Centriole-independent centrosome assembly in interphase mammalian cells

Fangrui Chen[1], Jingchao Wu[1], Malina K. Iwanski[1], Daphne Jurriens[1], Arianna Sandron[1], Milena Pasolli[1], Gianmarco Puma[1], Jannes Z. Kromhout[1], Chao Yang[1], Wilco Nijenhuis[1,2], Lukas C. Kapitein[1,2] and Anna Akhmanova[1]

[1] Cell Biology, Neurobiology and Biophysics, Department of Biology, Faculty of Science, Utrecht University, Utrecht, Netherlands

[2] Center for Living Technologies, Eindhoven-Wageningen-Utrecht Alliance, the Netherlands

Correspondence: a.akhmanova@uu.nl

Abstract

The major microtubule-organizing center (MTOC) in animal cells, the centrosome, comprises a pair of centrioles surrounded by pericentriolar material (PCM), which nucleates and anchors microtubules. Centrosome assembly depends on the interactions of PCM with centrioles, PCM self-association and dynein-mediated transport. Here, we show that if centrioles are lost due to PLK4 depletion or inhibition, PCM still forms a single centrally located MTOC when non-centrosomal microtubule minus-end organization pathways are disabled. Acentriolar MTOC assembly depends on dynein-driven coalescence of PCM clusters with attached microtubule minus ends and requires γ-tubulin, pericentrin, CDK5RAP2 and ninein, but not NEDD1, CEP152 or CEP192. PCM self-assembly is inhibited by AKAP450-dependent PCM recruitment to the Golgi and by CAMSAP2-mediated microtubule minus-end stabilization. However, if CAMSAP2 is linked to a minus-end-directed motor, a single MTOC containing PCM components can still form, and its organization depends on the presence of pericentrin. Our results reveal that the formation of a single central MTOC in interphase mammalian cells is not strictly centriole dependent but can be driven by self-organization of PCM and microtubule minus ends.

Introduction

The centrosome is the major microtubule organizing center (MTOC) in animal cells. It consists of two centrioles surrounded by pericentriolar material (PCM) (reviewed in (Conduit et al., 2015; Paz and Luders, 2017)). Major PCM components are microtubule-nucleating and anchoring proteins, which can associate with centrioles and with each other. While for a long time PCM was thought to be amorphous, super-resolution microscopy studies have shown that it has a distinct organization, with some proteins likely attached to the centriole wall and others organized around them (Fu and Glover, 2012; Lawo et al., 2012; Mennella et al., 2014; Mennella et al., 2012). This distinct organization is more obvious in interphase than in mitosis, when the microtubule-organizing capacity of the centrosome increases due to enhanced PCM recruitment. Many PCM components are known to oligomerize and interact with each other, and recent work suggested that phase separation of interacting PCM components can contribute to centrosome assembly (Raff, 2019; Woodruff et al., 2017). This idea is underscored by data showing that various cell-type specific assemblies of PCM components can form clusters which can nucleate and organize microtubules and serve as MTOCs in the absence of centrioles, particularly during the formation of mitotic spindle poles (Balestra et al., 2021; Chinen et al., 2021; Gartenmann et al., 2020; Meitinger et al., 2020; Watanabe et al., 2020; Yeow et al., 2020). Furthermore, an important centrosome component, cytoplasmic dynein, is a motor that can bind to different PCM proteins and transport them to the centrosome-anchored microtubule ends, where these PCM proteins can nucleate and anchor more microtubules, thus generating a positive feedback loop in centrosome assembly (Balczon et al., 1999; Burakov et al., 2008; Purohit et al., 1999; Redwine et al., 2017). Dynein and its mitotic binding partner NuMA also strongly participate in the formation of mitotic and meiotic spindle poles (Chinen et al., 2020; Khodjakov et al., 2000; Kolano et al., 2012). The relative importance of different molecular pathways of MTOC assembly varies between cell systems and phases of the cell cycle.

Many interphase mammalian cell types have a radial microtubule array. In immune cells, which have a sparse microtubule network, the majority of microtubule minus ends are attached to the centrosome (reviewed in (Meiring et al., 2020)). However, in most commonly studied cultured cell lines, such as fibroblasts, epithelial, endothelial or cancer cells, microtubule networks are denser and not all minus ends can be directly attached to the centrosome. In such cells, non-centrosomal microtubule minus ends are often stabilized by the members of CAMSAP family (Jiang et al., 2014; Meng et al., 2008; Tanaka et al., 2012), and the Golgi apparatus serves as a secondary MTOC (Efimov et al., 2007; Rios, 2014; Wu et al., 2016; Zhu and Kaverina, 2013). If centrosomes are lost because centriole duplication is blocked by inhibiting the kinase PLK4 or depleting another essential centriole component, Golgi-dependent microtubule organization becomes predominant (Gavilan et al., 2018;

Martin et al., 2018; Wu et al., 2016). The ability of the Golgi complex to serve as an MTOC critically depends on the Golgi adaptor AKAP450, which recruits several PCM components that nucleate microtubules, including the γ-tubulin ring complex (γ-TuRC), CDK5RAP2 and pericentrin. Moreover, AKAP450 also tethers microtubule minus ends stabilized by CAMSAP2 to the Golgi membranes (Gavilan et al., 2018; Rivero et al., 2009; Wu et al., 2016). In the absence of AKAP450, the Golgi ribbon is maintained, but neither PCM components nor CAMSAP-stabilized microtubule minus ends can be attached to the Golgi membranes (Gavilan et al., 2018; Rivero et al., 2009; Wu et al., 2016). These data seem to suggest that centrioles and/or Golgi membranes are essential for assembling a single MTOC in interphase. However, this notion appears to be inaccurate: in our previous study in RPE1 cells, we observed that a single compact acentriolar MTOC (aMTOC) can still form after centriole loss in AKAP450 knockout cells, which lack the ability to organize microtubules at the Golgi, if the stabilization of free minus ends in these cells is disabled by knocking out CAMSAP2 (Wu et al., 2016).

Here, we used this observation as a starting point to explore the centriole-independent pathway of centrosome assembly in interphase mammalian cells. We found that AKAP450/CAMSAP2 knockout cells formed compact aMTOCs when PLK4 was either inhibited or depleted. aMTOC formation in these cells required microtubules and depended on dynein, which brought together small PCM clusters with attached minus ends. The resulting aMTOCs were often cylindrical rather than spherical in shape and contained a subset of the major centrosome components. γ-tubulin, pericentrin, CDK5RAP2 and ninein were necessary for the formation of compact aMTOCs, whereas some other major PCM proteins, namely CEP192, CEP152 and NEDD1, were neither enriched in these structures nor required for their formation. A single aMTOC could also form in the presence of CAMSAP2, if this protein was directly linked to a microtubule minus-end-directed motor. The formation of a compact MTOC in such cells still required pericentrin. Assembly of a single MTOC in interphase mammalian cells can thus be achieved without centrioles through the concerted action of scaffolds for microtubule nucleation and stabilization, provided that they are linked to a minus-end-directed motor.

Results

Assembly of microtubule-dependent aMTOCs in AKAP450/CAMSAP2 KO cells lacking PLK4 activity

To induce centrosome loss in RPE1 cells, we treated these cells for 11 days with the PLK4 inhibitor centrinone B (Wong et al., 2015) (Figure 1A,B). In wild type (WT) cells, PCM (detected with antibodies against pericentrin) relocalized to the Golgi apparatus, and the microtubule array reorganized around the Golgi membranes, as described previously (Gavilan et al., 2018; Wu et al., 2016) (Figure 1C,D). In

AKAP450 knockout cells, centriole loss led to the appearance of strongly dispersed PCM clusters, which could no longer bind to the Golgi, and a highly disorganized microtubule system, consistent with published work (Gavilan et al., 2018; Wu et al., 2016) (Figure 1D,E). In contrast, in AKAP450/CAMSAP2 double knockout cells, a single compact MTOC with microtubules focused around it was observed (Figure 1D-F). Formation of a single compact aMTOC was also observed in AKAP450 knockout cells transiently depleted of CAMSAP2 by siRNA transfection (Figure 1 – figure supplement 1A,B).

Unlike the centrosomes, which always have a spherical shape, compact aMTOCs in AKAP450/CAMSAP2 knockout cells were cylindrical in ~35% of the cells, whereas in the remaining cells that lacked centrioles based on staining for centrin, MTOCs had a round shape (~38% of the cells); the rest of the centrin-negative cells either had dispersed PCM clusters (~7%) or no detectable PCM clusters (~11%) (Figure 1 – figure supplement 1C,D). In contrast, ~72% of acentriolar AKAP450 knockout cells had dispersed PCM, while compact aMTOCs were very rare (Figure 1E, Figure 1 – figure supplement 1C,D). Analysis by Stimulated Emission Depletion (STED) microscopy revealed that cylindrical aMTOCs in AKAP450/CAMSAP2 knockout cells consisted of small clusters of PCM components, including pericentrin, CDK5RAP2, γ-tubulin, ninein and dynein heavy chain (Figure 1F). aMTOCs with a clearly elongated shape had an average length of ~11 µm and an average width of ~1.5 µm (Figure 1G).

To study PCM dynamics in aMTOCs, we generated cell lines stably expressing the PCM component CDK5RAP2 tagged with GFP. In WT cells, GFP-CDK5RAP2 was localized to the centrosome and the Golgi apparatus as expected (Figure 1 – figure supplement 2A). In centrinone-treated AKAP450/CAMSAP2 knockout cells, it was strongly enriched within aMTOCs and sometimes also present in small motile clusters around an aMTOC (Figure 1H, Figure 1 – figure supplement 2B). Fluorescence recovery after photobleaching (FRAP) assays showed that when the whole aMTOC was bleached, the recovery was very slow and incomplete (Figure 1H, I). If an aMTOC was photobleached partially, the dynamics of recovery showed cell-to-cell variability. Highly compacted aMTOCs did not undergo rearrangement and displayed slow redistribution of GFP-CDK5RAP2. In more loosely organized aMTOCs, some rearrangement of small PCM clusters was observed (Figure 1H,I); however, the recovery was still far from complete. These data indicate that aMTOCs display variable degrees of compaction and are composed of PCM clusters that display limited exchange of GFP-CDK5RAP2 with the cytoplasmic pool, possibly because most of the GFP-CDK5RAP2 is accumulated within the aMTOC.

Next, we investigated whether centriole loss induced by means other than pharmacological PLK4 inhibition could also cause the formation of a single aMTOC in AKAP450/CAMSAP2 knockout cells. To achieve efficient protein depletion in RPE1 cells, they were transfected with siRNAs twice (on day 0

and day 2), treated with thymidine starting from day 4 to block cell cycle progression and fixed and stained on day 5 or day 7 (Figure 1 – figure supplement 1E). Depletion of PLK4 using siRNAs caused the appearance of compact round or cylindrical aMTOCs, similar to those observed after PLK4 inhibition with centrinone, indicating that catalytically inactive PLK4 had no scaffolding role within these structures (Figure 1 – figure supplement 1E-H). The percentage of cells with compact aMTOCs increased over time (Figure 1 – figure supplement 1E-H), possibly due to the gradual depletion of PLK4. In contrast, depletion of an essential centriole biogenesis factor CPAP (Kohlmaier et al., 2009; Schmidt et al., 2009; Tang et al., 2009), which also led to centriole loss, was much less efficient in inducing compact aMTOCs, and cylindrical a MTOCs were not observed (Figure 1 – figure supplement 1E-G). After CPAP depletion, cells in which pericentrin formed dispersed clusters or no visible clusters predominated (~67%, Figure 1 – figure supplement E-G). Treatment of CPAP-depleted AKAP450/CAMSAP2 knockout cells with centrinone for 1 day promoted the assembly of compact round or cylindrical aMTOCs, and the proportion of such cells increased to ~55% after 3 days of centrinone treatment (Figure 1 – figure supplement 1E-I). We also tested whether the inhibition of PLK1, a kinase that is known to be a major regulator of PCM self-assembly in mitosis (Haren et al., 2009; Joukov et al., 2014; Lee and Rhee, 2011), has an effect on the formation of aMTOCs, but found this not to be the case (Figure 1 – figure supplement 1F). We conclude that PCM can assemble into a single stable MTOC in the absence of centrioles if PLK4 is either inactivated or depleted and the two major pathways of microtubule nucleation and minus-end stabilization dependent on AKAP450 at the Golgi membranes and CAMSAP2 are disabled.

Composition of aMTOCs and their effect on microtubule organization

To investigate the composition of aMTOCs, we stained centrinone-treated AKAP450/CAMSAP2 knockout cells with antibodies against different centrosome and centriole markers and microtubule-associated proteins (MAPs). As indicated above, abundant PCM components pericentrin, CDK5RAP2, ninein and γ-tubulin colocalized within aMTOCs (Figure 1F). In contrast, three other major PCM proteins, CEP152, CEP192 and NEDD1, could not be detected in these structures although they were present in centrosomes of AKAP450/CAMSAP2 knockout RPE1 cells that were not treated with centrinone (Figure 2A-C) and were also expressed in centrinone-treated cells (Figure 2 – figure supplement 1A). We then individually depleted all these proteins in centrinone-treated AKAP450/CAMSAP2 knockout cells using siRNAs. After the depletion of pericentrin, no clusters of other PCM components could be detected (Figure 2D, Figure 2 – figure supplement 1B). To confirm this result, we also attempted to knock out pericentrin in AKAP450/CAMSAP2 knockout cells, but such

cells were not viable, likely because centrosome defects in these cells caused prolonged mitosis and p53-dependent G1 arrest (Fong et al., 2016; Lambrus et al., 2016; Meitinger et al., 2016). However, we were able to knock out pericentrin in cells lacking AKAP450, CAMSAP2 and p53 (Figure 2 – figure supplement 2), confirming that the loss of p53 makes the cells more tolerant to centrosome defects. Similar to pericentrin-depleted cells, these quadruple knockout cells were unable to form a single aMTOC when treated with centrinone (Figure 2E). In these acentriolar quadruple knockout cells, CDK5RAP2, γ-tubulin and cytoplasmic dynein displayed no clustering, while ninein and PCM1, a centriolar satellite protein that localizes closely around the centrosome in normal cells (Prosser and Pelletier, 2020), formed small clusters distributed throughout the cytoplasm (Figure 2 – figure supplement 3).

Depletion of CDK5RAP2, γ-tubulin or ninein in centrinone-treated AKAP450/CAMSAP2 knockout cells did not prevent the formation of small pericentrin clusters, but these failed to coalesce into a single aMTOC (Figure 2F-H, J, Figure 2 – figure supplement 1B). In contrast, depletion of CEP152, CEP192 or NEDD1 had no effect on the formation of aMTOCs (Figure 2A-C, J, Figure 2 – figure supplement 1B), in agreement with the fact these proteins could not be detected within these structures. aMTOCs contained several centriole biogenesis factors, including CPAP, CP110 and CEP120, but lacked centrin and CEP135; however, the depletion of several centriolar proteins did not affect aMTOC formation (Figure 2J, Figure 2 – figure supplement 1C). We also detected within aMTOCs the component of the HAUS complex HAUS2, the centrosomal protein CEP170, dynein, dynactin, CLASP1/2, CLIP-115, CLIP-170, chTOG, KIF2A and KIF1C (Figure 2J, Figure 2 – figure supplement 1C). We tested the importance of some of these proteins for aMTOC formation by siRNA-mediated depletion (see Figure 2J for an overview), but among the tested proteins, only cytoplasmic dynein appeared essential for this process. In dynein-depleted cells, no clusters of pericentrin or other PCM components could be detected after centrinone treatment (Figure 2I,J). It is important to note, however, that because we used siRNAs to reduce protein expression, we cannot exclude that the residual levels of some of the investigated proteins were sufficient to support aMTOC formation. Since we have detected in the aMTOCs several microtubule plus-end tracking proteins (+TIPs), such as CLIP-170, CLASP1/2 and the large subunit of dynactin p150Glued, we also tested for the presence of the core components of the +TIP machinery, EB1 and EB3, but found that they were not enriched within the aMTOCs (Figure 2J, Figure 2 – supplement 4A). Using the previously described EB1/EB3/CAMSAP2mut cells, which lack EB3, CAMSAP2 and C-terminal partner-binding half of EB1 (Yang et al., 2017), we generated a knockout cell line that also lacks AKAP450 and found that aMTOCs could still form in these cells (Figure 2J, Figure 2 – figure supplement 4B,C). We conclude that compact aMTOCs formed in AKAP450/CAMSAP2

knockout cells concentrate many but not all components of conventional centrosomes and require some of them for their formation.

As could be expected, the presence of an aMTOC was a critical determinant of microtubule organization and density in acentriolar cells: microtubules were focused around aMTOCs if present and disorganized in cells lacking aMTOCs. The strongest loss of microtubule density was observed in cells lacking pericentrin, dynein or γ-tubulin, while milder phenotypes were observed in cells lacking CDK5RAP2 or ninein (Figure 3A,B). To further characterize microtubule organization after the loss of these proteins, we analyzed the proportion of the radial and non-radial microtubules. Whereas control cells (AKAP450/CAMSAP2 knockout cells treated with centrinone and control siRNA) formed radial microtubule networks with ~12% non-radial microtubules, acentriolar cells lacking pericentrin or cytoplasmic dynein had ~46% non-radial microtubules, and the depletion of CDK5RAP2, ninein and γ-tubulin led to an intermediate phenotype with 25-30% non-radial microtubules (Figure 3C,D). aMTOC formed in AKAP450/CAMSAP2 knockout cells upon centrinone treatment can thus organize microtubules and increase microtubule density (Figure 3E), and the formation and function of such an aMTOC depend on pericentrin, CDK5RAP2, ninein, γ-tubulin and dynein.

Dynamics of aMTOC assembly and disassembly

To test whether the formation and maintenance of aMTOCs in AKAP450/CAMSAP2 knockout cells depends on microtubules, we depolymerized them by treating cells with nocodazole at 37°C and found that aMTOCs fragmented into small clusters during nocodazole treatment and reassembled into a single structure after nocodazole washout (Figure 4A-C). Because we found that aMTOC formation is dynein-dependent, we also included in these experiments the dynein inhibitor dynapyrazole A (Steinman et al., 2017). We confirmed that treatment with dynapyrazole A for 3 hrs had no effect on dynein expression (Figure 4D) and found that the addition of this drug before nocodazole treatment prevented the disassembly of aMTOCs, whereas treatment of cells with dynapyrazole A during nocodazole washout strongly inhibited aMTOC re-assembly (Figure 4A-C). These data indicate that microtubule-dependent dispersal and coalescence of PCM clusters into aMTOCs are driven by dynein activity.

We next studied PCM dynamics using stably expressed GFP-CDK5RAP2 as a marker in live cells where microtubules were labeled SiR-tubulin. GFP-CDK5RAP2 was mostly immobile within aMTOCs before nocodazole treatment (Figure 1 – figure supplement 2B, Video 1). After a few minutes of nocodazole treatment, when the microtubule density was significantly reduced, small PCM clusters started to

move out of the aMTOC and undergo rapid directional motility with speeds of up to 2 µm/sec, which is within the range characteristic for cytoplasmic dynein (Schlager et al., 2014) (Figure 4E,F, Figure 4 – figure supplement 1A, Video 1). Once microtubules were completely disassembled, the movement of GFP-CDK5RAP2-positive clusters stopped, indicating that it is microtubule-dependent but occurs only when the microtubule network is partly depolymerized. Since cluster dispersal towards the cell periphery could be blocked by a dynein inhibitor, and since cytoplasmic dynein is a minus-end-directed motor, these data indicate that during microtubule disassembly by nocodazole at 37°C, there is a transient stage when PCM clusters interact with only a few microtubules, some of which have their minus-ends facing outwards, and these microtubules serve as tracks for PCM transport. To support this idea, we used motor-PAINT, a technique that employs nanometric tracking of purified kinesin motors on the extracted cytoskeleton of fixed cells to super-resolve microtubules and determine their orientation (Tas et al., 2017). Using this approach, we determined microtubule orientations in centrinone-treated AKAP450/CAMSAP2 knockout cells and in cells that were also treated with nocodazole for 15 min to induce partial microtubule disassembly (Figure 4G, Figure 4 – figure supplement 1B). We found that the cells contained a significant number of minus-end-out microtubules, and their proportion increased during early stages of nocodazole treatment, possibly because minus-end-out microtubules are more stable (Figure 4G, e.g., minus-end-out microtubules constituted ~23% of the total microtubule length determined from kinesin-1 trajectories in the untreated cell and ~46% in the nocodazole-treated cell). These microtubules could serve as tracks for outward movement of PCM, causing the disassembly of aMTOC when the overall microtubule density around the aMTOC was strongly reduced (Figure 4H). These data suggest that the dense network of PCM-anchored microtubule minus-ends keeps aMTOC compacted by dynein-mediated forces, which can, however, pull it apart when the microtubules are disorganized.

Next, we investigated in more detail aMTOC reassembly during nocodazole washout. Small PCM clusters positive for pericentrin, CDK5RAP2, γ-tubulin and the centriolar satellite protein PCM1 that co-localized with the ends of microtubules labeled with EB1 could be detected 30 s after nocodazole washout; these nascent microtubules did not colocalize with the Golgi membranes (Figure 5A, Figure 5 – figure supplement 1A). Ninein was not detected within the clusters at this early stage of microtubule regrowth but could be found 2 min after nocodazole washout. In contrast, no clusters of CEP192 or NEDD1 were observed even 10 min after nocodazole washout (Figure 5A, Figure 5 – supplement 1A, B). Depletion of pericentrin, CDK5RAP2 and γ-tubulin strongly inhibited microtubule nucleation in these conditions, whereas the depletion of dynein heavy chain or ninein had a milder effect (Figure 5B,C). Live cell imaging with GFP-CDK5RAP2 and SiR-tubulin showed that CDK5RAP2 clusters with attached microtubules coalesced by undergoing microtubule-based movements (Figure

5D), and measurements in cells fixed at different time points after nocodazole washout showed that a partly radial microtubule system emerged already 2 min after nocodazole washout (Figure 5 – figure supplement 1C). Reassembly of a single aMTOC in the central part of the cell happened within ~15 min after nocodazole washout, though typically it was less compact than in cells that were not treated with nocodazole (Figure 5D-G). Depletion of pericentrin, γ-tubulin and dynein heavy chain strongly inhibited the reformation of a radial microtubule network during nocodazole washout, whereas the effect of depleting CDK5RAP2 and ninein was less strong (Figure 5 – figure supplement 1C-E). Live cell imaging of acentriolar AKAP450/CAMSAP2 knockout RPE1 cells stably expressing GFP-CDK5RAP2 showed that when pericentrin was depleted, CDK5RAP2 clusters were not detectable and the microtubule network, both before nocodazole treatment and after nocodazole washout, was disorganized (Figure 5 – figure supplement 2, Video 2). Taken together, our data show that pericentrin and γ-tubulin form microtubule-nucleating and anchoring units that can be assembled into larger structures by dynein-based transport. CDK5RAP2 contributes to microtubule nucleation activity, whereas ninein appears to act somewhat later and contributes to the formation of a single compact aMTOC.

The role of CAMSAP2-stabilized minus ends in defining microtubule network geometry

All the components of aMTOCs observed in AKAP450/CAMSAP2 knockout cells were also present in AKAP450 knockout cells, yet these cells did not form a single aMTOC upon centrinone treatment because they expressed CAMSAP2. In these cells, CAMSAP2-stabilized microtubule minus ends were randomly distributed throughout the lamella, and microtubules were largely disorganized, although many microtubules tended to co-align with the long axis of the lamella or of the whole cell (Figure 6A). Live imaging of GFP-CDK5RAP2 together with SiR-tubulin in these cells showed that PCM clusters moved along microtubules and occasionally encountered each other, but the movement directions were random and PCM clusters did not coalesce into a single structure (Figure 6B, Figure 6 – figure supplement 1A, Video 3). Treatment with nocodazole and subsequent nocodazole washout confirmed that the motility of GFP-CDK5RAP2 clusters in centrinone-treated AKAP450 knockout cells is microtubule-dependent and that these clusters can nucleate microtubules and move together with their ends, but do not converge into a single compact aMTOC (Figure 6 – figure supplement 1A-C, Video 3). Treatment with dynapyrazole A strongly inhibited the movements of small PCM clusters (Figure 6 – figure supplement 1D,E, Video 4), indicating that they are dynein-driven. After the depletion of pericentrin, GFP-CDK5RAP2 became completely diffuse, and it also did not form any clusters during nocodazole treatment or washout (Figure 6 – figure supplement 2, Video 5), indicating

that clustering of GFP-CDK5RAP2 in AKAP450 knockout cells is pericentrin-dependent. Based on these data, we conclude that in AKAP450 knockout cells, pericentrin still forms PCM clusters that can nucleate microtubules and can be moved by dynein along other microtubules. However, since CAMSAP2-stabilized microtubule minus-ends in these cells are not attached to the Golgi membranes and do not interact with dynein, they are distributed randomly. This results in a disorganized microtubule network, with the minus ends pointing both in- and outwards, and leads to random motility of PCM clusters that prevents assembly of a single compact aMTOC (Figure 6C).

We next wondered whether we could force aMTOC formation in AKAP450 knockout cells by linking CAMSAP2-stabilized minus ends to a minus-end-directed motor. To avoid potential cell toxicity associated with manipulating cytoplasmic dynein, we used the motor-containing part of a moss kinesin-14, type VI kinesin-14b from the spreading earthmoss *Physcomitrella patens* (termed here ppKin14). The C-terminal motor-containing part of this protein can efficiently induce minus-end-directed motility of different cargoes in mammalian cells when it is tetramerized through a fusion with the leucine zipper domain of GCN4 (GCN4-ppKin14-VIb (861–1321)) and recruited to cargoes using inducible protein heterodimerization (Jonsson et al., 2015; Nijenhuis et al., 2020). Here, we employed a chemical heterodimerization system that is based on inducible binding of two protein domains, FRB and FKBP, upon the addition of a rapamycin analog (rapalog) (Pollock et al., 2000). To ensure that all CAMSAP2-decorated microtubule minus ends are linked to kinesin-14, we rescued centrinone-treated AKAP450/CAMSAP2 knockout cells by expressing CAMSAP2 fused to a tandemly repeated FKBP domain (2FKBP-mCherry-CAMSAP2) (Figure 6D-F). This construct was co-expressed with the FRB-GCN4-tagBFP-ppKin14 fusion, which by itself localized quite diffusely, with only a weak enrichment along microtubules, as described previously (Nijenhuis et al., 2020) (Figure 6D,F). In the absence of rapalog, CAMSAP2-decorated microtubule minus ends were distributed randomly, similar to endogenous CAMSAP2 in AKAP450 knockout cells (Figure 6F). However, upon rapalog addition, ppKin14 was rapidly recruited to CAMSAP2-decorated microtubule ends, and after 2 hrs, more than 90% of cells acquired a radial microtubule organization (Figure 6E-G). In rapalog-treated cells, CAMSAP2-bound microtubule minus ends formed either a tight cluster or a “whirlpool-like” ring in the cell center (Figure 6D-G, Figure 6 – figure supplement 1F). The whirlpool-like arrangement likely comes about when CAMSAP2-stretches are a bit longer and keep sliding against each other, forming a nematic circular bundle. The major aMTOC components, pericentrin, CDK5RAP2, γ-tubulin and ninein were also concentrated within the CAMSAP2 cluster, although they did not form a strongly compacted assembly (Figure 6G, Figure 6 – figure supplement 1F). These data indicate that the positioning of stabilized minus-ends is a very important determinant of the overall microtubule organization in

interphase cells, and that linking a minus-end-directed motor, even a heterologous one, to stable minus ends can induce self-assembly of a radial microtubule array.

The role of PCM in CAMSAP2-driven microtubule organization

Next, we tested whether PCM plays a role in CAMSAP-driven aMTOC formation by inducibly attaching CAMSAP2 to ppKin14 in centrinone-treated cells with both AKAP450 and pericentrin knocked out (AKAP450/CAMSAP2/p53/pericentrin knockout). In the absence of rapalog, CAMSAP2-stabilized minus ends and the whole microtubule network were disorganized, as expected (Figure 7A,D). After rapalog addition, microtubules acquired a radial organization, but their minus ends usually did not converge in a single spot but rather accumulated in a ~30-70 µm-large ring-like structure (Figure 7A,D, Figure 7- figure supplement 1, Video 6). Staining for PCM markers showed that CDK5RAP2 and γ-tubulin were enriched in the vicinity of CAMSAP2-positive microtubule minus ends, whereas ninein appeared rather diffuse (Figure 7A). To determine the nature of the structure "corralled" by the ring of CAMSAP2-decorated minus ends in rapalog-treated cells, we stained for different membrane organelles and found that whereas there was no strong correlation with the nucleus, Golgi membranes or lysosomes, the majority of mitochondria were found within the CAMSAP2 ring, and the endoplasmic reticulum (ER) displayed increased density overlapping with the CAMSAP2 ring (Figure 7B, Figure 7 - figure supplement 1B). It therefore appeared that in the absence of pericentrin, CAMSAP2-decorated minus ends were brought together by ppKin14, but their convergence was impeded by the ER and possibly mitochondria, which were enriched in the central, thicker part of the cell before rapalog addition (see the upper panel of Figure 7 - figure supplement 1B). Transient transfection of centrinone-treated AKAP450/CAMSAP2/p53/pericentrin knockout cells with GFP-pericentrin rescued the formation of a tight CAMSAP2 cluster upon rapalog treatment (Figure 7C). Our data show that pericentrin-containing PCM contributes to the formation of an aMTOC driven by minus-end-directed transport of CAMSAP2-stabilized minus-ends.

To support this notion further, we also generated cells that were knockout for AKAP450, CAMSAP2, CDK5RAP2, myomegalin (MMG, homologue of CDK5RAP2), p53 and pericentrin. To achieve this, we used the previously described RPE1 cell line knockout for AKAP450, CAMSAP2, CDK5RAP2 and MMG (Wu et al., 2016), in which we sequentially knocked out p53 and pericentrin (Figure 7 – figure supplement 2A-G). While it was not possible to induce centriole loss by centrinone treatment in AKAP450/CAMSAP2/CDK5RAP2/MMG knockout cells because the proliferation of these cells was arrested in the absence of centrioles (Wu et al., 2016), centriole removal was successful in AKAP450/CAMSAP2/CDK5RAP2/MMG/p53/pericentrin knockout cells due to the absence of p53 and

led to microtubule disorganization (Figure 7 – figure supplement 2H). Interestingly, when these cells were co-transfected with FKBP-linked CAMSAP2 and FRB-linked ppKin14 and treated with rapalog (Figure 6D), we observed that CAMSAP2 clustering was even less efficient than in AKAP450/CAMSAP2/p53/pericentrin knockout cells (Figure 7D,E). 49% of AKAP450/CAMSAP2/CDK5RAP2/MMG/p53/pericentrin knockout cells had small bundles of CAMSAP2 stretches dispersed throughout the cytoplasm, and only 37% of these cells formed a ring of CAMSAP2-decorated minus ends, whereas 80% of AKAP450/CAMSAP2/p53/pericentrin knockout cells did form such a ring. We examined the ER and mitochondria in these cells and found that in cells that did form a CAMSAP2 ring, the ER displayed an overlapping ring-like density, although the mitochondria inside the CAMSAP2 ring were more scattered compared to those of AKAP450/CAMSAP2/p53/pericentrin knockout cells (Figure 7 – figure supplement 1B). In cells with dispersed CAMSAP2-positive bundles, no increased ER density or central accumulation of mitochondria were observed (Figure 7 – figure supplement 1B). These data further support the notion that during the formation an aMTOC, minus-end-directed transport of CAMSAP2-stabilized minus ends needs to be augmented by PCM function dependent on pericentrin, CDK5RAP2 and possibly also MMG.

Discussion

In this study, we explored the mechanisms driving MTOC assembly in acentriolar cells and showed that centrioles are not strictly needed to form a central compact MTOC and a radial microtubule array in interphase mammalian cells. Our data indicate that in the absence of the pathways that promote formation of non-centrosomal microtubules, cytoplasmic dynein can assemble a single aMTOC by bringing together microtubule minus ends that are nucleated and stabilized by PCM. However, the formation of MTOC in acentriolar cells is slow and less robust than in centriole-containing cells. Similar to the formation of spindle poles in mitosis (Meraldi, 2016), centrioles can thus be regarded as catalysts of interphase centrosome assembly.

We found that self-assembly of aMTOCs is driven by dynein-dependent transport of PCM components that include pericentrin, CDK5RAP2, γ-TuRC and ninein. In acentriolar cells that we studied, the major scaffold for interphase PCM assembly is pericentrin, which recruits CDK5RAP2 and ninein, in agreement with previous work (Chen et al., 2014; Delaval and Doxsey, 2010; Kim and Rhee, 2014; Lawo et al., 2012). Moreover, it has been established previously that CDK5RAP2 binds and activates γ-TuRC (Choi et al., 2010; Fong et al., 2008), and the same may be true for pericentrin (Takahashi et al., 2002) and possibly also for ninein (Delgehyr et al., 2005; Mogensen et al., 2000). Pericentrin and ninein can both directly interact with dynein (Purohit et al., 1999; Redwine et al., 2017), and an interaction between CDK5RAP2 and dynein has also been reported (Jia et al., 2013; Lee and Rhee, 2010). All these interactions likely contribute to the formation of aMTOCs.

Pericentrin-dependent MTOC assembly has also been observed in acentriolar mitotic cells (Chinen et al., 2021; Watanabe et al., 2020), but the interphase pathway displays some interesting differences. It seems that while oligomerization and clustering of pericentrin molecules is important for MTOC formation both in interphase and in mitosis, during mitotic entry, pericentrin may form condensates (Jiang et al., 2020), while in interphase, dynein-mediated motility dominates the behavior of pericentrin clusters. The compact aMTOC structure we observed in interphase was not simply a result of small pericentrin- and CDK5RAP2-positive PCM clusters coming into proximity of each other and sticking together, but also depended on active transport. In AKAP450 knockout cells, we also frequently observed CDK5RAP2-containing PCM clusters encountering each other, yet they did not coalesce into a single MTOC because they kept moving in random directions on CAMSAP2-stabilized microtubules. When most CAMSAP2-decorated minus ends were brought together by a minus-end-directed motor, pericentrin accumulated in the vicinity of such an artificially formed MTOC and contributed to its formation, but did not form a single solid body, likely because it kept moving along the sides of CAMSAP2-decorated microtubules but was not attached to their outermost minus ends.

A strongly compacted aMTOC only formed when most microtubule minus ends were anchored by PCM clusters. The shape of the MTOC was cylindrical rather than spherical in a significant proportion of such cells, suggesting that it was optimized for increasing the surface area. A larger surface area allows for the attachment of more microtubules and fits with the idea that aMTOC formation is primarily driven by the coalescence of minus-end-attached PCM clusters rather than free oligomers of PCM proteins. Altogether, it appears that active, dynein-mediated transport of pericentrin-based PCM clusters rather than spontaneous formation of PCM condensates is the major driver of interphase aMTOC assembly. This explains why aMTOCs are exquisitely sensitive to microtubule disassembly by nocodazole: during intermediate stages of microtubule loss, PCM complexes that are no longer attached to microtubule minus ends start to move on the remaining microtubules, and therefore, a few surviving minus-end-out microtubules can serve as rails to drive the dispersal of the aMTOC (Figure 4H). Furthermore, PCM dynamics within aMTOCs show no hallmarks of liquid droplet-like behavior: PCM components do not appear to be in equilibrium with the soluble cytoplasmic pool, and GFP-CDK5RAP2 displays very slow redistribution within the aMTOC. As CDK5RAP2 is recruited to the aMTOC by pericentrin, these data suggest that pericentrin is also quite immobile within aMTOCs.

Although pericentrin can directly bind to γ-TuRC, CDK5RAP2 and ninein are also needed for aMTOC formation. Analysis of different stages of microtubule recovery after nocodazole washout suggested that CDK5RAP2 is important for efficient microtubule nucleation, consistent with its role as an activator of γ-TuRC (Choi et al., 2010). Ninein can be detected within nascent aMTOC structures with some delay after their formation and might be important for stabilizing these structures or promoting minus-end anchoring, as proposed by many previous studies (Abal et al., 2002; Chong et al., 2020; Delgehyr et al., 2005; Goldspink et al., 2017; Lechler and Fuchs, 2007; Mogensen et al., 2000; Shinohara et al., 2013; Zheng et al., 2020). The importance of ninein for the formation of aMTOCs illustrates its function in minus-end organization within the PCM that is independent of centriolar appendages, one of the sites of ninein localization at the centrosome (Chong et al., 2020; Delgehyr et al., 2005; Sonnen et al., 2012).

A major difference between interphase and mitotic MTOC assembly is the role of other major PCM components, CEP192 and the γ-TURC-binding protein NEDD1. In our experiments, CEP192 and its binding partners CEP152 and NEDD1 (Gomez-Ferreria et al., 2012; Joukov et al., 2014; Kim et al., 2013; Sonnen et al., 2013) were not enriched at aMTOCs, and their depletion appeared to have no impact on aMTOC formation. This is surprising, because during mitosis, CEP192 is essential (Gomez-Ferreria et al., 2007; Joukov et al., 2014; Yang and Feldman, 2015; Zhu et al., 2008), and in acentriolar cells that rely on pericentrin and CDK5RAP2 for spindle pole formation, CEP192 is recruited to pericentrin clusters (Chinen et al., 2021; Watanabe et al., 2020). Moreover, although NEDD1 is

targeted to centrosomes by CEP192, pericentrin can also contribute to the centrosomal targeting of NEDD1 independently of CEP192 (Chi et al., 2021). Therefore, the lack of enrichment of CEP192, CEP152 and NEDD1 in interphase aMTOC is unexpected, particularly because these three proteins are present within interphase PCM at the centrosome, and multiple other centrosomal and centriolar proteins and MAPs are recruited to aMTOCs. Among the proteins enriched at aMTOCs, we did not identify any additional factors that would be crucial for aMTOC formation, but it is of course possible that this process requires some proteins that we have not tested. It is also important to note that because siRNA-mediated protein depletion may be incomplete, we cannot exclude that low amounts of some of the tested centrosome components or MAPs are sufficient to support aMTOC assembly.

An interesting question that remains unanswered by our work is the inhibitory role of PLK4 in interphase aMTOC formation. We did observe aMTOCs in cells depleted of PLK4, indicating that, unlike cells lacking TRIM37, which form PCM clusters containing catalytically inactive PLK4 (Meitinger et al., 2020; Yeow et al., 2020), interphase cells studied here do not rely on enzymatically inactive PLK4 for PCM assembly. PLK4 is known to phosphorylate NEDD1 (Chi et al., 2021), and it is possible that the lack of phosphorylation prevents this γ-TuRC activator and its partners, such as CEP192, from participating in interphase aMTOC assembly. It is of course also possible that PLK4 phosphorylation inhibits the interactions or activities of some of the players that are driving aMTOC formation.

An important conclusion of our study is the key role of CAMSAP2-stabilized minus ends in determining microtubule organization in the absence of the centrosome. Unlike the PCM components, CAMSAP2 does not interact with dynein, and if CAMSAP2-decorated minus ends are not attached to the Golgi membranes, which are themselves subject to dynein-based transport, the microtubule system becomes strongly disorganized. However, linking a minus-end-directed motor to CAMSAP2 can restore a radial microtubule array with a single MTOC, provided that the major active PCM components are also transported to microtubule minus ends due to the presence of pericentrin. Surprisingly, in the absence of pericentrin, minus-end-directed convergence of CAMSAP2-bound minus ends drives “corralling” of ER and mitochondria. Since there are currently no indications that CAMSAP2 specifically interacts with ER or mitochondria, we favor the idea that these organelles, which are normally enriched in the central, thicker part of the cell, form a physical obstacle for CAMSAP2-ppKin14-driven minus-end clustering, and that dynein-mediated transport of pericentrin-anchored minus ends helps to overcome this obstacle and form a compact aMTOC. Removal of CDK5RAP2 and its homologue MMG in these conditions further inhibits minus-end organization and aMTOC formation. This indicates that minus-end-directed transport of CAMSAP2-stabilized microtubule minus ends is by itself not sufficient to form a radial microtubule network but needs to synergize with PCM-dependent microtubule organization.

These data have implications for understanding how microtubules are reorganized in differentiated cells. During cell differentiation, the centrosome often loses its activity, and PCM is redeployed to other cellular locations (Martin and Akhmanova, 2018; Muroyama and Lechler, 2017; Sallee and Feldman, 2021). Our study shows that interphase PCM has the potential to self-assemble, but this ability is inhibited by PLK4, and the regulation of this kinase may thus influence PCM assembly and activity at different cellular locations. Further, we show that CAMSAP-dependent minus-end organization has a very dominant effect on the overall microtubule network geometry but can be affected by the presence of PCM components. This suggests that during microtubule reorganization in differentiated cells, PCM-dependent and CAMSAP-dependent pathways are likely to be co-regulated. This idea is strongly supported by studies of microtubule organization at the Golgi membranes (Gavilan et al., 2018; Wu et al., 2016) and the apical membranes of polarized epithelial cells, where components of both pathways colocalize and can display some redundancy (Goldspink et al., 2017; Khanal et al., 2016; Noordstra et al., 2016; Toya et al., 2016; Wang et al., 2015). In muscle cells, CAMSAPs are not expressed, and the organization of microtubule minus-ends is driven by the Golgi adaptor AKAP450 and some PCM proteins that are localized to the nuclear envelope and the Golgi (Gimpel et al., 2017; Oddoux et al., 2013; Vergarajauregui et al., 2020). In neurons, minus-ends can be organized by PCM, CAMSAPs, the Golgi membranes and endosomes (Fu et al., 2019; Garbrecht et al., 2021; Liang et al., 2020; Magescas et al., 2021; Pongrakhananon et al., 2018; Yau et al., 2014), though the cross-talk between different pathways is insufficiently understood. One common feature between these different systems and the data described here is that the function of PCM components, redeployed to different locations in differentiated cells, is dominated by two structurally related adaptors, AKAP450 and pericentrin, as well as CDK5RAP2 and ninein. In contrast, CEP192 seems to have a much more important role in mitotic rather than interphase cells. In line with this idea, recent work demonstrated that certain types of worm neurons contain an aMTOC that is formed by the functional counterparts of CDK5RAP2 (SPD-5), pericentrin (PCMD-1) and γ-tubulin, but lacks CEP192/SPD-2 (Garbrecht et al., 2021; Magescas et al., 2021). Future work will show whether this distinction is generally applicable. It would also be important to know to which extent PCM transport along microtubules contributes to microtubule organization in different cell types, and to determine how the biochemical and functional coupling between different pathways of microtubule nucleation and minus-end stabilization defines various geometries of microtubule networks.

Materials and Methods

DNA constructs and protein purification

To generate the lentiviral vector pLVX-GFP-CDK5RAP2-IRES-Puro, pLVX-IRES-Puro plasmid (Clontech) was digested with AgeI and NotI (FastDigest, Thermo Fisher), and then Gibson Assembly (NEB) was performed with gel-purified PCR product of GFP-CDK5RAP2 (Wu et al., 2016). To generate pB80-FRB-TagBFP-GCN4-ppKin14 and pB80-FRB-HA-GCN4-ppKin14, pB80-FRB-GFP-GCN4-ppKin14-VIb was digested with XbaI and BsrGI (FastDigest, Thermo Fisher), and then TagBFP and HA-tag encoding DNA fragments were subcloned into the linearized vector by Gibson Assembly.

To generate the PX459 with single guide RNA (sgRNA) sequences, pSpCas9(BB)-2A-Puro (PX459) V2.0 (Ran et al., 2013)(purchased from Addgene) was digested with FastDigest BbsI (Thermo Fisher), and the annealing product of single-strand sgRNA-encoding oligonucleotides was inserted into the linear PX459 linear vector by T4 ligation (Thermo Fisher). The sgRNA sequences that were used in this study are: sgRNA targeting AKAP450 5'- gAGGGTTACCTATGGGACTGA -3'; sgRNA targeting CAMSAP2 encoding gene 5'-gCATGATCGATACCCTCATGA-3'; sgRNA targeting p53-encoding gene exon 2 #1 5'-gCGTCGAGCCCCCTCTGAGTC-3'; sgRNA targeting p53 exon 4 #2 5'-gTCCATTGCTTGGGACGGCAA-3'; sgRNA targeting p53 exon 4 #3 5'-gCCATTGTTCAATATCGTCCG-3'; sgRNA targeting PCNT exon 5-1 #1 5'-gAGACGGCATTGACGGAGCTG-3'; sgRNA targeting pericentrin-encoding gene exon 5-2 #2 5'-GCTCAACAGCCGGCGTGCCC-3'.

To generate the GST-DmKHC(1-421)-mNeonGreen construct used for protein purification for motor-PAINT, the fragment containing amino acids 1 to 421 of the Drosophila melanogaster Kinesin Heavy Chain (DmKHC) was amplified from donor construct DmKHC(1-421)-GFP-6x-His with a C-terminal mNeonGreen tag by PCR and then cloned into a pGEX vector. The plasmid was transformed into *E. coli* BL21 cells for purification. Bacteria were cultured until OD600 $\approx$0.7 and cultures were cooled prior to inducing protein expression with 0.15 mM IPTG at 18°C overnight. Cells were then pelleted by centrifugation, snap frozen in liquid nitrogen, and stored at -80°C until use. Cells were rapidly thawed at 37°C before being resuspended in chilled lysis buffer (phosphate buffered saline (PBS) supplemented with 5 mM $MgCl_2$, 0.5 mM ATP, 0.1% Tween 20, 250 mM NaCl, and 1x complete protease inhibitor; pH 7.4). Bacteria were lysed by sonication (5 rounds of 30 s) and supplemented with 5 mM DTT and 2mg/mL lysozyme and then incubated on ice for 45 min. The lysate was clarified by centrifuging at 26000 xg for 30 minutes before being incubated with equilibrated Glutathione Sepharose 4B resin for 1.75 hrs. Beads were then pelleted, resuspended in wash buffer (PBS supplemented with 5 mM $MgCl_2$, 0.1% Tween 20, 250 mM NaCl, 1 mM DTT, and 0.5 mM ATP; pH 7.4), and transferred to a BioRad column. Once settled, the resin was washed with 2 x 10 column volumes

(CV) wash buffer, followed by 1 x 10CV PreScission buffer (50 mM Tris-HCl, 5 mM $MgCl_2$, 100mM NaCl, 1 mM DTT, 0.5 mM ATP; pH 8.0). The resin was then incubated overnight in 4CV PreScission buffer with 80U PreScission protease to cleave off the GST tag. The following morning, after allowing the resin to settle, the eluent was collected, concentrated by spinning through a 3000kDa MWCO filter, supplemented with an additional 0.1mM ATP, 1mM DTT, and 20% w/v sucrose before flash freezing in liquid nitrogen, and finally stored at -80°C. Concentration was determined using a Nanodrop. All steps from lysis onwards were performed at 4°C.

Cell culture and drug treatment

hTERT immortalized RPE-1 (RPE1) cell lines were grown in an 1:1 mix of DMEM and F-10 (Lonza) and Human Embryonic Kidney (HEK) 293T cells line were cultured in DMEM, both supplemented with 10% fetal bovine serum (FBS, GE Healthcare) and 1% penicillin and streptomycin (Sigma-Aldrich). All cells were grown in tissue culture polystyrene flasks (Corning) and were maintained in a humidified incubator at 37°C with 5% CO_2. Mycoplasma contamination was routinely checked with LT07-518 Mycoalert assay (Lonza).

FuGENE 6 (Promega) was used to transfect RPE1 cells with plasmids for generating CRISPR/Cas9 knockouts, immunofluorescence staining and live cell imaging; RNAiMAX (Thermo Fisher Scientific) was used to transfect RPE1 cells with siRNAs at 20 nM; MaxPEI was used to transfect HEK293T cells for lentivirus packaging. Transfections were performed according to the manufacturer's instructions within the recommended reagent/DNA or reagent/siRNA ratio range.

We used the following drugs: centrinone B (Tocris Bioscience), nocodazole (Sigma), rapalog (A/C Heterodimerizer, Takara), dynapyrazole A (Sigma-Aldrich) and BI2536 (Selleckchem).

To remove centrioles, RPE1 cells were treated with 125 nM centrinone B containing complete medium for ~10 days, and drug-containing medium was refreshed every 24 hrs; cell confluence was maintained around ~50-80% during the treatment.

For the microtubule disassembly and regrowth assay, the acentriolar RPE1 cells were seeded onto coverslips in 24-well plates and incubated for 24 hrs, then cells were treated with 10 µM nocodazole for 1 hr in an incubator (37°C, 5% CO_2) and followed by another 1 hr treatment at 4°C to achieve complete disassembly of stable microtubule fragments. Nocodazole washout was then carried out by at least six washes on ice with ice-cold complete medium; subsequently, plates were moved to a 37°C water bath and pre-warmed medium was added to each well to allow microtubule regrowth.

For the inducible ppKin14-CAMSAP2 heterodimerization experiment, acentriolar cells were seeded onto coverslips in 24-well plates, cultured with centrinone B containing medium and co-transfected with 2FKBP-mCherry-CAMSAP2 and FRB-TagBFP-GCN4-ppKin14 vectors. 24 hrs after transfection, rapalog was added into the medium at a final concentration of 50 nM and incubated overnight for preparation of fixed cells. For live imaging, rapalog was used at 100 nM.

Lentivirus packaging and generation of transgenic stable cell lines

Lentiviruses were produced by MaxPEI-based co-transfection of HEK293T cells with the transfer vectors together with the packaging vector psPAX2 and envelope vector pMD2.G (psPAX2 and pMD2.G were a gift from Didier Trono, Addgene plasmid #12259 and #12260; RRID:Addgene_12259 and RRID:Addgene_12260). Supernatant of packaging cells was harvested 48-72 hrs after transfection, filtered through a 0.45 µm filter, incubated with a polyethylene glycol (PEG)-6000-based precipitation solution overnight at 4°C and centrifuged for 30 minutes at 1500 rpm to concentrate the virus. Lentiviral pellet was resuspended in PBS.

Wild type, AKAP450 and AKAP450/CAMSAP2 knockout RPE1 cells were infected with lentivirus and incubated in complete medium supplemented with 8 µg/ml polybrene (Sigma-Aldrich). After 24 hrs, the cell medium was replaced with fresh medium. Starting 72 hrs after viral transduction, cells were subjected to selection with puromycin at a concentration of 25 µg/ml for wild-type, 20 µg/ml for AKAP450 knockout and 15 µg/ml for AKAP450/CASMAP2 knockout for up to 3 days (until most of the untransduced control cells, treated with the same concentration of antibiotic, were dead). After selection, cells were grown in normal medium for 3 days and individual colonies expressing GFP were isolated into 96-well plates by fluorescence-activated cell sorting (FACS). Sorted single transgenic stable cell lines were further confirmed by immunofluorescence staining to check the expression level of GFP-CDK5RAP2 and its colocalization with other centrosomal proteins.

Generation of CRIPSR/Cas9 knockout cell lines

The CRISPR/Cas9-mediated knockout of p53-, pericentrin-, AKAP450- and CAMSAP2-encoding genes was performed as described previously (Ran et al., 2013). In brief, AKAP450/CAMSAP2 knockout RPE1 cells (Wu et al., 2016) were transfected with the vectors bearing the appropriate targeting sequences using FuGENE 6. One day after transfection, the transfected AKAP450/CAMSAP2 knockout RPE1 cells were subjected to selection with 15 µg/ml puromycin for up to 3 days. After selection, cells were allowed to recover in normal medium for ~7 days, and knockout efficiency was checked by

immunofluorescence staining. Depending on the efficiency, 50–500 individual clones were isolated and confirmed by immunofluorescence staining, and the resulted single colonies were characterized by Western blotting, immunostaining and genome sequencing. AKAP450/CAMSAP2/p53 and AKAP450/CAMSAP2/MMG/CDK5RAP2/p53 knockout cell lines were generated first and subsequently, each of them was used to knock out the gene encoding pericentrin. The mutated portions of the p53- and pericentrin-encoding genes were sequenced using gel-purified PCR products obtained with primers located in the vicinity of the corresponding sgRNA targeting sites.

Antibodies, immunofluorescence staining and Western blotting

Antibodies used for immunostaining and Western blotting are listed in the Key Reagent or Resource table. For immunofluorescence cell staining, cultured cells were fixed with –20°C methanol for 5 min or with 4% paraformaldehyde (PFA) for 12 min at room temperature, rinsed in PBS for 5 min, permeabilized with 0.15% Triton X-100 in PBS for 2 min, washed 3 times for 5 min with 0.05% Tween-20 in PBS, sequentially incubated for 20 min in the blocking buffer (2% BSA and 0.05% Tween-20 in PBS), 1 hr with primary antibodies in the blocking buffer, washed 3 times for 5 min with 0.05% Tween-20 in PBS, then for 1 hr in secondary antibodies in the blocking buffer, washed 3 times for 5 min with 0.05% Tween-20 in PBS, and air-dried after a quick wash in 96% ethanol. Cells were mounted in Vectashield mounting medium with or without DAPI (Vector laboratories, Burlingame, CA). Alexa Fluor -405, -488, –594 and −647 conjugated goat antibodies against rabbit, rat and mouse IgG were used as secondary antibodies (Molecular Probes, Eugene, OR).

For Western blotting, cells were harvested from six-well plates or 10 cm dishes at 90% confluence and protein extracts were prepared using the lysis buffer containing 20 mM Tris-Cl, pH 7.5, 150 mM NaCl, 0.5 mM EDTA, 1 mM DTT, 1% Triton X-100 or RIPA buffer containing 50 mM Tris-HCl, pH 7.5, 150 mM NaCl, 1% Triton X-100, 0.5% Sodium Deoxycholate supplemented with protease inhibitor and phosphatase inhibitors (Roche). Samples were run on polyacrylamide gels, followed by transfer on 0.45 µm nitrocellulose membrane (Sigma-Aldrich). Blocking was performed in 2% BSA in PBS for 30 min at room temperature. The membrane was first incubated with the primary antibodies overnight at 4°C and washed with 0.05% Tween-20 in PBS 3 times and subsequently incubated with secondary antibodies for 1 hr at room temperature and washed 3 times with 0.05% Tween-20 in PBS. IRDye 800CW/680 LT Goat anti-rabbit and anti-mouse were used as secondary antibodies (Li-Cor Biosciences, Lincoln, LE) and membranes were imaged on Odyssey CLx infrared imaging system (Image Studio version 5.2.5, Li-Cor Biosciences).

Imaging and analysis of fixed cells

Images of fixed cells were collected with a Nikon Eclipse Ni upright fluorescence microscope equipped with a DS-Qi2 CMOS camera (Nikon), an Intensilight C-HGFI epi-fluorescence illuminator (Nikon), Plan Apo Lambda 100× NA 1.45 or Plan Apo Lambda 60x N.A. 1.40 oil objectives (Nikon) and driven by NIS-Elements Br software (Nikon).

Gated STED imaging was performed with Leica TCS SP8 STED 3X microscope driven by LAS X software using HC PL APO 100x/1.4 oil STED WHITE objective, white laser (633 nm) for excitation and 775 nm pulsed lased for depletion. Images were acquired in 2D STED mode with vortex phase mask. Depletion laser power was equal to 90% of maximum power and an internal Leica HyD hybrid detector with a time gate of $1 \leqslant tg \leqslant 8$ ns was used.

ImageJ was used for adjustments of intensity levels and contrast, quantification of the immunofluorescence signal intensity and maximum intensity projections. To analyze PCM clustering after nocodazole washout in AKAP450/CAMSAP2 knockout RPE1 cells, images were separated into concentric circular areas using Concentric Circles plugin of ImageJ. The biggest PCM cluster (which normally also had the highest fluorescence intensity) was selected as the center, around which 20 circles with 2 µm inner radius and 20 µm outer radius were drawn. Fluorescence intensity of PCM clusters in these concentric circles was measured automatically and normalized by the sum of the total PCM intensity in each cell per condition. To quantify the areas occupied by PCM clusters, immunofluorescence images of fixed cells and time lapse images of live cells were analyzed by drawing the smallest circle that covered visible PCM clusters to indicate the area occupied by the PCM clusters, and the diameters of the circles were used for the quantification.

Measurements of microtubule radiality

To analyze microtubule radiality, images of fluorescently labeled microtubules were separated into radial and non-radial components using a customized ImageJ macro (https://github.com/ekatrukha/radialitymap). First, a local orientation angle map was calculated for each pixel using the OrientationJ plugin. We used 'cubic spline gradient' method and tensor sigma parameter of 6 pixels (0.4 µm). The new origin of coordinates was specified by selecting the centrosome position in the corresponding channel, or the brightest spot in case of centrinone treatment. Radial local orientation angle was calculated as a difference between the local orientation angle and the angle of the vector drawn from the new origin of coordinates to the current pixel

position. A radial map image was calculated as an absolute value of the cosine of the radial local orientation angle at each pixel providing values between zero and one. A non-radial map image was calculated as one minus the radial map. Both maps were multiplied with the original image to account for different signal intensities; the two maps illustrate separated radial and non-radial image components.

Live cell imaging and analysis

Live fluorescent imaging was performed with spinning disk confocal microscopy on inverted research microscope Nikon EclipseTi-E (Nikon), equipped with the Perfect Focus System (Nikon), Nikon Plan Apo VC 60x NA 1.4 and Nikon Plan Apo VC 100x N.A. 1.40 oil objectives (Nikon) and spinning-disc confocal scanner unit (CSU-X1-A1, Yokogawa). The system was also equipped with ASI motorized stage with the piezo top plate MS-2000-XYZ (ASI), Photometrics Evolve 512 EMCCD camera (Photometrics) and controlled by the MetaMorph 7.8 software (Molecular Devices). Vortran Stradus lasers (405 nm 100 mW, 488 nm 150 mW and 642 nm 165 mW) and Cobolt Jive 561 nm 110 mW laser were used as the light sources. System was equipped with ET-DAPI (49000), ET-GFP (49002), ET-mCherry (49008) and ET-Cy5 (49006) filter sets (Chroma). 16-bit images were projected onto the EMCCD chip with the intermediate lens 2.0X (Edmund Optics) at a magnification of 110 nm per pixel (60x objective) and 67 nm per pixel (100x objective). To keep cells at 37°C and 5% CO_2 we used stage top incubator (INUBG2E-ZILCS, Tokai Hit). Cells were plated on round 25 mm coverslips, which were mounted in Attofluor Cell Chamber (Thermo fisher). Cells were imaged with a 2 s interval and 200 ms exposure for 1-3 hrs at 10% laser power.

For live imaging of nocodazole treatment and washout experiments, cells were incubated with the medium containing 100 nM SiR-tubulin (Tebu-bio) overnight to image the microtubule network. Centrinone B-treated cells were imaged for a desired period of time prior to the nocodazole treatment, and then nocodazole was added into the medium at a final concentration of 10 µM while imaging simultaneously. Culture medium was carefully removed when microtubules were completely depolymerized and washed with prewarmed medium six times to let microtubules regrow. GFP-CDK5RAP2 and SiR-tubulin imaging was performed with a 2 s interval with 200 ms exposure for 1-3 hrs in total, and maximum intensity projections, contrast adjustment and further processing was performed using ImageJ.

FRAP

FRAP experiments were performed on the spinning disc microscope describe above, equipped with iLas platform and using Targeted Laser Action options of iLas and controlled with iLas software (Roper Scientific, now Gataca Systems). Photobleaching in the GFP channel was performed with the 488 nm laser. For the FRAP analysis, Polygon ROIs were set in photobleached and non-bleached regions as well as in the background. The average fluorescence intensity was measured using ImageJ for each frame, the background intensity was subtracted from the bleached and non-bleached areas and normalized to the average of the frames acquired prior to the bleach. The mean fluorescence intensities of the images before photobleaching were set as 100%, and the subsequent relative recovery percentages were calculated. Time lapse acquisitions were corrected for drift with the ImageJ plugins Template Matching.

motor-PAINT and analysis

For motor-PAINT, a protocol published previously (Tas et al., 2017) was used, with minor adjustments. Cells were incubated with 50 nM SiR-tubulin and 500 nM verapamil overnight to allow fields of view suitable for imaging to be located before the addition of purified GST-DmKHC(1-421)-mNeonGreen. For nocodazole-treated samples, cells were first incubated with 10 µM nocodazole for 15 minutes at 37°C. A single nocodazole-treated or control sample was then transferred to an imaging chamber, and cells were subjected to extraction for 1 minute in extraction buffer (BRB80: 80 mM K-Pipes, 1 mM $MgCl_2$, 1 mM EGTA; pH 6.8, supplemented with 1M sucrose and 0.15% TritonX-100) pre-warmed to 37°C. Pre-warmed fixation buffer (BRB80 supplemented with 2% PFA) was added to this (i.e. final PFA concentration of 1%) and the solutions were mixed by gentle pipetting for 1 minute. This buffer was removed and the chamber was washed for 4 times for 1 minute in pre-warmed wash buffer (BRB80 supplemented with 1 µM Taxol) before adding imaging buffer (BRB80 supplemented with 583 µg/mL catalase, 42 µg/mL glucose oxidase, 1.7% w/v glucose, 1 mM DTT, 1 µM Taxol, and 5mM ATP). An aliquot of GST-DmKHC(1-421)-mNeonGreen motors was warmed, spun in the Airfuge at 20 psi for 5 minutes in a pre-chilled rotor to remove any aggregates, and then transferred to a clean tube prior to use. Motors were kept on ice and added locally to cells in 0.3 µl increments.

Imaging was performed immediately after sample preparation at room temperature on a Nikon Ti-E microscope equipped with a 100x Apo TIRF oil immersion objective (NA. 1.49) and Perfect Focus System 3 (Nikon). Excitation was achieved with a Lighthub-6 laser combiner (Omicron) containing a 647 nm laser (LuxX 140 mW, Omicron), a 488 nm laser (LuxX 200 mW, Omicron), and optics allowing for a tunable angle of incidence. Illumination was adjusted for (pseudo-) total internal reflection fluorescence (TIRF) microscopy. Emission light was separated from excitation light using a quad-band

polychroic mirror (ZT405/488/561/640rpc, Chroma), a quad-band emission filter (ZET405/488/561/640m, Chroma), and an additional single-band emission filter (ET525/50m for mNeonGreen emission, Chroma). Detection was achieved using a Hamamatsu Flash 4.0v2 sCMOS camera. Image stacks were acquired with a 60 ms exposure time, 7% laser power, and 15000-22000 images per field of view. Components were controlled using MicroManager (Edelstein et al., 2014).

Acquired stacks were pre-processed using the Faster Temporal Median ImageJ plugin (https://github.com/HohlbeinLab/FTM2; (Jabermoradi et al., 2021)) with a window size of 100 frames. These stacks were then analyzed using Detection of Molecules (DoM) plugin v.1.2.1 for ImageJ (https://github.com/ekatrukha/DoM_Utrecht), as has been described previously (Chazeau et al., 2016; Tas et al., 2017). Each image in an acquired stack is convoluted with a two-dimensional Mexican hat kernel. The resulting intensity histogram is used to create a thresholded mask based on a cut-off of three standard deviations above the mean. This mask is then subject to rounds of dilution and erosion to create a filtered mask used to calculate the centroids on the original image. These centroids are used as initial values to perform unweighted nonlinear least squares fitting with a Levenberg-Marquardt algorithm to an asymmetric two-dimensional Gaussian point spread function (PSF), allowing for the sub-pixel localization of particles.

Images were drift-corrected using DoM. The normalized cross-correlation between intermediate reconstructions of consecutive sub-stacks is used to calculate the drift in x and y between sub-stacks, which is then linearly interpolated to adjust each individual frame in the stack.

Detected particles were linked into tracks again using DoM, which performs a quicker variant of a nearest neighbor search, with a maximum distance of 5 pixels (~320nm) between consecutive frames and no permitted frame gap. Tracks were later filtered to remove those shorter than 4 frames or longer than 200 frames, those in which an angle between parts of the trajectory exceeded 90 degrees, and those in which the speed of the motor was less than 100nm/s or more than 1500nm/s.

The particle table was then split into four particle tables corresponding to the four quadrants of the image with tracks sorted based on their net displacement (i.e., $\Delta x>0 \wedge \Delta y>0$; $\Delta x>0 \wedge \Delta y<0$; $\Delta x<0 \wedge \Delta y>0$; $\Delta x<0 \wedge \Delta y<0$), as described previously (Tas et al., 2017). These directionality-filtered particle tables were reconstructed using DoM, creating four super-resolved images of microtubule segments pointing in a similar direction. These were merged with the reconstructed image of all localizations to determine the direction of each microtubule segment. Each microtubule was manually assessed to assign it as being plus-end-in or plus-end-out. Microtubules were manually traced with lines 4 pixels (80 nm) wide, assigned a color based on their orientation, flattened onto the image,

filtered with a Gaussian Blur of radius 2, and finally merged with the reconstructed image of all localizations.

To quantify the percentage of minus-end-out microtubule length to total microtubule length before and after nocodazole treatment, the length of each microtubule (determined from kinesin-1 trajectories) in the cell was measured by calculating the Euclidean distance between all subsequent pairs of points along the microtubule and summed. The ratio was calculated as the total minus-end-out microtubule length divided by the total microtubule length.

Analysis of PCM cluster dynamics

To represent the motion of PCM clusters during nocodazole treatment, ImageJ plugin KymoResliceWide v.0.4 (https://github.com/ekatrukha/KymoResliceWide) was used for generating kymographs from the time lapse images. The velocity of PCM clusters was measured manually using kymographs starting from the time point when a small PCM cluster moved out of an aMTOC. Microtubule density around each PCM cluster was determined by measuring the mean fluorescence intensity of SiR-tubulin in a circular area with a 2 µm radius centered on the PCM cluster and normalizing it to the mean fluorescence intensity of 20 images prior to nocodazole addition (set as 100%). The moment when a PCM cluster started to move out of the aMTOC was set as the initial time point (0 min), and the subsequent PCM cluster motion velocity and the relative local microtubule density at 43 time points were calculated and averaged.

The movement trajectories of PCM clusters were generated using ImageJ plugin TrackMate (version is 6.0.2). The parameters and the settings used were as following: LoG (Laplacian of Gaussian) detector with estimated blob diameter: 14.9 µm; thresholding value 12.25; sub-pixel localization was selected. HyperStack Displayer was selected to overlay the spots and tracks on the current hyperstack window. Simple LAP tracker was selected to track the distance and time with the linking max distance: 32.0 µm, gap-closing max distance: 55.0 µm and gap-closing max frame gap: 2. All other parameters and settings were used as the default.

Statistical analysis

All statistical analyses were performed using GraphPad Prism 9. Statistical details for each experiment can be found in the corresponding figure legends and supporting files.

Data and software availability

All mentioned ImageJ plugins have source code available and are licensed under open-source GNU GPL v3 license. The source data for the original Western blots are available within the paper.

Acknowledgements

We thank Lynne Cassimeris (Lehigh University, USA), Pierre Gönczy and Didier Trono (EPFL, Switzerland), Dr. Duane Compton (Geisel School of Medicine at Dartmouth, USA) and Dr. Laurence Pelletier (Lunenfeld-Tanenbaum Research Institute, Canada) for the gift of materials and Ilya Grigoriev and Eugene Katrukha (Biology Imaging Center, Utrecht University) for the help with imaging and image analysis. This work was supported by China Scholarship Council scholarships to Fangrui Chen, Jingchao Wu and Chao Yang, the Netherlands Organization for Scientific Research Spinoza prize to A.A, as well as the European Research Council Consolidator Grant 819219 to L.C.K. and the Eindhoven-Wageningen-Utrecht Alliance (www.ewuu.nl) that supports the Center for Living Technologies.

Competing financial interests

The authors declare no competing financial interests.

References

Abal, M., M. Piel, V. Bouckson-Castaing, M. Mogensen, J.B. Sibarita, and M. Bornens. 2002. Microtubule release from the centrosome in migrating cells. *J Cell Biol*. 159:731-737.

Akhmanova, A., C.C. Hoogenraad, K. Drabek, T. Stepanova, B. Dortland, T. Verkerk, W. Vermeulen, B.M. Burgering, C.I. De Zeeuw, F. Grosveld, and N. Galjart. 2001. Clasps are CLIP-115 and -170 associating proteins involved in the regional regulation of microtubule dynamics in motile fibroblasts. *Cell*. 104:923-935.

Balczon, R., C.E. Varden, and T.A. Schroer. 1999. Role for microtubules in centrosome doubling in Chinese hamster ovary cells. *Cell Motil Cytoskeleton*. 42:60-72.

Balestra, F.R., A. Dominguez-Calvo, B. Wolf, C. Busso, A. Buff, T. Averink, M. Lipsanen-Nyman, P. Huertas, R.M. Rios, and P. Gonczy. 2021. TRIM37 prevents formation of centriolar protein assemblies by regulating Centrobin. *Elife*. 10:e62640.

Burakov, A., O. Kovalenko, I. Semenova, O. Zhapparova, E. Nadezhdina, and V. Rodionov. 2008. Cytoplasmic dynein is involved in the retention of microtubules at the centrosome in interphase cells. *Traffic*. 9:472-480.

Cassimeris, L., and J. Morabito. 2004. TOGp, the human homolog of XMAP215/Dis1, is required for centrosome integrity, spindle pole organization, and bipolar spindle assembly. *Mol Biol Cell*. 15:1580-1590.

Charrasse, S., M. Schroeder, C. Gauthier-Rouviere, F. Ango, L. Cassimeris, D.L. Gard, and C. Larroque. 1998. The TOGp protein is a new human microtubule-associated protein homologous to the Xenopus XMAP215. *J Cell Sci*. 111 (Pt 10):1371-1383.

Chazeau, A., E.A. Katrukha, C.C. Hoogenraad, and L.C. Kapitein. 2016. Studying neuronal microtubule organization and microtubule-associated proteins using single molecule localization microscopy. *Methods Cell Biol*. 131:127-149.

Chen, C.T., H. Hehnly, Q. Yu, D. Farkas, G. Zheng, S.D. Redick, H.F. Hung, R. Samtani, A. Jurczyk, S. Akbarian, C. Wise, A. Jackson, M. Bober, Y. Guo, C. Lo, and S. Doxsey. 2014. A unique set of centrosome proteins requires pericentrin for spindle-pole localization and spindle orientation. *Curr Biol*. 24:2327-2334.

Chi, W., G. Wang, G. Xin, Q. Jiang, and C. Zhang. 2021. PLK4-phosphorylated NEDD1 facilitates cartwheel assembly and centriole biogenesis initiations. *J Cell Biol*. 220:e202002151.

Chinen, T., S. Yamamoto, Y. Takeda, K. Watanabe, K. Kuroki, K. Hashimoto, D. Takao, and D. Kitagawa. 2020. NuMA assemblies organize microtubule asters to establish spindle bipolarity in acentrosomal human cells. *EMBO J*. 39:e102378.

Chinen, T., K. Yamazaki, K. Hashimoto, K. Fujii, K. Watanabe, Y. Takeda, S. Yamamoto, Y. Nozaki, Y. Tsuchiya, D. Takao, and D. Kitagawa. 2021. Centriole and PCM cooperatively recruit CEP192 to spindle poles to promote bipolar spindle assembly. *J Cell Biol*. 220:e202006085.

Choi, Y.K., P. Liu, S.K. Sze, C. Dai, and R.Z. Qi. 2010. CDK5RAP2 stimulates microtubule nucleation by the gamma-tubulin ring complex. *J Cell Biol*. 191:1089-1095.

Chong, W.M., W.J. Wang, C.H. Lo, T.Y. Chiu, T.J. Chang, Y.P. Liu, B. Tanos, G. Mazo, M.B. Tsou, W.N. Jane, T.T. Yang, and J.C. Liao. 2020. Super-resolution microscopy reveals coupling between mammalian centriole subdistal appendages and distal appendages. *Elife*. 9:e53580.

847 Cizmecioglu, O., M. Arnold, R. Bahtz, F. Settele, L. Ehret, U. Haselmann-Weiss, C. Antony, and I.
848 Hoffmann. 2010. Cep152 acts as a scaffold for recruitment of Plk4 and CPAP to the
849 centrosome. *Journal of Cell Biology*. 191:731-739.

850 Conduit, P.T., A. Wainman, and J.W. Raff. 2015. Centrosome function and assembly in animal cells.
851 *Nat Rev Mol Cell Biol*. 16:611-624.

852 Delaval, B., and S.J. Doxsey. 2010. Pericentrin in cellular function and disease. *J Cell Biol*. 188:181-
853 190.

854 Delgehyr, N., J. Sillibourne, and M. Bornens. 2005. Microtubule nucleation and anchoring at the
855 centrosome are independent processes linked by ninein function. *J Cell Sci*. 118:1565-1575.

856 Edelstein, A.D., M.A. Tsuchida, N. Amodaj, H. Pinkard, R.D. Vale, and N. Stuurman. 2014. Advanced
857 methods of microscope control using muManager software. *J Biol Methods*. 1:e10.

858 Efimov, A., A. Kharitonov, N. Efimova, J. Loncarek, P.M. Miller, N. Andreyeva, P. Gleeson, N. Galjart,
859 A.R. Maia, I.X. McLeod, J.R. Yates, 3rd, H. Maiato, A. Khodjakov, A. Akhmanova, and I.
860 Kaverina. 2007. Asymmetric CLASP-dependent nucleation of noncentrosomal microtubules
861 at the trans-Golgi network. *Dev Cell*. 12:917-930.

862 Fong, C.S., G. Mazo, T. Das, J. Goodman, M. Kim, B.P. O'Rourke, D. Izquierdo, and M.F. Tsou. 2016.
863 53BP1 and USP28 mediate p53-dependent cell cycle arrest in response to centrosome loss
864 and prolonged mitosis. *Elife*. 5:e16270.

865 Fong, K.W., Y.K. Choi, J.B. Rattner, and R.Z. Qi. 2008. CDK5RAP2 is a pericentriolar protein that
866 functions in centrosomal attachment of the gamma-tubulin ring complex. *Mol Biol Cell*.
867 19:115-125.

868 Fu, J.Y., and D.M. Glover. 2012. Structured illumination of the interface between centriole and peri-
869 centriolar material. *Open Biology*. 2:120104.

870 Fu, M.M., T.S. McAlear, H. Nguyen, J.A. Oses-Prieto, A. Valenzuela, R.D. Shi, J.J. Perrino, T.T. Huang,
871 A.L. Burlingame, S. Bechstedt, and B.A. Barres. 2019. The Golgi Outpost Protein TPPP
872 Nucleates Microtubules and Is Critical for Myelination. *Cell*. 179:132-146.

873 Ganem, N.J., and D.A. Compton. 2004. The KinI kinesin Kif2a is required for bipolar spindle assembly
874 through a functional relationship with MCAK. *J Cell Biol*. 166:473-478.

875 Ganem, N.J., K. Upton, and D.A. Compton. 2005. Efficient mitosis in human cells lacking poleward
876 microtubule flux. *Curr Biol*. 15:1827-1832.

877 Garbrecht, J., T. Laos, E. Holzer, M. Dillinger, and A. Dammermann. 2021. An acentriolar centrosome
878 at the C. elegans ciliary base. *Curr Biol*. 31:2418-2428.

879 Gartenmann, L., C.C. Vicente, A. Wainman, Z.A. Novak, B. Sieber, J.H. Richens, and J.W. Raff. 2020.
880 Drosophila Sas-6, Ana2 and Sas-4 self-organise into macromolecular structures that can be
881 used to probe centriole and centrosome assembly. *J Cell Sci*. 133:jcs244574.

882 Gavilan, M.P., P. Gandolfo, F.R. Balestra, F. Arias, M. Bornens, and R.M. Rios. 2018. The dual role of
883 the centrosome in organizing the microtubule network in interphase. *EMBO Rep*. 19:e45942.

884 Gimpel, P., Y.L. Lee, R.M. Sobota, A. Calvi, V. Koullourou, R. Patel, K. Mamchaoui, F. Nedelec, S.
885 Shackleton, J. Schmoranzer, B. Burke, B. Cadot, and E.R. Gomes. 2017. Nesprin-1alpha-
886 Dependent Microtubule Nucleation from the Nuclear Envelope via Akap450 Is Necessary for
887 Nuclear Positioning in Muscle Cells. *Curr Biol*. 27:2999-3009.

888 Goldspink, D.A., C. Rookyard, B.J. Tyrrell, J. Gadsby, J. Perkins, E.K. Lund, N. Galjart, P. Thomas, T.
889 Wileman, and M.M. Mogensen. 2017. Ninein is essential for apico-basal microtubule

formation and CLIP-170 facilitates its redeployment to non-centrosomal microtubule organizing centres. *Open Biol*. 7:160274.

Gomez-Ferreria, M.A., M. Bashkurov, A.O. Helbig, B. Larsen, T. Pawson, A.C. Gingras, and L. Pelletier. 2012. Novel NEDD1 phosphorylation sites regulate gamma-tubulin binding and mitotic spindle assembly. *J Cell Sci*. 125:3745-3751.

Gomez-Ferreria, M.A., U. Rath, D.W. Buster, S.K. Chanda, J.S. Caldwell, D.R. Rines, and D.J. Sharp. 2007. Human Cep192 is required for mitotic centrosome and spindle assembly. *Curr Biol*. 17:1960-1966.

Grigoriev, I., S.M. Gouveia, B. van der Vaart, J. Demmers, J.T. Smyth, S. Honnappa, D. Splinter, M.O. Steinmetz, J.W. Putney, Jr., C.C. Hoogenraad, and A. Akhmanova. 2008. STIM1 is a MT-plus-end-tracking protein involved in remodeling of the ER. *Curr Biol*. 18:177-182.

Haren, L., M.H. Remy, I. Bazin, I. Callebaut, M. Wright, and A. Merdes. 2006. NEDD1-dependent recruitment of the gamma-tubulin ring complex to the centrosome is necessary for centriole duplication and spindle assembly. *J Cell Biol*. 172:505-515.

Haren, L., T. Stearns, and J. Luders. 2009. Plk1-dependent recruitment of gamma-tubulin complexes to mitotic centrosomes involves multiple PCM components. *PLoS One*. 4:e5976.

Hoogenraad, C.C., P. Wulf, N. Schiefermeier, T. Stepanova, N. Galjart, J.V. Small, F. Grosveld, C.I. de Zeeuw, and A. Akhmanova. 2003. Bicaudal D induces selective dynein-mediated microtubule minus end-directed transport. *Embo J*. 22:6004-6015.

Jabermoradi, A., S. Yang, M. Gobes, J.P.M. van Duynhoven, and H. J. 2021. Enabling single-molecule localization microscopy in turbid food emulsions. *bioRxiv*:2021.2003.2003.433739.

Jia, Y., K.W. Fong, Y.K. Choi, S.S. See, and R.Z. Qi. 2013. Dynamic recruitment of CDK5RAP2 to centrosomes requires its association with dynein. *PLoS One*. 8:e68523.

Jiang, K., S. Hua, R. Mohan, I. Grigoriev, K.W. Yau, Q. Liu, E.A. Katrukha, A.F. Altelaar, A.J. Heck, C.C. Hoogenraad, and A. Akhmanova. 2014. Microtubule minus-end stabilization by polymerization-driven CAMSAP deposition. *Dev Cell*. 28:295-309.

Jiang, X., D. Bang Tam Ho, K. Mahe, J. Mia, G. Sepulveda, M. Antkowiak, L. Jiang, S. Yamada, and L.-E. Jao. 2020. Condensation of pericentrin proteins in human cells illuminates phase separation in centrosome assembly. *bioRxiv*:2020.2005.2008.084749.

Jonsson, E., M. Yamada, R.D. Vale, and G. Goshima. 2015. Clustering of a kinesin-14 motor enables processive retrograde microtubule-based transport in plants. *Nat Plants*. 1:15087.

Joukov, V., J.C. Walter, and A. De Nicolo. 2014. The Cep192-organized aurora A-Plk1 cascade is essential for centrosome cycle and bipolar spindle assembly. *Mol Cell*. 55:578-591.

Khanal, I., A. Elbediwy, C. Diaz de la Loza Mdel, G.C. Fletcher, and B.J. Thompson. 2016. Shot and Patronin polarise microtubules to direct membrane traffic and biogenesis of microvilli in epithelia. *J Cell Sci*. 129:2651-2659.

Khodjakov, A., R.W. Cole, B.R. Oakley, and C.L. Rieder. 2000. Centrosome-independent mitotic spindle formation in vertebrates. *Curr Biol*. 10:59-67.

Kim, S., and K. Rhee. 2014. Importance of the CEP215-pericentrin interaction for centrosome maturation during mitosis. *PLoS One*. 9:e87016.

Kim, T.S., J.E. Park, A. Shukla, S. Choi, R.N. Murugan, J.H. Lee, M. Ahn, K. Rhee, J.K. Bang, B.Y. Kim, J. Loncarek, R.L. Erikson, and K.S. Lee. 2013. Hierarchical recruitment of Plk4 and regulation of

centriole biogenesis by two centrosomal scaffolds, Cep192 and Cep152. *Proc Natl Acad Sci U S A*. 110:E4849-4857.

Kohlmaier, G., J. Loncarek, X. Meng, B.F. McEwen, M.M. Mogensen, A. Spektor, B.D. Dynlacht, A. Khodjakov, and P. Gonczy. 2009. Overly Lona Centrioles and Defective Cell Division upon Excess of the SAS-4-Related Protein CPAP. *Current Biology*. 19:1012-1018.

Kolano, A., S. Brunet, A.D. Silk, D.W. Cleveland, and M.H. Verlhac. 2012. Error-prone mammalian female meiosis from silencing the spindle assembly checkpoint without normal interkinetochore tension. *Proc Natl Acad Sci U S A*. 109:E1858-1867.

Komarova, Y., G. Lansbergen, N. Galjart, F. Grosveld, G.G. Borisy, and A. Akhmanova. 2005. EB1 and EB3 control CLIP dissociation from the ends of growing microtubules. *Mol Biol Cell*. 16:5334-5345.

Lambrus, B.G., V. Daggubati, Y. Uetake, P.M. Scott, K.M. Clutario, G. Sluder, and A.J. Holland. 2016. A USP28-53BP1-p53-p21 signaling axis arrests growth after centrosome loss or prolonged mitosis. *J Cell Biol*. 214:143-153.

Lansbergen, G., Y. Komarova, M. Modesti, C. Wyman, C.C. Hoogenraad, H.V. Goodson, R.P. Lemaitre, D.N. Drechsel, E. van Munster, T.W.J. Gadella Jr., F. Grosveld, N. Galjart, G.G. Borisy, and A. Akhmanova. 2004. Conformational changes in CLIP-170 regulate its binding to microtubules and dynactin localisation. *J Cell Biol*. 166:1003-1014.

Lawo, S., M. Bashkurov, M. Mullin, M.G. Ferreria, R. Kittler, B. Habermann, A. Tagliaferro, I. Poser, J.R. Hutchins, B. Hegemann, D. Pinchev, F. Buchholz, J.M. Peters, A.A. Hyman, A.C. Gingras, and L. Pelletier. 2009. HAUS, the 8-subunit human Augmin complex, regulates centrosome and spindle integrity. *Curr Biol*. 19:816-826.

Lawo, S., M. Hasegan, G.D. Gupta, and L. Pelletier. 2012. Subdiffraction imaging of centrosomes reveals higher-order organizational features of pericentriolar material. *Nat Cell Biol*. 14:1148-1158.

Lechler, T., and E. Fuchs. 2007. Desmoplakin: an unexpected regulator of microtubule organization in the epidermis. *J Cell Biol*. 176:147-154.

Lee, K., and K. Rhee. 2011. PLK1 phosphorylation of pericentrin initiates centrosome maturation at the onset of mitosis. *J Cell Biol*. 195:1093-1101.

Lee, S., and K. Rhee. 2010. CEP215 is involved in the dynein-dependent accumulation of pericentriolar matrix proteins for spindle pole formation. *Cell Cycle*. 9:774-783.

Liang, X., M. Kokes, R.D. Fetter, M.D. Sallee, A.W. Moore, J.L. Feldman, and K. Shen. 2020. Growth cone-localized microtubule organizing center establishes microtubule orientation in dendrites. *Elife*. 9:e56547.

Lin, Y.N., C.T. Wu, Y.C. Lin, W.B. Hsu, C.J. Tang, C.W. Chang, and T.K. Tang. 2013. CEP120 interacts with CPAP and positively regulates centriole elongation. *J Cell Biol*. 202:211-219.

Luders, J., U.K. Patel, and T. Stearns. 2006. GCP-WD is a gamma-tubulin targeting factor required for centrosomal and chromatin-mediated microtubule nucleation. *Nat Cell Biol*. 8:137-147.

Magescas, J., S. Eskinazi, M.V. Tran, and J.L. Feldman. 2021. Centriole-less pericentriolar material serves as a microtubule organizing center at the base of C. elegans sensory cilia. *Curr Biol*. 31:2410-2417.

Martin, M., and A. Akhmanova. 2018. Coming into Focus: Mechanisms of Microtubule Minus-End Organization. *Trends Cell Biol*. 28:574-588.

975 Martin, M., A. Veloso, J. Wu, E.A. Katrukha, and A. Akhmanova. 2018. Control of endothelial cell
976 polarity and sprouting angiogenesis by non-centrosomal microtubules. *Elife*. 7:e33864.

977 Meiring, J.C.M., B.I. Shneyer, and A. Akhmanova. 2020. Generation and regulation of microtubule
978 network asymmetry to drive cell polarity. *Curr Opin Cell Biol*. 62:86-95.

979 Meitinger, F., J.V. Anzola, M. Kaulich, A. Richardson, J.D. Stender, C. Benner, C.K. Glass, S.F. Dowdy,
980 A. Desai, A.K. Shiau, and K. Oegema. 2016. 53BP1 and USP28 mediate p53 activation and G1
981 arrest after centrosome loss or extended mitotic duration. *J Cell Biol*. 214:155-166.

982 Meitinger, F., M. Ohta, K.Y. Lee, S. Watanabe, R.L. Davis, J.V. Anzola, R. Kabeche, D.A. Jenkins, A.K.
983 Shiau, A. Desai, and K. Oegema. 2020. TRIM37 controls cancer-specific vulnerability to PLK4
984 inhibition. *Nature*. 585:440-446.

985 Meng, W., Y. Mushika, T. Ichii, and M. Takeichi. 2008. Anchorage of microtubule minus ends to
986 adherens junctions regulates epithelial cell-cell contacts. *Cell*. 135:948-959.

987 Mennella, V., D.A. Agard, B. Huang, and L. Pelletier. 2014. Amorphous no more: subdiffraction view
988 of the pericentriolar material architecture. *Trends Cell Biol*. 24:188-197.

989 Mennella, V., B. Keszthelyi, K.L. McDonald, B. Chhun, F. Kan, G.C. Rogers, B. Huang, and D.A. Agard.
990 2012. Subdiffraction-resolution fluorescence microscopy reveals a domain of the
991 centrosome critical for pericentriolar material organization. *Nat Cell Biol*. 14:1159-1168.

992 Meraldi, P. 2016. Centrosomes in spindle organization and chromosome segregation: a mechanistic
993 view. *Chromosome Res*. 24:19-34.

994 Mimori-Kiyosue, Y., I. Grigoriev, G. Lansbergen, H. Sasaki, C. Matsui, F. Severin, N. Galjart, F.
995 Grosveld, I. Vorobjev, S. Tsukita, and A. Akhmanova. 2005. CLASP1 and CLASP2 bind to EB1
996 and regulate microtubule plus-end dynamics at the cell cortex. *J Cell Biol*. 168:141-153.

997 Mogensen, M.M., A. Malik, M. Piel, V. Bouckson-Castaing, and M. Bornens. 2000. Microtubule
998 minus-end anchorage at centrosomal and non-centrosomal sites: the role of ninein. *J Cell Sci*.
999 113 (Pt 17):3013-3023.

1000 Muroyama, A., and T. Lechler. 2017. Microtubule organization, dynamics and functions in
1001 differentiated cells. *Development*. 144:3012-3021.

1002 Nijenhuis, W., M.M.P. van Grinsven, and L.C. Kapitein. 2020. An optimized toolbox for the
1003 optogenetic control of intracellular transport. *J Cell Biol*. 219:e201907149.

1004 Noordstra, I., Q. Liu, W. Nijenhuis, S. Hua, K. Jiang, M. Baars, S. Remmelzwaal, M. Martin, L.C.
1005 Kapitein, and A. Akhmanova. 2016. Control of apico-basal epithelial polarity by the
1006 microtubule minus-end-binding protein CAMSAP3 and spectraplakin ACF7. *J Cell Sci*.
1007 129:4278-4288.

1008 Oddoux, S., K.J. Zaal, V. Tate, A. Kenea, S.A. Nandkeolyar, E. Reid, W.H. Liu, and E. Ralston. 2013.
1009 Microtubules that form the stationary lattice of muscle fibers are dynamic and nucleated at
1010 Golgi elements. *Journal of Cell Biology*. 203:205-213.

1011 Paz, J., and J. Luders. 2017. Microtubule-Organizing Centers: Towards a Minimal Parts List. *Trends*
1012 *Cell Biol*:S0962-8924(0917)30187-30183.

1013 Pollock, R., R. Issner, K. Zoller, S. Natesan, V.M. Rivera, and T. Clackson. 2000. Delivery of a stringent
1014 dimerizer-regulated gene expression system in a single retroviral vector. *Proc Natl Acad Sci U*
1015 *S A*. 97:13221-13226.

1016 Pongrakhananon, V., H. Saito, S. Hiver, T. Abe, G. Shioi, W. Meng, and M. Takeichi. 2018. CAMSAP3
1017 maintains neuronal polarity through regulation of microtubule stability. *Proc Natl Acad Sci U*
1018 *S A*. 115:9750-9755.

1019 Prosser, S.L., and L. Pelletier. 2020. Centriolar satellite biogenesis and function in vertebrate cells. *J*
1020 *Cell Sci*. 133:jcs239566.

1021 Purohit, A., S.H. Tynan, R. Vallee, and S.J. Doxsey. 1999. Direct interaction of pericentrin with
1022 cytoplasmic dynein light intermediate chain contributes to mitotic spindle organization. *J*
1023 *Cell Biol*. 147:481-492.

1024 Raff, J.W. 2019. Phase Separation and the Centrosome: A Fait Accompli? *Trends Cell Biol*. 29:612-
1025 622.

1026 Ran, F.A., P.D. Hsu, J. Wright, V. Agarwala, D.A. Scott, and F. Zhang. 2013. Genome engineering using
1027 the CRISPR-Cas9 system. *Nat Protoc*. 8:2281-2308.

1028 Redwine, W.B., M.E. DeSantis, I. Hollyer, Z.M. Htet, P.T. Tran, S.K. Swanson, L. Florens, M.P.
1029 Washburn, and S.L. Reck-Peterson. 2017. The human cytoplasmic dynein interactome
1030 reveals novel activators of motility. *Elife*. 6:e28257.

1031 Rios, R.M. 2014. The centrosome-Golgi apparatus nexus. *Philos Trans R Soc Lond B Biol Sci*.
1032 369:20130462.

1033 Rivero, S., J. Cardenas, M. Bornens, and R.M. Rios. 2009. Microtubule nucleation at the cis-side of
1034 the Golgi apparatus requires AKAP450 and GM130. *EMBO J*. 28:1016-1028.

1035 Sallee, M.D., and J.L. Feldman. 2021. Microtubule organization across cell types and states. *Curr Biol*.
1036 31:R506-R511.

1037 Schlager, M.A., A. Serra-Marques, I. Grigoriev, L.F. Gumy, M. Esteves da Silva, P.S. Wulf, A.
1038 Akhmanova, and C.C. Hoogenraad. 2014. Bicaudal d family adaptor proteins control the
1039 velocity of Dynein-based movements. *Cell Rep*. 8:1248-1256.

1040 Schmidt, T.I., J. Kleylein-Sohn, J. Westendorf, M. Le Clech, S.B. Lavoie, Y.D. Stierhof, and E.A. Nigg.
1041 2009. Control of centriole length by CPAP and CP110. *Curr Biol*. 19:1005-1011.

1042 Shinohara, H., N. Sakayori, M. Takahashi, and N. Osumi. 2013. Ninein is essential for the
1043 maintenance of the cortical progenitor character by anchoring the centrosome to
1044 microtubules. *Biol Open*. 2:739-749.

1045 Sonnen, K.F., A.M. Gabryjonczyk, E. Anselm, Y.D. Stierhof, and E.A. Nigg. 2013. Human Cep192 and
1046 Cep152 cooperate in Plk4 recruitment and centriole duplication. *J Cell Sci*. 126:3223-3233.

1047 Sonnen, K.F., L. Schermelleh, H. Leonhardt, and E.A. Nigg. 2012. 3D-structured illumination
1048 microscopy provides novel insight into architecture of human centrosomes. *Biology Open*.
1049 1:965-976.

1050 Spektor, A., W.Y. Tsang, D. Khoo, and B.D. Dynlacht. 2007. Cep97 and CP110 suppress a cilia
1051 assembly program. *Cell*. 130:678-690.

1052 Splinter, D., M.E. Tanenbaum, A. Lindqvist, D. Jaarsma, A. Flotho, K.L. Yu, I. Grigoriev, D. Engelsma,
1053 E.D. Haasdijk, N. Keijzer, J. Demmers, M. Fornerod, F. Melchior, C.C. Hoogenraad, R.H.
1054 Medema, and A. Akhmanova. 2010. Bicaudal D2, dynein and kinesin-1 associate with nuclear
1055 pore complexes and regulate centrosome and nuclear positioning during mitotic entry. *PLoS*
1056 *Biol*. 8:e1000350.

1057 Steinman, J.B., C.C. Santarossa, R.M. Miller, L.S. Yu, A.S. Serpinskaya, H. Furukawa, S. Morimoto, Y.
1058 Tanaka, M. Nishitani, M. Asano, R. Zalyte, A.E. Ondrus, A.G. Johnson, F. Ye, M.V. Nachury, Y.

Fukase, K. Aso, M.A. Foley, V.I. Gelfand, J.K. Chen, A.P. Carter, and T.M. Kapoor. 2017. Chemical structure-guided design of dynapyrazoles, cell-permeable dynein inhibitors with a unique mode of action. *Elife*. 6:e25174.

Stolz, A., N. Ertych, and H. Bastians. 2015. A phenotypic screen identifies microtubule plus end assembly regulators that can function in mitotic spindle orientation. *Cell Cycle*. 14:827-837.

Takahashi, M., A. Yamagiwa, T. Nishimura, H. Mukai, and Y. Ono. 2002. Centrosomal proteins CG-NAP and kendrin provide microtubule nucleation sites by anchoring gamma-tubulin ring complex. *Mol Biol Cell*. 13:3235-3245.

Tanaka, N., W. Meng, S. Nagae, and M. Takeichi. 2012. Nezha/CAMSAP3 and CAMSAP2 cooperate in epithelial-specific organization of noncentrosomal microtubules. *Proc Natl Acad Sci U S A*. 109:20029-20034.

Tang, C.J.C., R.H. Fu, K.S. Wu, W.B. Hsu, and T.K. Tang. 2009. CPAP is a cell-cycle regulated protein that controls centriole length. *Nat Cell Biol*. 11:825-831.

Tas, R.P., A. Chazeau, B.M.C. Cloin, M.L.A. Lambers, C.C. Hoogenraad, and L.C. Kapitein. 2017. Differentiation between Oppositely Oriented Microtubules Controls Polarized Neuronal Transport. *Neuron*. 96:1264-1271.

Tibelius, A., J. Marhold, H. Zentgraf, C.E. Heilig, H. Neitzel, B. Ducommun, A. Rauch, A.D. Ho, J. Bartek, and A. Kramer. 2009. Microcephalin and pericentrin regulate mitotic entry via centrosome-associated Chk1. *J Cell Biol*. 185:1149-1157.

Toya, M., S. Kobayashi, M. Kawasaki, G. Shioi, M. Kaneko, T. Ishiuchi, K. Misaki, W. Meng, and M. Takeichi. 2016. CAMSAP3 orients the apical-to-basal polarity of microtubule arrays in epithelial cells. *Proc Natl Acad Sci U S A*. 113:332-337.

Vergarajauregui, S., R. Becker, U. Steffen, M. Sharkova, T. Esser, J. Petzold, F. Billing, M.S. Kapiloff, G. Schett, I. Thievessen, and F.B. Engel. 2020. AKAP6 orchestrates the nuclear envelope microtubule-organizing center by linking golgi and nucleus via AKAP9. *Elife*. 9:e61669.

Vinopal, S., M. Cernohorska, V. Sulimenko, T. Sulimenko, V. Vosecka, M. Flemr, E. Draberova, and P. Draber. 2012. gamma-Tubulin 2 nucleates microtubules and is downregulated in mouse early embryogenesis. *PLoS One*. 7:e29919.

Wang, G., Q. Chen, X. Zhang, B. Zhang, X. Zhuo, J. Liu, Q. Jiang, and C. Zhang. 2013. PCM1 recruits Plk1 to the pericentriolar matrix to promote primary cilia disassembly before mitotic entry. *J Cell Sci*. 126:1355-1365.

Wang, S., D. Wu, S. Quintin, R.A. Green, D.K. Cheerambathur, S.D. Ochoa, A. Desai, and K. Oegema. 2015. NOCA-1 functions with gamma-tubulin and in parallel to Patronin to assemble non-centrosomal microtubule arrays in C. elegans. *Elife*. 4:e08649.

Watanabe, S., F. Meitinger, A.K. Shiau, K. Oegema, and A. Desai. 2020. Centriole-independent mitotic spindle assembly relies on the PCNT-CDK5RAP2 pericentriolar matrix. *J Cell Biol*. 219:e202006010.

Wong, Y.L., J.V. Anzola, R.L. Davis, M. Yoon, A. Motamedi, A. Kroll, C.P. Seo, J.E. Hsia, S.K. Kim, J.W. Mitchell, B.J. Mitchell, A. Desai, T.C. Gahman, A.K. Shiau, and K. Oegema. 2015. Cell biology. Reversible centriole depletion with an inhibitor of Polo-like kinase 4. *Science*. 348:1155-1160.

Woodruff, J.B., B. Ferreira Gomes, P.O. Widlund, J. Mahamid, A. Honigmann, and A.A. Hyman. 2017. The Centrosome Is a Selective Condensate that Nucleates Microtubules by Concentrating Tubulin. *Cell*. 169:1066-1077.

Wu, J., C. de Heus, Q. Liu, B.P. Bouchet, I. Noordstra, K. Jiang, S. Hua, M. Martin, C. Yang, I. Grigoriev, E.A. Katrukha, A.F. Altelaar, C.C. Hoogenraad, R.Z. Qi, J. Klumperman, and A. Akhmanova. 2016. Molecular Pathway of Microtubule Organization at the Golgi Apparatus. *Dev Cell*. 39:44-60.

Yang, C., J. Wu, C. de Heus, I. Grigoriev, N. Liv, Y. Yao, I. Smal, E. Meijering, J. Klumperman, R.Z. Qi, and A. Akhmanova. 2017. EB1 and EB3 regulate microtubule minus end organization and Golgi morphology. *J Cell Biol*. 216:3179-3198.

Yang, R., and J.L. Feldman. 2015. SPD-2/CEP192 and CDK Are Limiting for Microtubule-Organizing Center Function at the Centrosome. *Curr Biol*. 25:1924-1931.

Yau, K.W., S.F. van Beuningen, I. Cunha-Ferreira, B.M. Cloin, E.Y. van Battum, L. Will, P. Schatzle, R.P. Tas, J. van Krugten, E.A. Katrukha, K. Jiang, P.S. Wulf, M. Mikhaylova, M. Harterink, R.J. Pasterkamp, A. Akhmanova, L.C. Kapitein, and C.C. Hoogenraad. 2014. Microtubule minus-end binding protein CAMSAP2 controls axon specification and dendrite development. *Neuron*. 82:1058-1073.

Yeow, Z.Y., B.G. Lambrus, R. Marlow, K.H. Zhan, M.A. Durin, L.T. Evans, P.M. Scott, T. Phan, E. Park, L.A. Ruiz, D. Moralli, E.G. Knight, L.M. Badder, D. Novo, S. Haider, C.M. Green, A.N.J. Tutt, C.J. Lord, J.R. Chapman, and A.J. Holland. 2020. Targeting TRIM37-driven centrosome dysfunction in 17q23-amplified breast cancer. *Nature*. 585:447-452.

Zheng, Y., R.A. Buchwalter, C. Zheng, E.M. Wight, J.V. Chen, and T.L. Megraw. 2020. A perinuclear microtubule-organizing centre controls nuclear positioning and basement membrane secretion. *Nat Cell Biol*. 22:297-309.

Zhu, F., S. Lawo, A. Bird, D. Pinchev, A. Ralph, C. Richter, T. Muller-Reichert, R. Kittler, A.A. Hyman, and L. Pelletier. 2008. The mammalian SPD-2 ortholog Cep192 regulates centrosome biogenesis. *Curr Biol*. 18:136-141.

Zhu, X.D., and I. Kaverina. 2013. Golgi as an MTOC: making microtubules for its own good. *Histochemistry and Cell Biology*. 140:361-367.

Figure legends.

Figure 1. Formation and characterization of aMTOCs in AKAP450/CAMSAP2 knockout cells

(A) Immunofluorescence images of control or centrinone B-treated wild type (WT) RPE1 cells stained for centrioles (CEP135, red; centrin, green). The zooms of the boxed area show the centrioles stained with the indicated markers.

(B) Quantification shows the percentage of cells with centrioles before and after the centrinone treatment. 350 cells (n=7 fields of view) analyzed for each measurement in three independent experiments. The statistical significance was determined by unpaired two-tailed Mann-Whitney test in Prism 9.1 (***p<0.001). Values represent mean±SD.

(C) Immunofluorescence images of centrinone-treated WT RPE1 cells stained for pericentrin (PCNT, green) and the Golgi marker GM130 (red). Inset shows the merged image of the boxed area.

(D) Diagrams of the microtubule organization in WT and knockout (KO) cells used.

(E) Immunofluorescence images of centrinone-treated WT and knockout RPE1 cell lines stained for pericentrin (green) and microtubules (α-tubulin, red). Enlargements of the boxed areas are shown in the bottom row.

(F) Immunofluorescence images of centrinone-treated AKAP450/CAMSAP2 knockout RPE1 cells stained for different PCM components as indicated and imaged by STED microscopy.

(G) Quantification of the length and width of cylindrical PCM clusters. n=65 cells analyzed in three independent experiments. Values represent mean±SD.

(H) (Top left) Two frames of time-lapse images of centrinone-treated AKAP450/CAMSAP2 knockout RPE1 cells stably expressing GFP-CDK5RAP2 prior to FRAP experiments. (Top right) Schemes show regions of aMTOC where photobleaching was performed. (Middle) Kymographs illustrating fluorescence of unbleached aMTOC (No FRAP), fully photobleached aMTOC (Whole FRAP) and partially photobleached MTOC (Partial FRAP). (Bottom) Time-lapse images illustrating partial FRAP of a compact aMTOC. Time is min:sec.

(I) Normalized fluorescence intensity as a function of time. The blue line shows averaged intensity traces of unbleached MTOCs (No FRAP), the black line shows averaged intensity traces of fully photobleached MTOCs (Whole FRAP), the red line shows averaged intensity traces of whole MTOC that were partially photobleached (whole MTOC intensity, Partial FRAP) and the green line shows averaged intensity traces of the photobleached region of the partially photobleached MTOC (FRAP region intensity, Partial FRAP). n=3 for No FRAP, 3 for Whole FRAP, 5 for Partial FRAP (whole MTOC

intensity) and 5 for Partial FRAP (FRAP region intensity); time-lapse images of ~1600 timepoints with 2 s interval were analyzed for each measurement. Values are mean±SD.

Figure 2. Molecular composition of aMTOCs in AKAP450/CAMSAP2 knockout cells

(A-C) Immunofluorescence images of control or centrinone-treated AKAP450/CAMSAP2 knockout RPE1 cells stained for and depleted of the indicated proteins.

(D, F-I) Immunofluorescence images of centrinone-treated AKAP450/CAMSAP2 knockout RPE1 cells stained for and depleted of the indicated proteins.

(E) Immunofluorescence images of centrinone-treated AKAP450/CAMSAP2/p53 knockout and AKAP450/CAMSAP2/p53/pericentrin knockout RPE1 cells stained as indicated.

In panels A-I, insets show enlargements of the merged channels of the boxed areas, and dashed lines indicate cell edges in panels where these are poorly visible.

(J) Summarizing table of PCM localization and the depletion effects on aMTOC formation in AKAP450/CAMSAP2 knockout RPE1 cells. NT, not tested.

Figure 3. Microtubule organization in acentriolar cells missing different aMTOC components

(A) Immunofluorescence images of centrinone-treated AKAP450/CAMSAP2 knockout RPE1 cells depleted of the indicated proteins and stained for microtubules (α-tubulin, red) and different PCM proteins (green). Insets show enlargements of the merged channels of the boxed areas and dashed lines show cell boundaries.

(B) Quantification of the normalized overall microtubule intensity for the indicated conditions. The number of cells analyzed in three independent experiments: n=56 (siLuci), 45 (siPCNT), 33 (siCDK5RAP2), 36 (siNinein), 43 (siγ-tubulin) and 28 (siDHC). The statistical significance was determined by unpaired two-tailed Mann-Whitney test in Prism 9.1 (***p<0.001). Values represent mean±SD.

(C) Microtubule images were split into a radial and non-radial components (heat maps) based on microtubule orientation in relation to the PCM clusters or the brightest point, as described in Methods.

(D) Quantification of the proportion of the non-radial microtubules shown in panel C (see Methods for details). The number of cells analyzed for each measurement in three independent experiments: n=25 (siLuci), 43 (siPCNT), 32 (siCDK5RAP2), 34 (siNinein), 37 (siγ-tubulin) and 25 (siDHC). The statistical significance was determined by unpaired two-tailed Mann-Whitney test in Prism 9.1 (***p<0.001). Values represent mean±SD.

(E) Diagram illustrating the distribution of PCM clusters and microtubule organization upon the depletion of the indicated proteins in centrinone-treated AKAP450/CAMSAP2 knockout cells.

Figure 4. Microtubule- and dynein-dependent disassembly of aMTOCs

(A) Diagram illustrating different order of cell treatments with centrinone and/or dynapyrazole A (5 μM) and the time points when the cells were fixed.

(B) Immunofluorescence staining of centrinone-treated AKAP450/CAMSAP2 knockout cells treated as shown in panel A. Dashed red circles represent the areas occupied by PCM clusters in each condition.

(C) Quantification of the area occupied by PCM clusters in each condition, as shown in panels A and B. n=35-53 cells analyzed for each measurement in three independent experiments. The statistical significance was determined by unpaired two-tailed Mann-Whitney test in Prism 9.1 (not significant (NS), *P*<0.12; **P*<0.033; ****P*<0.001). Values are represented as mean±SD.

(D) Western blot showing that 3 hr treatment with dynaprazole A does not affect the expression of the endogenous dynein heavy chain and the dynactin large subunit p150Glued.

(E) Time-lapse images of centrinone-treated AKAP450/CAMSAP2 knockout RPE1 cells stably expressing GFP-CDK5RAP2. Microtubules were visualized by treating cells with 100 nM SiR-tubulin overnight. Red arrows show the immobilized PCM clusters at indicated timepoints. Time is min:sec. Time-lapse images of the same cell prior to the nocodazole treatment were shown in Figure 1 - figure supplement 2B.

(F) (Top) Kymograph illustrating the motility of PCM clusters during microtubule disassembly with nocodazole. (Bottom) Measurements of the normalized microtubule (SiR-tubulin) fluorescence intensity (red plot, left Y-axis) and the instantaneous velocity of GFP-CDK5RAP2 clusters (green plot, right Y-axis) during the movement of GFP-CDK5RAP2 clusters away from aMTOC. Microtubule density around each PCM cluster was determined by measuring mean fluorescence intensity of SiR-tubulin in a circular area with a 2 μm radius centered on the PCM cluster and normalizing it to the mean fluorescence intensity of 20 images prior to nocodazole addition (set as 100%). The moment when a

PCM cluster started to move out of the aMTOC was set as the initial time point (0 min) for this cluster, and the subsequent PCM cluster motion velocity and the relative local microtubule density of 43 time points were calculated and averaged. n=12 clusters were analyzed in each condition. Values are represented as mean±SD.

(G) Motor-PAINT images of centrinone-treated AKAP450/CAMSAP2 knockout RPE1 cells before and after nocodazole treatment. Plus-end-out microtubules are shown in white whereas minus-end-out microtubules are shown in magenta. Asterisks represent the putative position of aMTOC.

(H) Summarizing diagram illustrating microtubule organization and the motility of GFP-CDK5RAP2-positive PCM clusters during nocodazole treatment and dynapyrazole A (treat first) and nocodazole co-treatment.

Figure 5. Dynamics of microtubule nucleation and MTOC re-assembly in acentriolar cells

(A) Immunofluorescence images of microtubule regrowth after nocodazole washout at the indicated timepoints in centrinone-treated AKAP450/CAMSAP2 knockout RPE1 cells stained for PCM components (green) and newly nucleated microtubules (EB1, red). A Golgi marker, GM130 (blue), is included in the left row, and zooms of the boxed regions (numbered 1 and 2) show that microtubules nucleate from PCM clusters but not from the Golgi membranes. Dashed lines show cell boundaries.

(B) Immunofluorescence images of microtubule regrowth experiments after depletion of the indicated proteins in centrinone-treated AKAP450/CAMSAP2 knockout RPE1 cells stained for the indicated PCM markers (green) and EB1 as a marker of nascent microtubules (red). Cell outlines are indicated with dashed lines and enlargements of the merged channels of the boxed areas are shown on the right.

(C) Quantification of normalized microtubule intensity at 30 s after nocodazole washout in control cells and cells depleted of the indicated PCM proteins. n=40 (siLuci, siPCNT), 57 (siCDK5RAP2), 48 (siNIN), 45 (siγ-tubulin) and 50 (siDHC) cells analyzed for each measurement in three independent experiments. The statistical significance was determined by unpaired two-tailed Mann-Whitney test in Prism 9.1 (***P*<0.002; ****P*<0.001). Values are represented as mean±SD.

(D) Time-lapse images of centrinone-treated AKAP450/CAMSAP2 knockout RPE1 cells stably expressing GFP-CDK5RAP2 before and after nocodazole washout. Dispersed GFP-CDK5RAP2-positive PCM clusters (GFP, green) serve as microtubule nucleation sites (SiR-tubulin, red) and coalesce into a big cluster after nocodazole washout. Time is min:sec.

(E) Immunofluorescence images of centrinone-treated AKAP450/CAMSAP2 knockout RPE1 cells stained for pericentrin (green) and microtubules (α-tubulin, red) at the indicated timepoints after nocodazole washout.

(F) Measurements of normalized fluorescence intensity of PCM clusters at the indicated distances in relation to the brightest point, as described in Methods. The biggest PCM cluster (which normally also had the highest fluorescence intensity) was selected as the center, around which 10 concentric circles with 2 μm width were drawn. Fluorescence intensity of PCM clusters in these concentric circles was measured automatically and normalized by the sum of the total PCM intensity in each cell per condition. n=12 cells per plot per timepoint. Values represent mean±SD.

(G) Summarizing diagram illustrating microtubule organization and motility of GFP-CDK5RAP2-positive PCM clusters during nocodazole washout.

Figure 6. CAMSAP2-driven microtubule organization in acentriolar cells

(A) Immunofluorescence images of control or centrinone treated AKAP450 knockout RPE1 cells stained for CAMSAP2 (green), PCM protein (γ-tubulin, cyan) and microtubules (α-tubulin, red). Enlargements show the boxed regions of the merged images.

(B) Time lapse images of centrinone treated AKAP450 knockout RPE1 cells stably expressing GFP-CDK5RAP2 (green). Microtubules were labeled with 100 nM SiR-tubulin overnight (red, top row). The maximum intensity projection includes 200 frames, 200 ms/frame. Red arrows show the motion directions of GFP-CDK5RAP2-positive PCM clusters. Time is min:sec.

(C) A diagram of microtubule organization and PCM motility in AKAP450 knockout cells.

(D, E) Diagram of the inducible heterodimerization assay with ppKin14 and CAMSAP2. (D) CAMSAP2 was tagged with mCherry and fused to a tandemly repeated FKBP domain; tetramerized ppKin14 was tagged with TagBFP and fused to FRB. Rapalog induces the binding of CAMSAP2 and ppKin14 by linking FKBP to FRB. (E) Rapalog treatment induces the binding of CAMSAP2 (red) and ppKin14 (blue) and the formation of radial microtubule network. In this scheme, PCM-anchored microtubules are not shown.

(F) Immunofluorescence images of centrinone-treated AKAP450/CAMSAP2 knockout RPE1 cells co-transfected with 2FKBP-mCherry-CAMSAP2 and FRB-TagBFP-GCN4-ppKin14 and stained for the indicated proteins in cells treated with DMSO or rapalog. Zooms show the magnifications of boxed areas.

(G) Quantification of the proportion of cells with a radial, whirlpool-like or non-radial microtubule organization with and without rapalog treatment. Numbers on the histogram show the percentages. 414 cells treated with DMSO (-Rapa) and 385 cells treated with rapalog (+Rapa) analyzed for each measurement in three independent experiments (n=3). Values represent mean±SD.

Figure 7. The role of the PCM in CAMSAP2-driven formation of aMTOCs

(A,B) Immunofluorescence images of centrinone-treated AKAP450/CAMSAP2/p53/pericentrin knockout RPE1 cells transfected with 2FKBP-mCherry-CAMSAP2 and FRB-TagBFP-GCN4-ppKi14 and stained for the indicated components before (top) or after an overnight rapalog treatment. Zooms show magnifications of boxed areas. Black dashed lines show the position of the nucleus.

(C) Cells treated as described for panel A were co-transfected with GFP-pericentrin and stained for mitochondria (cytochrome C, red) and CAMSAP2 (red) in same channel overnight after rapalog addition. Zooms show magnifications of boxed areas.

(D) Quantification of the proportion of cells with different types of microtubule minus end organization before and after overnight rapalog treatment. Numbers on the histogram show the percentages. 334 (-Rapa), 424(+Rapa) cells of AKAP450/CAMSAP2/p53/pericentrin knockout RPE1 cells, 206(-Rapa) and 239(+Rapa) of AKAP450/CAMSAP2/CDK5RAP2/MMG/p53/pericentrin knockout RPE1 cells analyzed for each measurement in three independent experiments (n=3). Values represent mean±SD.

(E) Immunofluorescence images of centrinone-treated AKAP450/CAMSAP2/CDK5RAP2/MMG/p53/pericentrin knockout RPE1 cells transfected with 2FKBP-mCherry-CAMSAP2 and FRB-TagBFP-GCN4-ppKi14 and stained for microtubules (α-tubulin, green) after an overnight rapalog treatment. Zooms show magnifications of boxed areas.

Legends to Supplemental Figures

Figure 1 – figure supplement 1. Characterization of aMTOCs in AKAP450/CAMSAP2 knockout cells

(A) Immunofluorescence images of centrinone B treated AKAP450 knockout RPE1 cells stained for CAMSAP2 (green) and γ-tubulin (red), transfected either with control (Luciferase) or CAMSAP2 siRNAs. Insets show enlargements of the merged images of the boxed areas.

(B) Quantification of CAMSAP2 depletion and aMTOC formation related to panel A. For normalized CAMSAP2 intensity, n=76 (siLuciferase) and 62 (siCAMSAP2) cells from three independent experiment were analyzed; to calculate the percentage of cells showing dispersed or clustered PCM, n=300 (siLuciferase) and 299 (siCAMSAP2) cells analyzed for each measurement in three independent experiments. The statistical significance was determined by unpaired two-tailed Mann-Whitney test in Prism 9.1 (***$p<0.001$). Values represent mean±SD.

(C) Immunofluorescence images of AKAP450/CAMSAP2 knockout treated with DMSO or centrinone B and stained for pericentrin and centrin show the main PCM organization types (centrin-negative cells with cylindrical or round PCM cluster, dispersed PCM or no cluster, and centrin-positive centrosomes) in each condition. Enlargements of the merged channels of the boxed areas are shown on the right.

(D) Quantification of the main PCM organization types in centrinone-treated AKAP450 knockout and AKAP450/CAMSAP2 knockout RPE1 cells. Numbers on the histogram show the percentages. 465 (AKAP450 KO) and 495 (AKAP450/CAMSAP2 KO) cells analyzed for each measurement in three independent experiments (n=3). Values represent mean±SD.

(E) Diagram showing the generation of CPAP or PLK4 depleted AKAP450/CAMSAP2 knockout RPE1 cells with different drug treatments. Cells were transfected with siRNAs to depleted CPAP and PLK4 respectively. After 2 days, the transfection was performed again to increase the depletion efficiency. After 2 more days, cells were treated with thymidine to block cell proliferation or with a combination of thymidine and centrinone B, or thymidine, centrinone B and the PLK1 inhibitor BI 2536 for one or three days. Cells were fixed for the first time (Fix1) after a 24 hr drug treatment, and for the second time (Fix2) after a 72 hr drug treatment.

(F) Quantification of the main PCM organization types, as described for panel D, for cells prepared as described in panel E. Numbers on the histogram show the percentages and numbers in brackets show cells analyzed for each measurement in three independent experiments (n=3; 247-612 cells analyzed per condition). Values represent mean±SD.

(G-I) Immunofluorescence images of Fix2 (as described in panel E) showing control (transfected with siRNA against Luciferase), or depleted of PLK4 or CPAP and treated as indicated. Cells were stained for centrioles (CEP135, centrin), PCM proteins (PCNT) and microtubules (α-tubulin). Images illustrate the PCM organization types in each condition. Insets show enlargements of the merged channels for the boxed areas.

Figure 1 – figure supplement 2. PCM dynamics visualized with GFP-CDK5RAP2

(A) Immunofluorescence images of control and centrinone B treated WT RPE1 cell stably expressing GFP-CDK5RAP2 (green) stained for α-tubulin (red) and pericentrin (PCNT, blue). Zooms show enlargements of the boxed regions.

(B) Time-lapse images of centrinone-treated AKAP450/CAMSAP2 knockout RPE1 cells stably expressing GFP-CDK5RAP2. Microtubules are visualized by treating the cells with 100 nM SiR-tubulin overnight. PCM labeled with GFP-CDK5RAP2 (green) forms a stable cluster that functions as the MTOC. Zooms show the enlarged GFP channel of the boxed regions. Time is min:sec.

Figure 2 – figure supplement 1. Characterization of PCM components localizing to aMTOCs in AKAP450/CAMSAP2 knockout cells

(A) Western blot showing that endogenous NEDD1 and CEP192 are present in centrinone-treated AKAP450/CAMSAP2 knockout cells.

(B) Western blot results showing the depletion of the indicated PCM proteins.

(C) Immunofluorescence images of centrinone-treated AKAP450/CAMSAP2 knockout RPE1 cells showing the localization and the effects of depletion of the indicated proteins on the aMTOCs. siRNA against luciferase was used as a control. Zooms show enlargements of the merged channels of the boxed areas.

Figure 2 – figure supplement 2. Generation of the AKAP450/CAMSAP2/p53/pericentrin knockout RPE1 cell line

(A) Diagram illustrating two sgRNA sites targeting p53 exon 2 and exon 4. The green and red boxes indicate the position of the PAM sites, and the predicted Cas9 cut sites are indicated by scissors.

(B,C) Genotyping results of the genomic mutation using gel-purified PCR product which covers exon 2 and exon 4 of the p53-encoding gene in AKAP450/CAMSAP2/p53 knockout cell line and a diagram illustrating the induced inversion.

(D) Diagram illustrating the binding sites of p53 antibodies and the position of the mutation induced in p53-encoding gene.

(E,F) Immunofluorescence and Western blot images showing p53 expression in control and AKAP450/CAMSAP2/p53 knockout cells.

(G-H) Genotyping results of the genomic mutation using gel-purified PCR product which covers the two sgRNAs targeting sites within pericentrin-encoding gene in AKAP450/CAMSAP2/p53/pericentrin knockout cell line and a diagram illustrating the induced genomic mutations within exon 5 of the pericentrin-encoding gene. The green and red boxes indicate the position of the PAM sites, and the predicted Cas9 cut sites are indicated by scissors.

(I) Diagram illustrating the binding domain of the pericentrin antibody and the positions of the mutations induced downstream of the Cas9 cutting sites.

(J) Immunofluorescence images confirming the loss of pericentrin in AKAP450/CAMSAP2/p53/pericentrin knockout cells.

(K) Western blot confirming the loss of p53 and pericentrin in AKAP450/CAMSAP2/p53/pericentrin knockout cells.

Figure 2 – figure supplement 3. Characterization of PCM organization in AKAP450/CAMSAP2/p53/ pericentrin knockout cells

Immunofluorescence images of centrinone-treated AKAP450/CAMSAP2/p53 knockout (Ctl) and AKAP450/CAMSAP2/p53/pericentrin knockout (PCNT KO) RPE1 cells showing staining for the indicated proteins. Zooms of the boxed areas show merged channels.

Figure 2 – figure supplement 4. Effects of the depletion or knockout of EB1 and EB3 on aMTOC formation in AKAP450/CAMSAP2 knockout cells

(A) Immunofluorescence images of centrinone-treated AKAP450/CAMSAP2 knockout cells stained for EB1 or EB3 and pericentrin showing effects of EB1 or EB3 depletion on aMTOCs.

(B) Western blot confirming the loss of AKAP450 and CAMSAP2 in AKAP450/CAMSAP2/EB1/EB3 mutant cells.

(C) Immunofluorescence images of control or centrinone-treated AKAP450/CASMSAP2/EB1/EB3 mutant RPE1 cells stained for the indicated proteins. Zooms of the boxed areas show merged channels.

Figure 4 – Figure supplement 1. PCM dynamics during nocodazole treatment in centrinone-treated AKAP450/CAMSAP2 knockout cells

(A) Time-lapse images illustrating the dynamics of GFP-CDK5RAP2 clusters (green, white arrows) and microtubules (visualized with an overnight treatment with 100 nM SiR-tubulin, red) during nocodazole treatment. A single frame of the whole cell is on the bottom left, with the boxed area indicating the location of the enlarged images. Time is min:sec.

(B) Motor-PAINT images of centrinone-treated AKAP450/CAMSAP2 knockout RPE1 cells before and after treatment with 10 µM nocodazole for 15 min (the same cells, colorized differently, are displayed in Figure 4G). Microtubule segments were assigned a color based on their absolute orientation, with their plus-ends pointing in the directions indicated with the compass. Asterisks indicate approximate assumed positions of aMTOCs.

Figure 5 – figure supplement 1. PCM dynamics and microtubule regrowth during nocodazole washout in AKAP450/CAMSAP2 knockout cells

(A) Immunofluorescence images of acentriolar AKAP450/CAMSAP2 knockout RPE1 cells fixed at 30 s and 10 min after nocodazole washout and stained for the indicated markers. Zooms show the enlargements of boxed areas. Dashed lines show the cell boundaries.

(B) Summarizing table showing the presence of PCM components in clusters (including centrosome and aMTOC) before and after nocodazole washout in indicated conditions.

(C) Immunofluorescence images of control acentriolar AKAP450/CAMSAP2 knockout RPE1 cells and cells lacking the indicated PCM proteins fixed 2 min after nocodazole washout and stained for EB1 (a marker of growing microtubules, red) and different PCM proteins (γ-tubulin, NIN and DHC, green; CDK5RAP2 and PCNT, blue). Insets show the enlargements of the boxed areas and zooms show the radial and non-radial part of growing microtubules. Dashed lines show the cell boundaries.

(D) Quantification of the proportion of non-radial microtubules 2 min after nocodazole washout. The radial and the non-radial microtubule intensities were measured and the non-radial microtubule intensity was normalized by dividing it by the sum of the radial and the non-radial microtubule intensities for each group. n=20-25 cells analyzed for each measurement in three independent experiments. The statistical significance was determined by unpaired two-tailed Mann-Whitney test in Prism 9.1 (***p<0.001). Values represent mean±SD.

(E) Diagram showing microtubule regrowth and PCM assembly in control acentriolar AKAP450/CAMSAP2 knockout RPE1 cells and cells depleted of the indicated PCM proteins at 30 s and 2 min after nocodazole washout.

Figure 5 – figure supplement 2. Pericentrin is required for PCM clustering in acentriolar AKAP450/CAMSAP2 knockout RPE1 cells

Time-lapse images of centrinone-treated AKAP450/CAMSAP2 knockout RPE1 cells stably expressing GFP-CDK5RAP2 (green), which is diffusely distributed and does not form any clear clusters. Microtubule regrowth experiments show random nucleation of microtubules (labeled with 100nM SiR-tubulin overnight) that remain disorganized. Summarizing diagram shows PCM clusters and microtubule network in the indicated conditions.

Figure 6 – figure supplement 1. PCM dynamics and the effects of CAMSAP2 clustering on PCM organization in centrinone-treated RPE1 cells lacking AKAP450

(A) Time-lapse images illustrating the dynamics of PCM clusters (green, white arrows) and microtubules (SiR-tubulin, red) after nocodazole washout in centrinone-treated AKAP450 knockout RPE1 cells stably expressing GFP-CDK5RAP2. A single frame of the whole cell with numbered boxed areas indicating the location of enlarged time-lapse images is shown on the left. White arrows indicate moving PCM clusters after microtubules re-grow. Time is min:sec.

(B) Time-lapse images of centrinone-treated AKAP450 knockout RPE1 cells stably expressing GFP-CDK5RAP2. GFP-CDK5RAP2 forms small clusters that are dynamic before microtubules (SiR-tubulin, red) are disassembled by nocodazole treatment. Red arrows show that these clusters become immobile when microtubules are completely depolymerized (enlargements of the boxed areas shown in the bottom rows). GFP-CDK5RAP2-positive clusters are sites of microtubule nucleation after

nocodazole washout and become dynamic again once microtubules re-grow. The maximum intensity projections include 100 or 400 frames, 200 ms/frame. Time is min:sec.

(C) Summarizing diagram illustrating microtubule organization and the motility of PCM clusters in acentriolar AKAP450 knockout RPE1 cells.

(D) Movement trajectories of PCM clusters in acentriolar AKAP450 knockout cells before and after 1 hr treatment with 5µM dynapyrazole A. 350 frames with a 2 s interval from the same cell were analyzed. Shaded areas represent the cell body.

(E) Quantification of the length of the trajectories of moving PCM clusters. n=132 (without dynapyrazole A, from 5 cells) and 111 (after 1 hr dynapyrazole A treatment, from 4 cells) trajectories were analyzed for each condition. The statistical significance was determined by unpaired two-tailed Mann-Whitney test in Prism 9.1 (***p<0.001). Values represent mean±SD.

(F) Immunofluorescence images of centrinone-treated AKAP450/CAMSAP2 knockout RPE1 cells transfected with 2FKBP-mCherry-CAMSAP2 and FRB-TagBFP-GCN4-ppKin14 and stained for the indicated proteins after overnight rapalog treatment. Zooms show the magnification of boxed area.

Figure 6 – figure supplement 2. Pericentrin is required for PCM clustering in acentriolar AKAP450 knockout RPE1 cells

Time-lapse images of centrinone-treated AKAP450 knockout RPE1 cells stably expressing GFP-CDK5RAP2 (green) depleted of pericentrin. GFP-CDK5RAP2 is diffusely distributed and does not form any clear clusters. Microtubule regrowth experiments show random nucleation of microtubules (labeled with 100nM SiR-tubulin overnight) that remain disorganized. Summarizing diagram shows PCM clusters and microtubule network in the indicated conditions.

Figure 7 – figure supplement 1. Inducible CAMSAP2-driven radial microtubule rearrangement in AKAP450/CAMSAP2/p53/pericentrin knockout cell

(A) Time-lapse images of a centrinone-treated AKAP450/CAMSAP2/p53/pericentrin knockout cell transiently expressing 2FKBP-mCherry-CAMSAP2 and FRB-GFP-GCN4-ppKin14 imaged for 10 min (100 frames, 6 s interval) prior to treatment with 100 nM rapalog and ~90 min after. Time is hr: min: sec.

(B) Immunofluorescence images of centrinone-treated AKAP450/CAMSAP2/p53/pericentrin knockout and AKAP450/CAMSAP2/MMG/CDK5RAP2/p53/pericentrin knockout RPE1 cells, stained for the

indicated markers. In the upper row, the cells were neither transfected nor treated with rapalog, whereas in the other panels, cells were transfected with 2FKBP-mCherry-CAMSAP2 and FRB-HA-GCN4-ppKin14 and treated with rapalog overnight. Zooms show the magnification of boxed areas.

Figure 7 – figure supplement 2. Generation of the AKAP450/CAMSAP2/CDK5RAP2/MMG/ p53/pericentrin knockout RPE1 cell line

(A) Diagram illustrating two sgRNA sites targeting p53 exon 4. The green and red boxes indicate the position of the PAM sites, and the predicted Cas9 cut sites are indicated by scissors. Genotyping results of the genomic mutation using gel-purified PCR product which covers exon 4 of the p53-encoding gene in AKAP450/CAMSAP2/MMG/CDK5RAP2/p53 knockout cell line are shown below.

(B) Diagram illustrating the binding sites of p53 antibodies and the position of the mutation induced in p53-encoding gene.

(C) Immunofluorescence images showing p53 staining in control and AKAP450/CAMSAP2/MMG/CDK5RAP2/p53 knockout cells.

(D) Diagram illustrating two sgRNA sites targeting pericentrin exon 5. The green and red boxes indicate the position of the PAM sites, and the predicted Cas9 cut sites are indicated by scissors. Genotyping results of the genomic mutation using gel-purified PCR product which covers exon 5 of the pericentrin-encoding gene in AKAP450/CAMSAP2/MMG/CDK5RAP2/p53/pericentrin knockout cell line are shown below.

(E) Diagram illustrating the binding domain of the pericentrin antibody and the positions of the mutations induced downstream of the Cas9 cut sites.

(F) Immunofluorescence images showing the confirmation of pericentrin loss in control and AKAP450/CAMSAP2/MMG/CDK5RAP2/p53/pericentrin knockout cells.

(G) Western blot illustrating the p53 and pericentrin loss in control and AKAP450/CAMSAP2/MMG/CDK5RAP2/p53/pericentrin knockout cells.

(H) Immunofluorescence images of control and centrinone-treated AKAP450/CAMSAP2/ CDK5RAP2/MMG/p53/pericentrin knockout cells staining microtubule (α-tubulin, red) and centrosome (CEP192, green). Zooms show magnification of the boxed area.

Legends to Supplemental Videos

Video 1. aMTOC disassembly during nocodazole treatment of acentriolar AKAP450/CAMSAP2 knockout cells

PCM dynamics visualized by stable expression of GFP-CDK5RAP2 (green) in centrinone-treated AKAP450/CAMSAP2 knockout RPE1 cells. Microtubules were labeled overnight with 100 nM SiR-tubulin (red). The cell was imaged for ~3.5min (100 frames, 2 s interval) prior to the addition of 10 µM nocodazole. Time is min: sec.

Video 2. Depletion of pericentrin inhibits PCM clustering in acentriolar AKAP450/CAMSAP2 knockout cells

A pericentrin-depleted acentriolar AKAP450/CAMSAP2 knockout cell stably expressing GFP-CDK5RAP2 (green) and labeled overnight with 100 nM SiR-tubulin (red) was imaged for ~4.5 min (140 frames, 2 s time interval) prior to treatment with 10 µM nocodazole. Nocodazole was washed out at ~20 min (frame 591), when all microtubules were depolymerized. Time is hr: min: sec.

Video 3. PCM dynamics during nocodazole treatment and washout in acentriolar AKAP450 knockout cells

An acentriolar AKAP450 knockout RPE1 cell stably expressing GFP-CDK5RAP2 (green) and labeled overnight with 100 nM SiR-tubulin (red) was imaged for ~7min (200 frames, 2 s interval) prior to treatment with 10 µM nocodazole. Nocodazole was washed out at ~27 min (frame 801) when all microtubules were depolymerized. Time is min: sec.

Video 4. PCM dynamics in acentriolar AKAP450 knockout cells are inhibited by dynapyrazole

An acentriolar AKAP450 knockout RPE1 cell stably expressing GFP-CDK5RAP2 (green) and labeled overnight with 100 nM SiR-tubulin (red) was imaged for ~12 min (350 frames, 2 s interval) prior to the dynapyrazole treatment, treated with 5 µM Dynapyrazole A for 1h, and then the same cell was imaged for ~12 min. Time is min: sec.

Video 5. Depletion of pericentrin inhibits PCM clustering in acentriolar AKAP450 knockout cells

A pericentrin-depleted acentriolar AKAP450 knockout cell stably expressing GFP-CDK5RAP2 (green) and labeled overnight with 100 nM SiR-tubulin (red) was imaged for ~3 min (90 frames, 2 s time interval) prior to treatment with 10 µM nocodazole. Nocodazole was washed out at ~23 min (frame 701) when all microtubules were depolymerized. Time is hr: min: sec.

Video 6. Inducible CAMSAP2-driven radial microtubule rearrangement in an AKAP450/CAMSAP2/p53/pericentrin knockout cell

An acentriolar AKAP450/CAMSAP2/p53/pericentrin knockout cell transiently expressing 2FKBP-mCherry-CAMSAP2 (red) and FRB-GFP-GCN4-ppKin14 (green) was imaged for 10 min (100 frames, 6 s interval) prior to treatment with 100 nM rapalog. Subsequently, the cell was imaged for ~1 hr and 35 min after rapalog addition. Time is hr: min: sec.

Source data 1

Uncropped Western blots shown in this manuscript

(A,B) Western blots showing that NEDD1 and CEP192 are present in centrinone-treated AKAP450/CAMSAP2 knockout cells shown in Figure 2 – figure supplement 1A.

(C-J) Western blots showing the depletion of indicated proteins in centrinone-treated AKAP450/CAMSAP2 knockout cells shown in Figure 2 – figure supplement 1B.

(K) Western blot showing that 3 hr treatment with dynaprazole A does not affect the expression of the endogenous dynein heavy chain and the dynactin large subunit p150Glued in centrinone-treated AKAP450/CAMSAP2 knockout cells shown in Figure 4D.

Source data 2

Uncropped Western blots shown in this manuscript

(A) Western blots showing the knockout of p53 from AKAP450/CAMSAP2 knockout cell line shown in Figure 2 – figure supplement 2F.

(B) Western blots showing the knockout of pericentrin from AKAP450/CAMSAP2/p53 knockout cell line shown in Figure 2 – figure supplement 2K.

(C) Western blots showing the knockout of AKAP450 and CAMSAP2 from EB1/EB3 mutant RPE1 cell line shown in Figure 2 – figure supplement 4B.

(D) Western blots showing the knockout of pericentrin in AKAP450/CAMSAP2/CDK5RAP2/MMG/p53/ knockout cell line shown in Figure 7 – figure supplement 2G.

1566 ***Key reagent or resource table***

Reagent type (species) or resource	Designation	Source or reference	Identifiers	Additional information
Antibody	anti-Pericentrin (mouse monoclonal)	Abcam	Abcam Cat# ab28144, RRID:AB_2160664	(1:500) for IF
Antibody	anti-Pericentrin (rabbit polyclonal)	Abcam	Abcam Cat# ab4448, RRID:AB_304461	(1:500) for IF; (1:1000) for WB
Antibody	anti-CDK5RAP2 (rabbit polyclonal)	Bethyl Laboratories	Bethyl Cat# A300-554A, RRID:AB_477974	(1:300) for IF; (1:1000) for WB
Antibody	anti-γ-tubulin (mouse monoclonal)	Sigma-Aldrich	Sigma-Aldrich: T6557; RRID:AB_477584	(1:300) for IF; (1:2000) for WB
Antibody	anti-γ-tubulin (rabbit polyclonal)	Sigma-Aldrich	Sigma-Aldrich:T3559, RRID:AB_477575	(1:300) for IF
Antibody	anti-NEDD1 (mouse monoclonal)	Abnova	Abnova Corporation Cat# H00121441-M05, RRID:AB_534956	(1:300) for IF
Antibody	anti-NEDD1 (rabbit polyclonal)	Rockland	Rockland Cat# 109-401-C38S, RRID:AB_10893219	(1:1000) for WB
Antibody	anti-Ninein (rabbit polyclonal)	BETHYL	Bethyl Cat# A301-504A, RRID:AB_999627	(1:300) for IF; (1:2000) for WB
Antibody	anti-Ninein (mouse monoclonal)	Santa Cruz Biotechnology	Santa Cruz Biotechnology Cat# sc-376420, RRID:AB_11151570	(1:300) for IF
Antibody	anti-Dynein HC (rabbit polyclonal)	Santa Cruz Biotechnology	Santa Cruz Biotechnology Cat# sc-9115, RRID:AB_2093483	(1:300) for IF; (1:500) for WB
Antibody	anti-p150Glued (mouse monoclonal)	BD Biosciences	BD Biosciences Cat# 610473, RRID:AB_397845	(1:100) for IF; (1:500) for WB
Antibody	anti-PCM1 (mouse monoclonal)	Santa Cruz Biotechnology	Santa Cruz Biotechnology Cat# sc-398365, RRID:AB_2827155	(1:300) for IF
Antibody	anti-PCM1 (rabbit polyclonal)	Bethyl Laboratories	Bethyl Cat# A301-150A, RRID:AB_873100	(1:300) for IF
Antibody	anti-AKAP450 (mouse monoclonal)	BD Biosciences	BD Biosciences Cat# 611518, RRID:AB_398978	(1:500) for WB
Antibody	anti-CAMSAP2 (rabbit polyclonal)	Novus	Novus:NBP1-21402; RRID:AB_1659977	(1:200) for IF; (1:1000) for WB
Antibody	anti-p53 (mouse monoclonal)	Santa Cruz Biotechnology	Santa Cruz Biotechnology Cat# sc-126, RRID:AB_628082	(1:300) for IF; (1:1000) for WB
Antibody	anti-p53 (rabbit polyclonal)	BETHYL	Bethyl Cat# A300-248A, RRID:AB_263349	(1:300) for IF
Antibody	anti-EB1 (mouse monoclonal)	BD Biosciences	BD Biosciences:610535; RRID:AB_397892	(1:400) for IF

Antibody	anti-EB3 (rabbit polyclonal)	Martin, et al., 2018;		(1:300) for IF
Antibody	anti-Centrin (mouse monoclonal)	Millipore	Millipore Cat# 04-1624, RRID:AB_10563501	(1:500) for IF
Antibody	anti-CEP120 (rabbit polyclonal)	Thermo Fisher Scientific	Thermo Fisher Scientific Cat# PA5-55985, RRID:AB_2639665	(1:300) for IF
Antibody	anti-CEP135 (rabbit polyclonal)	Sigma-Aldrich	Sigma-Aldrich:SAB4503685; RRID:AB_10746232	(1:300) for IF
Antibody	anti-CEP152 (rabbit polyclonal)	Abcam	Abcam, Cat # ab183911	(1:300) for IF; (1:1000) for WB
Antibody	anti-CEP170 (mouse monoclonal)	Thermo Fisher Scientific	Thermo Fisher Scientific Cat# 41-3200, RRID:AB_2533502	(1:200) for IF
Antibody	anti-CEP192 (rabbit polyclonal)	Bethyl Laboratories	Bethyl Cat# A302-324A, RRID:AB_1850234	(1:300) for IF; (1:1000) for WB
Antibody	anti-GM130 (mouse monoclonal)	BD Biosciences	BD Biosciences:610823; RRID:AB_398142	(1:300) for IF; (1:2000) for WB
Antibody	anti-α-tubulin YL1/2 (rat monoclonal)	Pierce	Pierce: MA1-80017; RRID:AB_2210201	(1:300) for IF
Antibody	anti-α-tubulin (mouse monoclonal)	Sigma-Aldrich	Sigma-Aldrich:T5168; RRID:AB_477579	(1:400) for IF
Antibody	anti-α-tubulin (rabbit monoclonal antibody)	Abcam	Abcam Cat# ab52866, RRID:AB_869989	(1:800) for IF
Antibody	Anti-β-tubulin (mouse monoclonal)	Sigma-Aldrich	Sigma-Aldrich Cat# T8660, RRID:AB_477590	(1:2000) for WB
Antibody	anti-CLASP1 (rabbit polyclonal)	(Akhmanova et al., 2001)		(1:400) for IF
Antibody	anti-CLASP2 (rabbit polyclonal)	(Akhmanova et al., 2001)		(1:400) for IF
Antibody	anti-CLIP-115 #2238 (rabbit polyclonal)	(Akhmanova et al., 2001)		(1:300) for IF
Antibody	anti-CLIP-170 #2360 (rabbit polyclonal)	(Akhmanova et al., 2001)		(1:300) for IF
Antibody	anti-ch-TOG (rabbit polyclonal)	(Charrasse et al., 1998)	Dr. Lynne Cassimeris (Lehigh University, USA)	(1:200) for IF
Antibody	anti-CPAP (rabbit polyclonal)	(Kohlmaier et al., 2009)	Dr. Pierre Gönczy (EPFL, Switzerland)	(1:200) for IF
Antibody	anti-CP110 (rabbit monoclonal)	Proteintech	Proteintech Cat# 12780-1-AP, RRID:AB_10638480	(1:300) for IF
Antibody	anti-KIF1C (rabbit polyclonal)	Cytoskeleton	Cytoskeleton Cat# AKIN11-A, RRID:AB_10708792	(1:300) for IF
Antibody	anti-KIF2A (rabbit polyclonal)	(Ganem and Compton, 2004)	Dr. Duane Compton (Geisel School of Medicine at Dartmouth, USA)	(1:300) for IF

Antibody	anti-HAUS2 (rabbit polyclonal)	(Lawo et al., 2009)	Dr. Laurence Pelletier (Lunenfeld-Tanenbaum Research Institute, Canada)	(1:200) for IF
Antibody	anti-BICD2 (rabbit polyclonal)	(Hoogenraad et al., 2003)		(1:2500) for WB
Antibody	anti-Actin (mouse monoclonal)	Millipore	Millipore Cat# MAB1501, RRID:AB_2223041	(1:4000) for WB
Antibody	anti-Ku80 (mouse monoclonal)	BD Biosciences	BD Biosciences Cat# 611360, RRID:AB_398882	(1:2000) for WB
Antibody	anti-LaminA/C (mouse monoclonal)	BD Biosciences	BD Biosciences Cat# 612162, RRID:AB_399533	(1:400) for IF
Antibody	anti-Cytochrome C (mouse monoclonal)	BD Biosciences	BD Biosciences Cat# 556432, RRID:AB_396416	(1:300) for IF
Antibody	anti-Calnexin (rabbit polyclonal)	Abcam	Abcam Cat# ab22595, RRID:AB_2069006	(1:300) for IF
Antibody	Anti-Lamtor4 (rabbit monoclonal)	Cell Signaling (CST)/Bioke	Cell Signaling Technology Cat# 12284, RRID:AB_2797870	(1:800) for IF
	Anti-Tom20 (mouse monoclonal)	BD Biosciences	BD Biosciences Cat# 612278, RRID:AB_399595	(1:200) for IF
Antibody	IRDye 800CW/680LT secondaries	Li-Cor Biosciences	LI-COR Biosciences Cat# 926-32219, RRID:AB_1850025' LI-COR Biosciences Cat# 926-68020, RRID:AB_10706161; LI-COR Biosciences Cat# 926-32211, RRID:AB_621843; LI-COR Biosciences Cat# 926-68021, RRID:AB_10706309	(1:5000) for WB
Antibody	Alexa Fluor 405–, 488–, and 594–secondaries	Molecular Probes/ Thermo Fisher Scientific	Molecular Probes Cat# A-11007, RRID:AB_141374; Cat# A-11034, RRID:AB_2576217; Cat# A32723, RRID:AB_2633275; Cat# A-31553, RRID:AB_221604; Cat# A-11029, RRID:AB_138404; Cat# A-11032, RRID:AB_2534091; Cat# A-11006, RRID:AB_141373; Thermo Fisher Scientific Cat# A-11012, RRID:AB_2534079	(1:500) for IF
Sequence-based reagent	siRNA against PCNT #1	(Gavilan et al., 2018)	5'-AAAAGCUCUGAUUUAUCAAAAGAAG-3'	
Sequence-based reagent	siRNA against PCNT #2	(Gavilan et al., 2018)	5'-UGAUUGGACGUCAUCCAAUGAGAAA-3'	

Sequence-based reagent	siRNA against PCNT #3	(Tibelius et al., 2009)	5'-GCAGCUGAGCUGAAGGAGA-3'	
Sequence-based reagent	siRNA against CDK5RAP2	(Fong et al., 2008)	5'-UGGAAGAUCUCCUAACUAA-3'	
Sequence-based reagent	siRNA against γ-tubulin #1	(Luders et al., 2006)	5'-GGAGGACAUGUUCAAGGAA-3'	
Sequence-based reagent	siRNA against γ-tubulin #2	(Vinopal et al., 2012)	5'-CGCAUCUCUUUCUCAUAU-3'	
Sequence-based reagent	siRNA against Ninein	(Goldspink et al., 2017)	5'-CGGUACAAUGAGUGUAGAAUU-3'	
Sequence-based reagent	siRNA against PCM1	(Wang et al., 2013)	5'-UCAGCUUCGUGAUUCUCAG-3'	
Sequence-based reagent	siRNA against CEP152	(Cizmecioglu et al., 2010; Komarova et al., 2005)	5'-GCGGAUCCAACUGGAAAUCUA-3'	
Sequence-based reagent	siRNA against CEP120	(Ganem et al., 2005; Lin et al., 2013)	5'-AAUAUAUCUUCUUGCAUCUCCUUCC-3'	
Sequence-based reagent	siRNA against CEP192	(Sonnen et al., 2013)	5'-CAGAGGAAUCAAUAAUAAA -3'	
Sequence-based reagent	siRNA against NEDD1 #1	(Luders et al., 2006)	5'-GCAGACAUGUGUCAAUUUA-3'	
Sequence-based reagent	siRNA against NEDD1 #2	(Haren et al., 2006)	5'-GGGCAAAAGCAGACAUGUG-3'	
Sequence-based reagent	siRNA against DHC #1	(Splinter et al., 2010)	5'-CGUACUCCCGUGAUUGAUG-3'	
Sequence-based reagent	siRNA against DHC #2	(Splinter et al., 2010)	5'-GCCAAAAGUUACAGACUUU-3'	
Sequence-based reagent	siRNA against CAMSAP2	(Jiang et al., 2014)	5'-GUACUGGAUAAAUAAGGUA-3'	
Sequence-based reagent	siRNA against CEP170	(Stolz et al., 2015)	5'-GAAGGAAUCCUCCAAGUCA-3'	
Sequence-based reagent	siRNA against CPAP	(Tang et al., 2009)	5'-AGAAUUAGCUCGAAUAGAA-3'	
Sequence-based reagent	siRNA against CLIP170 #1	(Lansbergen et al., 2004; Mimori-Kiyosue et al., 2005)	5'-GGAGAAGCAGCAGCACAUU-3'	
Sequence-based reagent	siRNA against CLIP170 #2	(Lansbergen et al., 2004; Mimori-Kiyosue et al., 2005)	5'-UGAAGAUGUCAGGAGAUAA-3'	

Sequence-based reagent	siRNA against CLIP115 #1	(Lansbergen et al., 2004)	5'-GGCACAGCAUGAGCAGUAU-3'	
Sequence-based reagent	siRNA against CLIP115 #2	(Lansbergen et al., 2004)	5'-CUGGAAAUCCAAGCUGGAC-3'	
Sequence-based reagent	siRNA against ch-TOG:	(Cassimeris and Morabito, 2004; Lansbergen et al., 2004)	5'-GAGCCCAGAGUGGUCCAAA-3'	
Sequence-based reagent	siRNA against EB1	(Grigoriev et al., 2008; Lansbergen et al., 2004)	5'-AUUCCAAGCUAAGCUAGAA-3'	
Sequence-based reagent	siRNA against EB3	(Cassimeris and Morabito, 2004; Komarova et al., 2005)	5'-CUAUGAUGGAAAGGAUUAC-3'	
Sequence-based reagent	siRNA against KIF2A	(Ganem et al., 2005; Grigoriev et al., 2008)	5'-GGCAAAGAGAUUGACCUGG-3'	
Sequence-based reagent	siRNA against CP110	(Cizmecioglu et al., 2010; Spektor et al., 2007)	5'-AAGCAGCAUGAGUAUGCCAGU-3'	
Sequence-based reagent	siRNA against Luciferase	(Lansbergen et al., 2004; Lin et al., 2013)	5'-CGUACGCGGAAUACUUCGA-3'	
Sequence-based reagent	sgRNA target CAMSAP2	(Lansbergen et al., 2004; Wu et al., 2016)	5'-gCATGATCGATACCCTCATGA-3	
Sequence-based reagent	sgRNA target p53 e2 #1	This study	5′-gCGTCGAGCCCCCTCTGAGTC-3′;	
Sequence-based reagent	sgRNA target p53 e4 #2	This study	5′-gCCATTGTTCAATATCGTCCG-3′;	
Sequence-based reagent	sgRNA target p53 e4 #3	This study	5′-gTCCATTGCTTGGGACGGCAA-3′;	
Sequence-based reagent	sgRNA target PCNT e5-1 #1	This study	5′-gAGACGGCATTGACGGAGCTG-3′;	
Sequence-based reagent	sgRNA target PCNT e5-2 #2	This study	5′-GCTCAACAGCCGGCGTGCCC-3′;	

Sequence-based reagent	p53 KO sequencing primer F	This study	5′-TCAGACACTGGCATGGTGTT-3′;	
Sequence-based reagent	p53 KO sequencing primer R	This study	5′-AGAAATGCAGGGGGATACGG-3′;	
Sequence-based reagent	PCNT KO sequencing primer F	This study	5′-ATACAGCGAGGGAATTCGGG-3′;	
Sequence-based reagent	PCNT KO sequencing primer R	This study	5′-TAGAATGCCCACACCGAGC-3′;	
Chemical compound	Centrinone B	Tocris Bioscience	Tocris Bioscience Cat # 5690	125nM
Chemical compound	Nocodazole	Sigma-Aldrich	Sigma-Aldrich, Cat # M1404-10MG	10μM
Chemical compound	Rapalog (A/C Heterodimerizer)	Takara	Takara, Cat # 635056	50nM (fixation), 100nM (live imaging).
Chemical compound	Dynapyrazole A	Sigma-Aldrich	Sigma-Aldrich, Cat # SML2127-25MG	5μM
Chemical compound	BI2536	Selleckchem	Selleckchem, Cat # S1109	500nM
Chemical compound	SiR-tubulin	Tebu-bio	Tebu-bio, Cat # SC002	100nM
Software, algorithm	ImageJ radiality plugin	https://github.com/ekatrukha/radialitymap	Katrukha, 2017. radialitymap. Github. https://github.com/ekatrukha/radialitymap cf1e78f	
Recombinant DNA reagent	pLVX-IRES-puro (plasmid)	Clontech		
Recombinant DNA reagent	pB80-FRB-TagBFP-GCN4-ppKin14 (plasmid)	This work		
Recombinant DNA reagent	pB80-FRB-GFP-GCN4-ppKin14 (plasmid)	This work		
Recombinant DNA reagent	pB80-FRB-HA-GCN4-ppKin14 (plasmid)	This work		
Recombinant DNA reagent	2FKBP-mCherry-CAMSAP2 (plasmid)	This work		

Recombinant DNA reagent	GFP-PCNT (plasmid)	This work		
Recombinant DNA reagent	GST-DmKHC(1-421)-mNeonGreen (plasmid)	This work		
Cell line (Homo sapiens)	hTERT-RPE-1	ATCC	CRL-4000	
Cell line (Homo sapiens)	hTERT-RPE-1 AKAP450 knockout	(Wu et al., 2016)		
Cell line (Homo sapiens)	hTERT-RPE-1 AKAP450/CAMSAP 2 knockout	(Wu et al., 2016)		
Cell line (Homo sapiens)	hTERT-RPE-1 AKAP450/CAMSAP 2/p53 knockout	This work		
Cell line (Homo sapiens)	hTERT-RPE-1 AKAP450/CAMSAP 2/p53/Pericentrin knockout	This work		
Cell line (Homo sapiens)	hTERT-RPE-1 AKAP450/CAMSAP 2/EB1/EB3 mutant	This work		
Cell line (Homo sapiens)	hTERT-RPE-1 AKAP450/CAMSAP 2/CDK5RAP2/MMG/ p53/Pericentrin knockout	This work		
Cell line (Homo sapiens)	HEK 293T	ATCC	CRL-11268	

1567

Figure 1

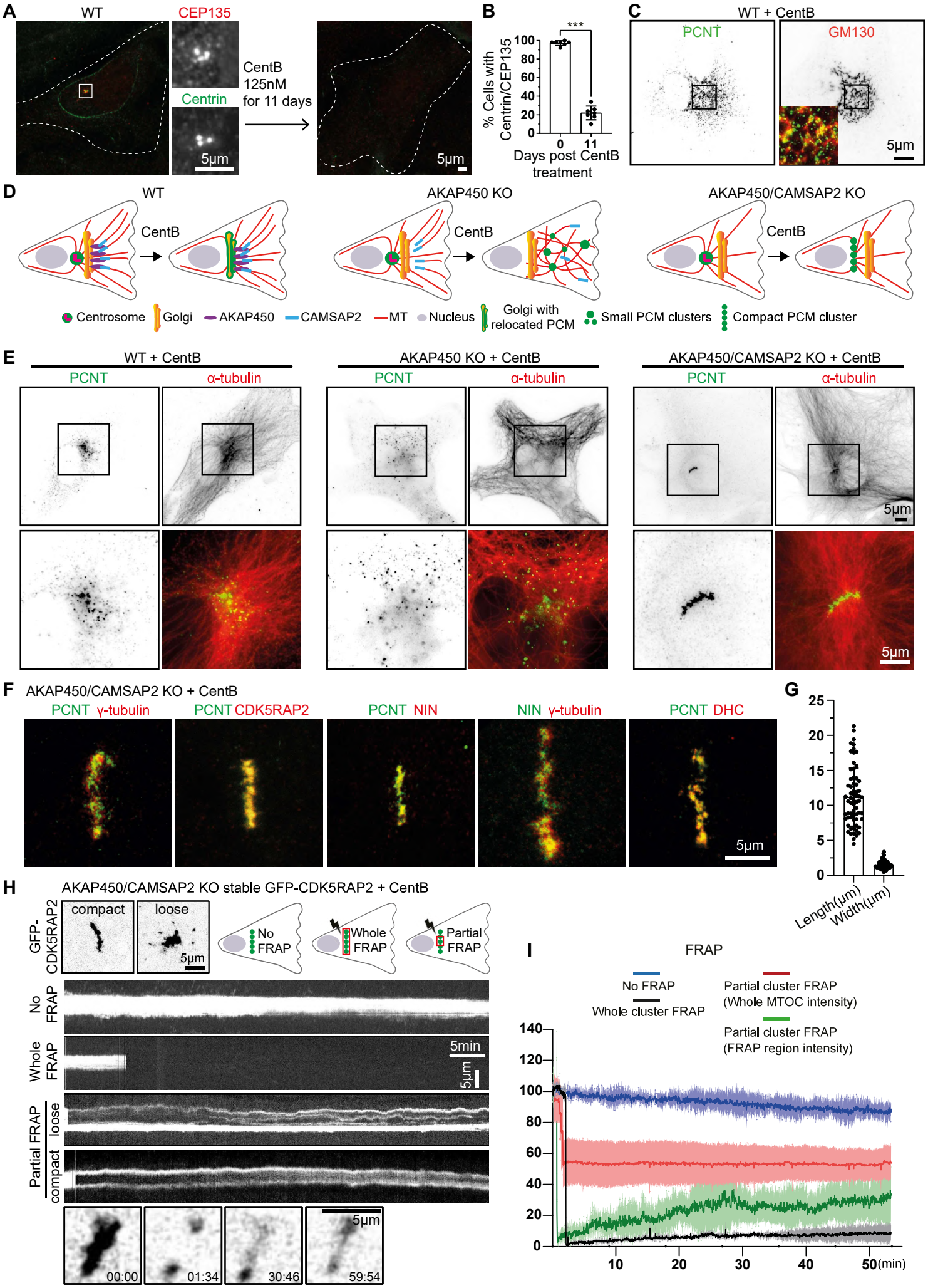
A
WT
CEP135
Centrin
5μm
CentB
125nM
for 11 days
5μm
B
% Cells with Centrin/CEP135
***
Days post CentB treatment
C
WT + CentB
PCNT
GM130
5μm
D
WT
AKAP450 KO
AKAP450/CAMSAP2 KO
CentB
Centrosome
Golgi
AKAP450
CAMSAP2
MT
Nucleus
Golgi with relocated PCM
Small PCM clusters
Compact PCM cluster
E
WT + CentB
AKAP450 KO + CentB
AKAP450/CAMSAP2 KO + CentB
PCNT
α-tubulin
5μm
F
AKAP450/CAMSAP2 KO + CentB
PCNT γ-tubulin
PCNT CDK5RAP2
PCNT NIN
NIN γ-tubulin
PCNT DHC
5μm
G
Length(μm)
Width(μm)
H
AKAP450/CAMSAP2 KO stable GFP-CDK5RAP2 + CentB
GFP-CDK5RAP2
compact
loose
5μm
No FRAP
Whole FRAP
Partial FRAP
5min
5μm
Partial FRAP
loose
compact
00:00
01:34
30:46
59:54
I
FRAP
No FRAP
Whole cluster FRAP
Partial cluster FRAP (Whole MTOC intensity)
Partial cluster FRAP (FRAP region intensity)
(min)

Figure 2

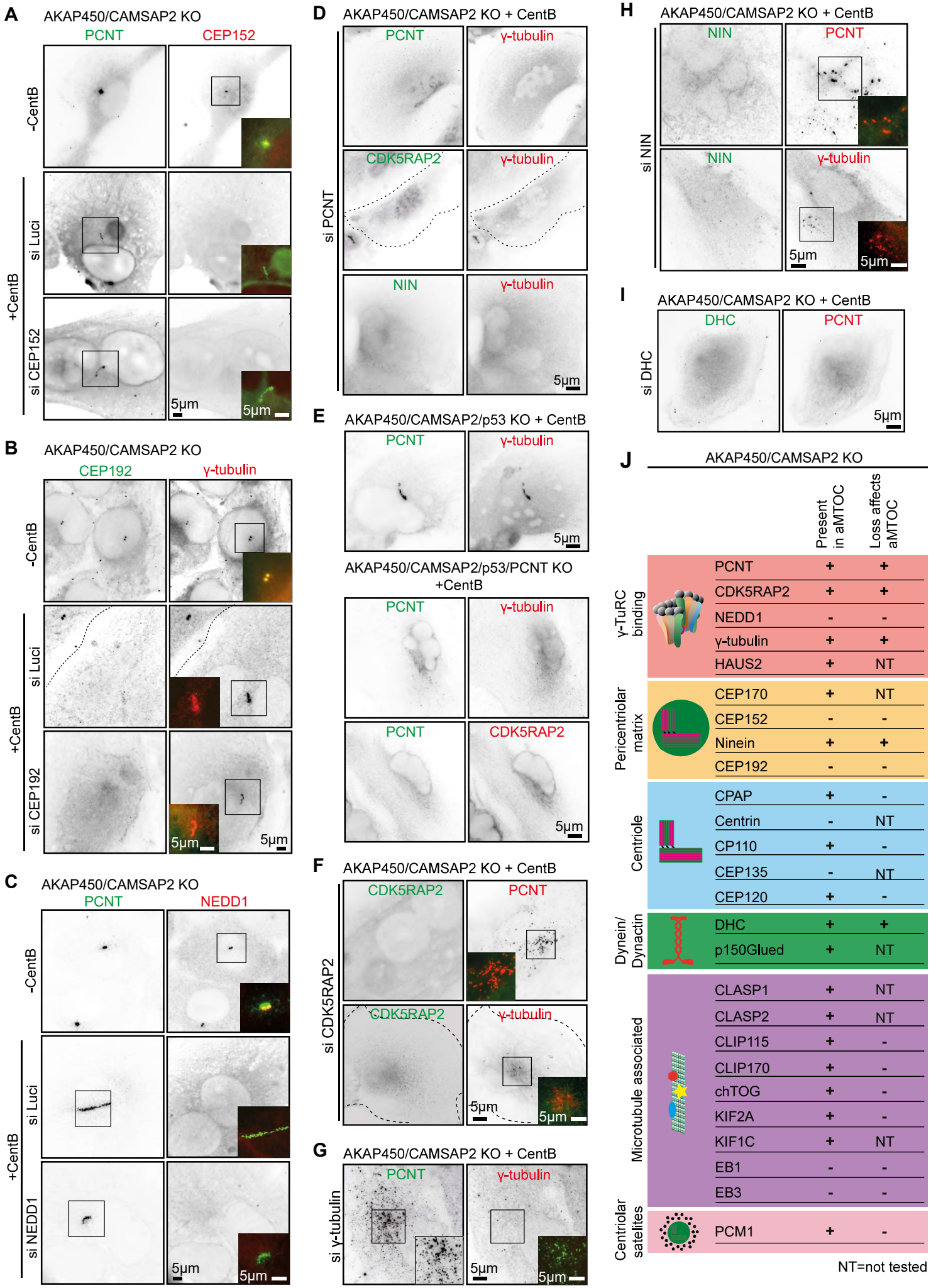
A
AKAP450/CAMSAP2 KO
PCNT
CEP152
-CentB
+CentB
si Luci
si CEP152
5μm
B
AKAP450/CAMSAP2 KO
CEP192
γ-tubulin
si CEP192
C
AKAP450/CAMSAP2 KO
NEDD1
si NEDD1
D
AKAP450/CAMSAP2 KO + CentB
si PCNT
CDK5RAP2
NIN
E
AKAP450/CAMSAP2/p53 KO + CentB
AKAP450/CAMSAP2/p53/PCNT KO +CentB
F
AKAP450/CAMSAP2 KO + CentB
si CDK5RAP2
G
AKAP450/CAMSAP2 KO + CentB
si γ-tubulin
H
AKAP450/CAMSAP2 KO + CentB
si NIN
I
AKAP450/CAMSAP2 KO + CentB
si DHC
DHC
J
AKAP450/CAMSAP2 KO
Present in aMTOC
Loss affects aMTOC
γ-TuRC binding
PCNT + +
CDK5RAP2 + +
NEDD1 - -
γ-tubulin + +
HAUS2 + NT
Pericentriolar matrix
CEP170 + NT
CEP152 - -
Ninein + +
CEP192 - -
Centriole
CPAP + -
Centrin - NT
CP110 + -
CEP135 - NT
CEP120 + -
Dynein/ Dynactin
DHC + +
p150Glued + NT
Microtubule associated
CLASP1 + NT
CLASP2 + NT
CLIP115 + -
CLIP170 + -
chTOG + -
KIF2A + -
KIF1C + NT
EB1 - -
EB3 - -
Centriolar satellites
PCM1 + -
NT=not tested

Figure 3

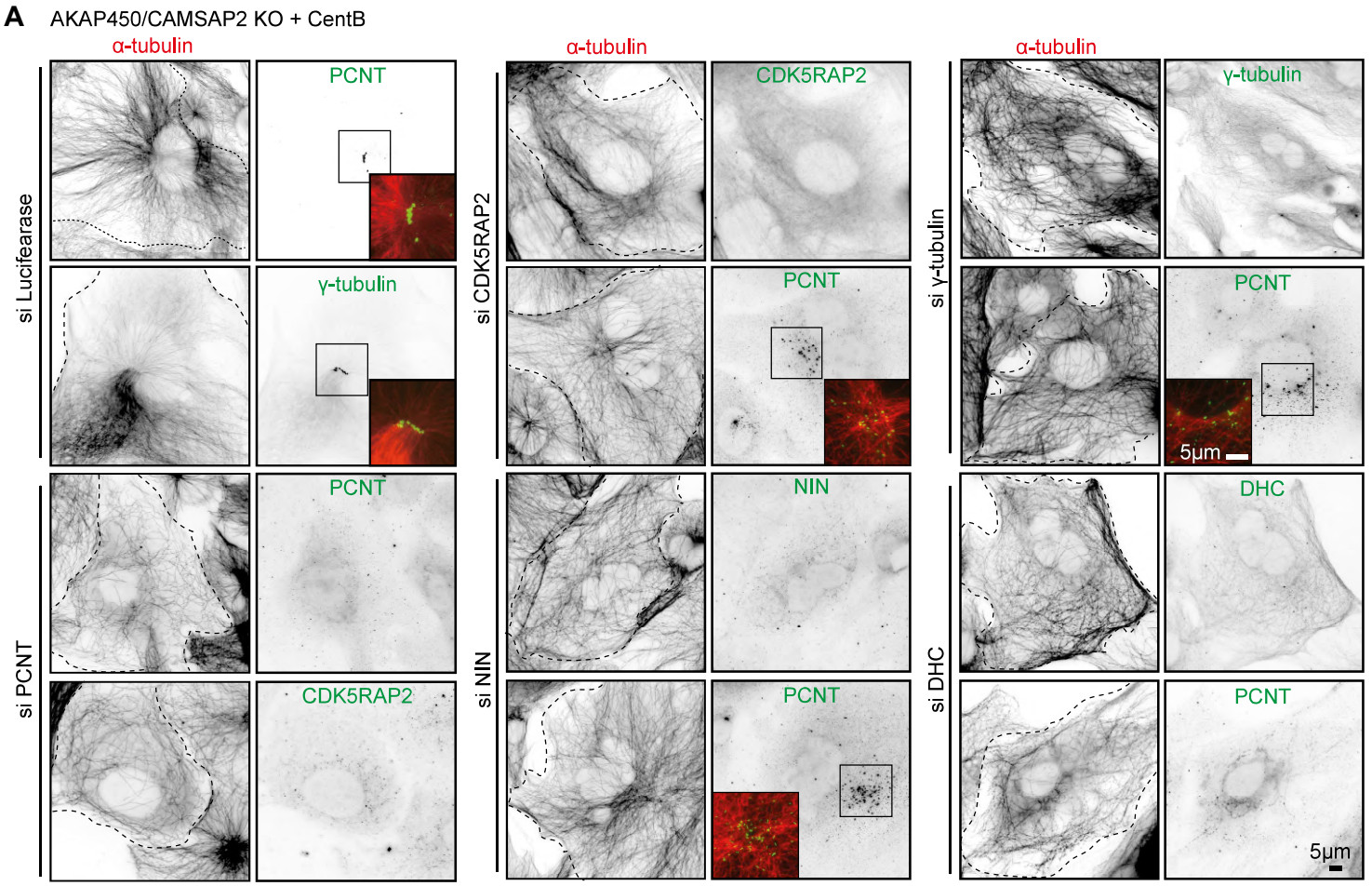
A
AKAP450/CAMSAP2 KO + CentB
α-tubulin
PCNT
γ-tubulin
CDK5RAP2
NIN
DHC
si Lucifearase
si CDK5RAP2
si γ-tubulin
si PCNT
si NIN
si DHC
5μm

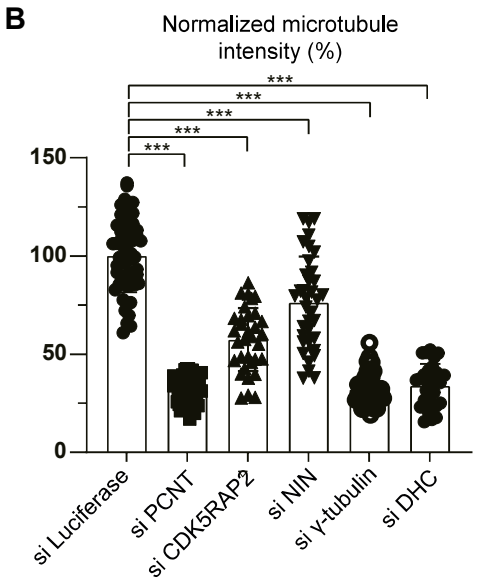
B
Normalized microtubule intensity (%)
150
100
50
0
si Luciferase
si PCNT
si CDK5RAP2
si NIN
si γ-tubulin
si DHC

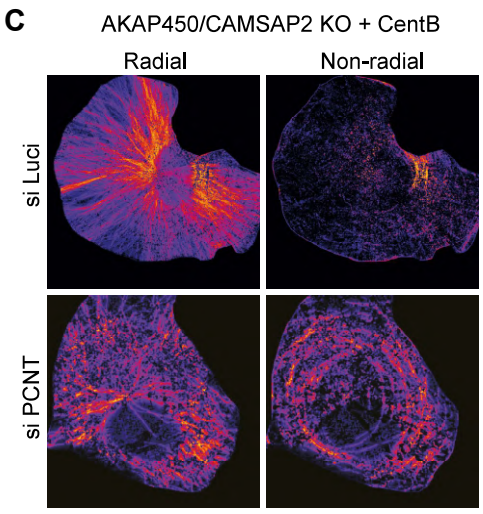
C
AKAP450/CAMSAP2 KO + CentB
Radial
Non-radial
si Luci
si PCNT

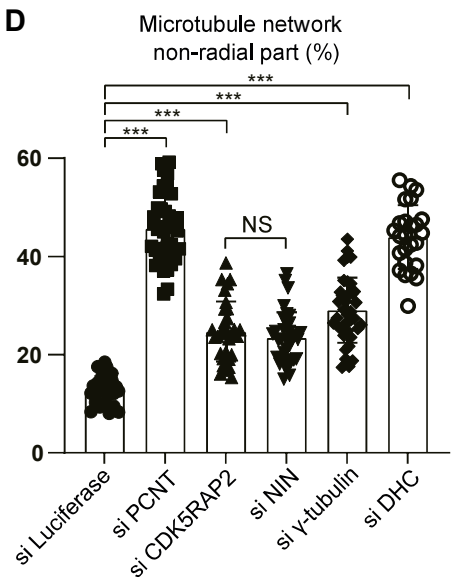
D
Microtubule network non-radial part (%)
60
40
20
0
NS
si Luciferase
si PCNT
si CDK5RAP2
si NIN
si γ-tubulin
si DHC

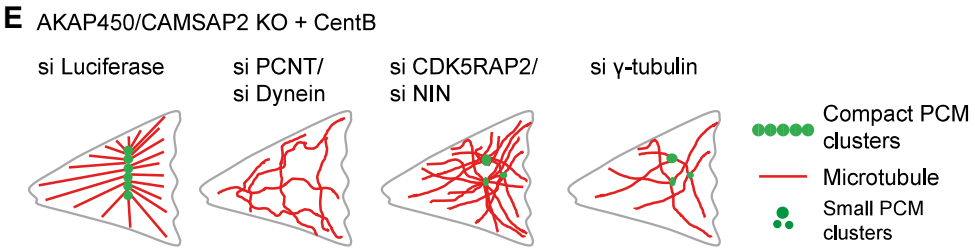
E
AKAP450/CAMSAP2 KO + CentB
si Luciferase
si PCNT/
si Dynein
si CDK5RAP2/
si NIN
si γ-tubulin
Compact PCM clusters
Microtubule
Small PCM clusters

Figure 4

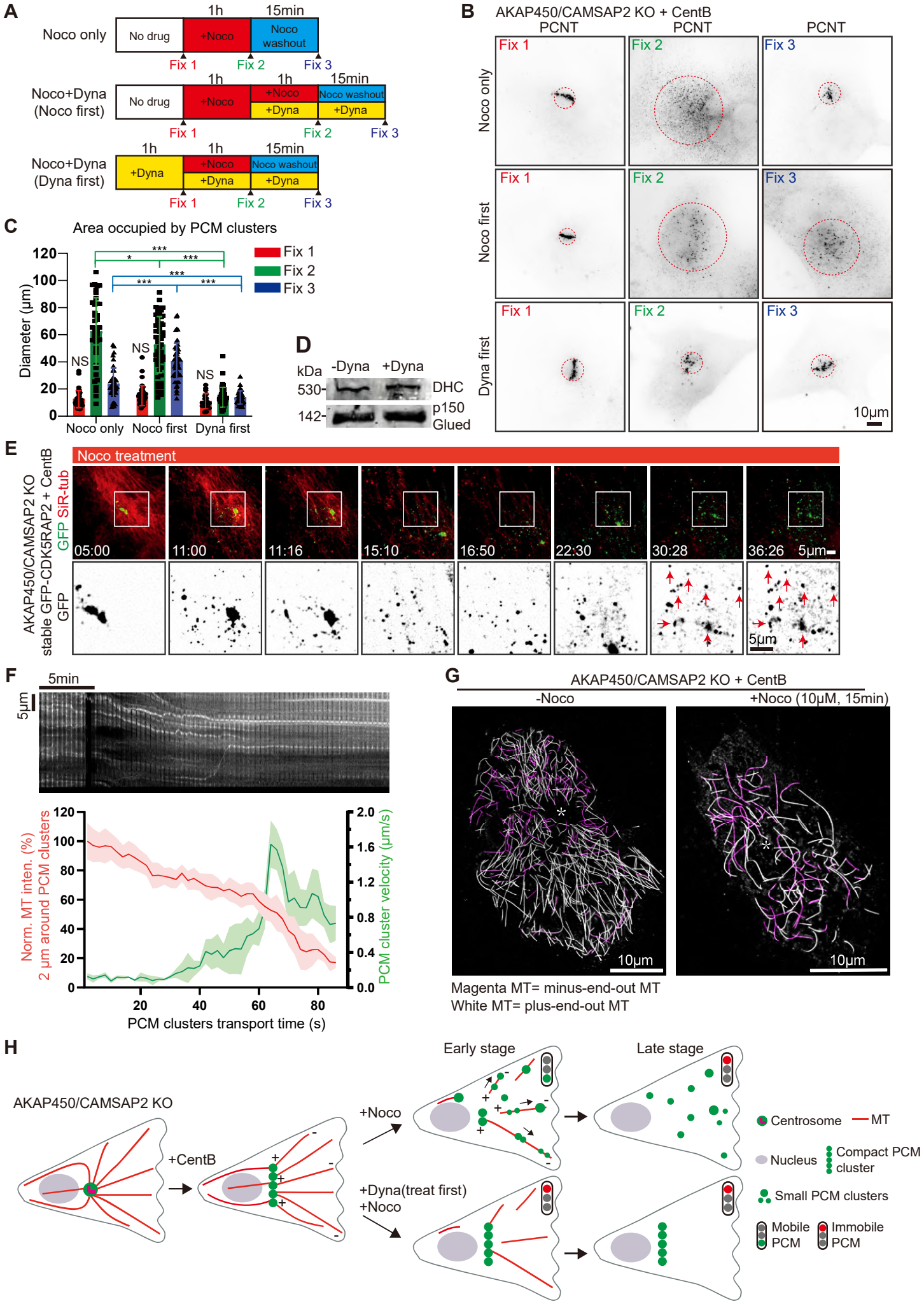
A
Noco only
No drug
1h
+Noco
15min
Noco washout
Fix 1
Fix 2
Fix 3
Noco+Dyna (Noco first)
+Dyna
Noco+Dyna (Dyna first)
B
AKAP450/CAMSAP2 KO + CentB
PCNT
Noco only
Noco first
Dyna first
10μm
C
Area occupied by PCM clusters
Diameter (μm)
NS
Noco only
Noco first
Dyna first
D
kDa
-Dyna
+Dyna
530-
142-
DHC
p150 Glued
E
Noco treatment
AKAP450/CAMSAP2 KO stable GFP-CDK5RAP2 + CentB
GFP SiR-tub
GFP
05:00
11:00
11:16
15:10
16:50
22:30
30:28
36:26
5μm
F
5min
5μm
Norm. MT inten. (%) 2 μm around PCM clusters
PCM cluster velocity (μm/s)
PCM clusters transport time (s)
G
AKAP450/CAMSAP2 KO + CentB
-Noco
+Noco (10μM, 15min)
10μm
Magenta MT= minus-end-out MT
White MT= plus-end-out MT
H
AKAP450/CAMSAP2 KO
+CentB
+Noco
+Dyna(treat first)
+Noco
Early stage
Late stage
Centrosome
MT
Nucleus
Compact PCM cluster
Small PCM clusters
Mobile PCM
Immobile PCM

Figure 5

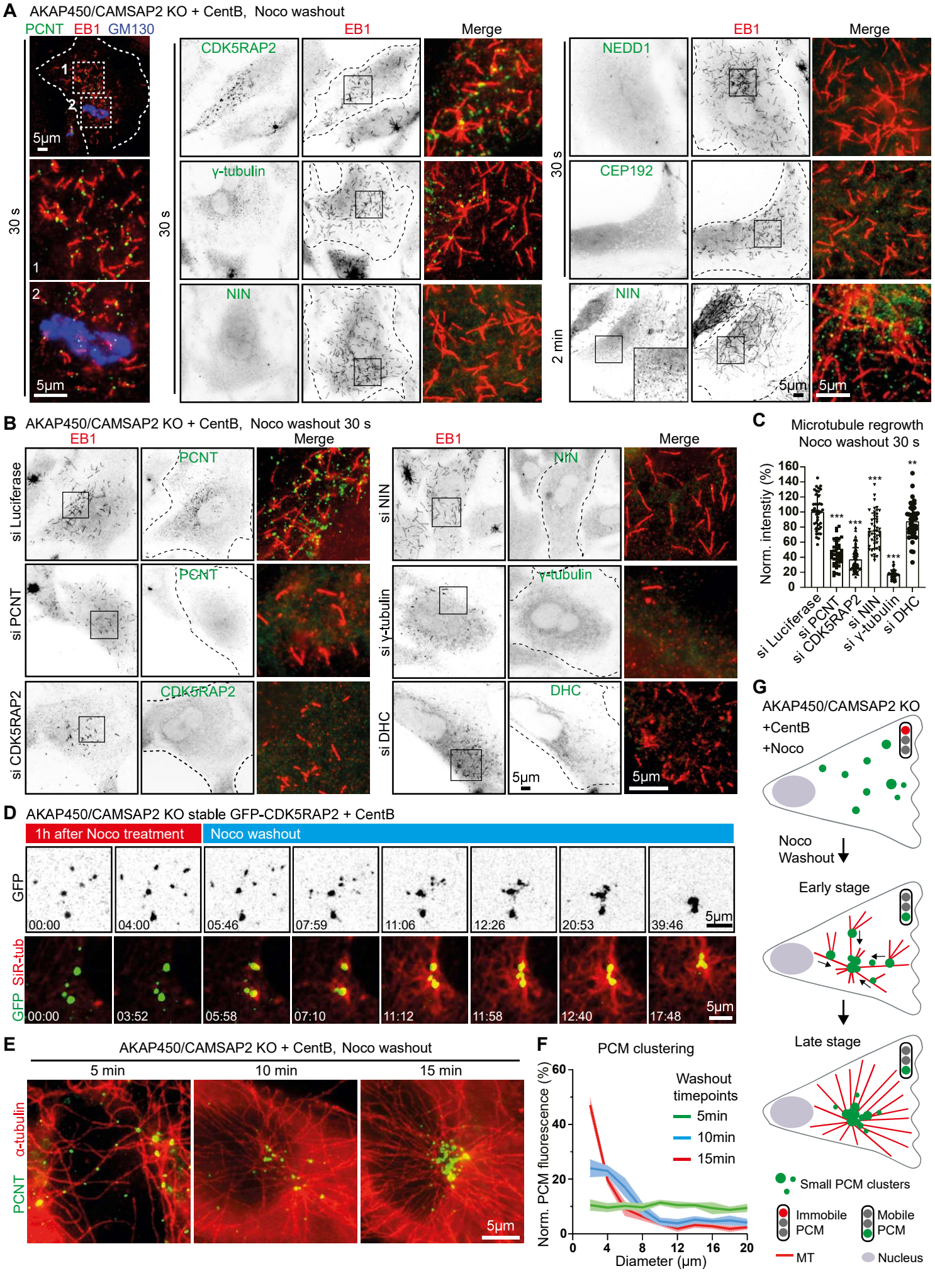
A
AKAP450/CAMSAP2 KO + CentB, Noco washout
PCNT EB1 GM130
EB1
Merge
CDK5RAP2
γ-tubulin
NIN
NEDD1
CEP192
30 s
2 min
5μm
B
AKAP450/CAMSAP2 KO + CentB, Noco washout 30 s
si Luciferase
si PCNT
si CDK5RAP2
si NIN
si γ-tubulin
si DHC
PCNT
CDK5RAP2
DHC
C
Microtubule regrowth
Noco washout 30 s
Norm. intenstiy (%)
si Luciferase
si PCNT
si CDK5RAP2
si NIN
si γ-tubulin
si DHC
D
AKAP450/CAMSAP2 KO stable GFP-CDK5RAP2 + CentB
1h after Noco treatment
Noco washout
GFP
SiR-tub
E
AKAP450/CAMSAP2 KO + CentB, Noco washout
5 min
10 min
15 min
α-tubulin
PCNT
F
PCM clustering
Norm. PCM fluorescence (%)
Diameter (μm)
Washout timepoints
5min
10min
15min
G
AKAP450/CAMSAP2 KO
+CentB
+Noco
Noco Washout
Early stage
Late stage
Small PCM clusters
Immobile PCM
Mobile PCM
MT
Nucleus

Figure 6

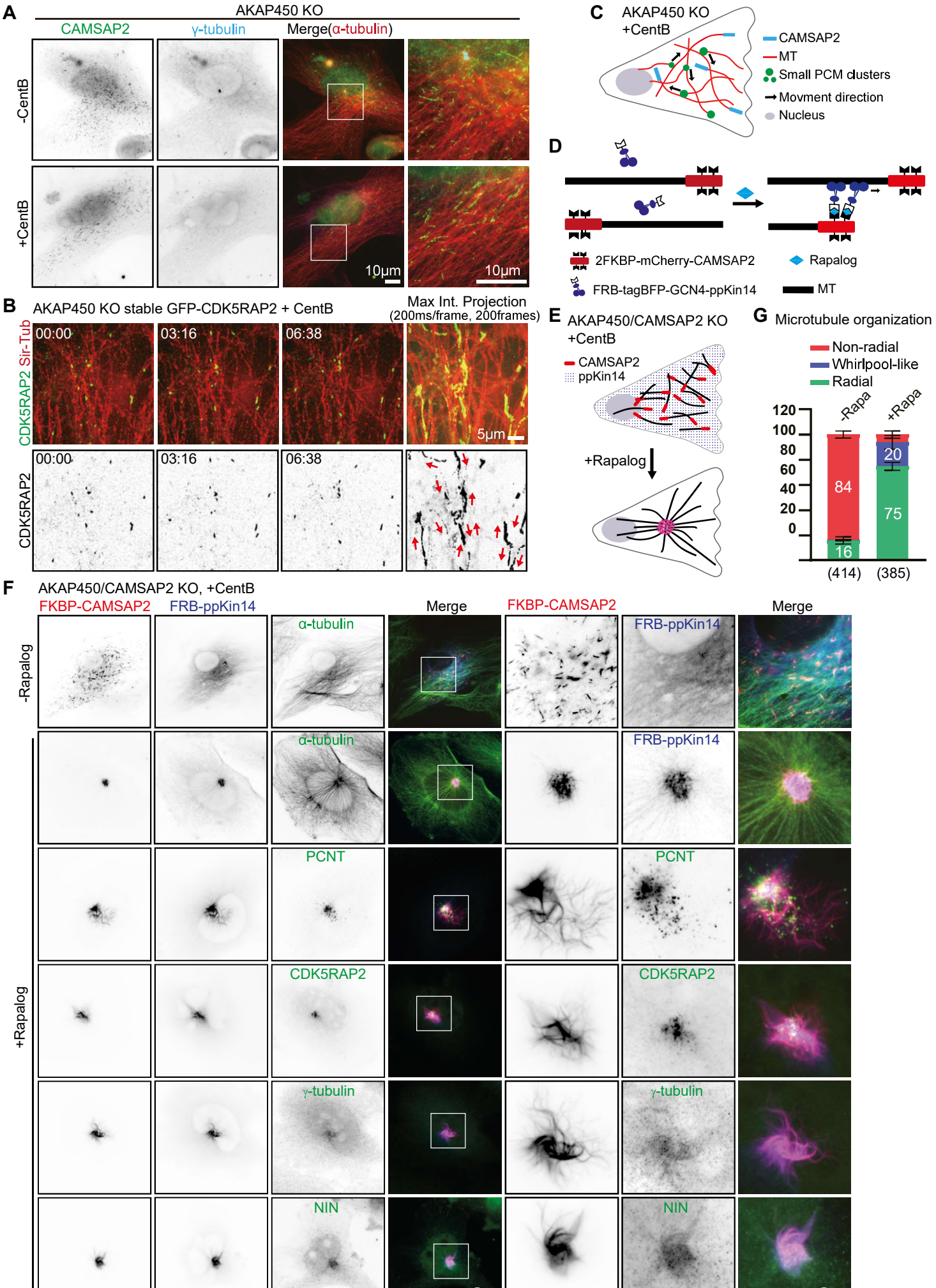
A
AKAP450 KO
CAMSAP2
γ-tubulin
Merge(α-tubulin)
-CentB
+CentB
10μm
10μm
B
AKAP450 KO stable GFP-CDK5RAP2 + CentB
Max Int. Projection
(200ms/frame, 200frames)
CDK5RAP2 Sir-Tub
CDK5RAP2
00:00
03:16
06:38
5μm
C
AKAP450 KO
+CentB
CAMSAP2
MT
Small PCM clusters
Movment direction
Nucleus
D
2FKBP-mCherry-CAMSAP2
Rapalog
FRB-tagBFP-GCN4-ppKin14
MT
E
AKAP450/CAMSAP2 KO
+CentB
CAMSAP2
ppKin14
+Rapalog
G
Microtubule organization
Non-radial
Whirlpool-like
Radial
-Rapa
+Rapa
120
100
80
60
40
20
0
84
16
20
75
(414)
(385)
F
AKAP450/CAMSAP2 KO, +CentB
FKBP-CAMSAP2
FRB-ppKin14
Merge
α-tubulin
PCNT
CDK5RAP2
γ-tubulin
NIN
-Rapalog
+Rapalog
5μm
5μm

Figure 7

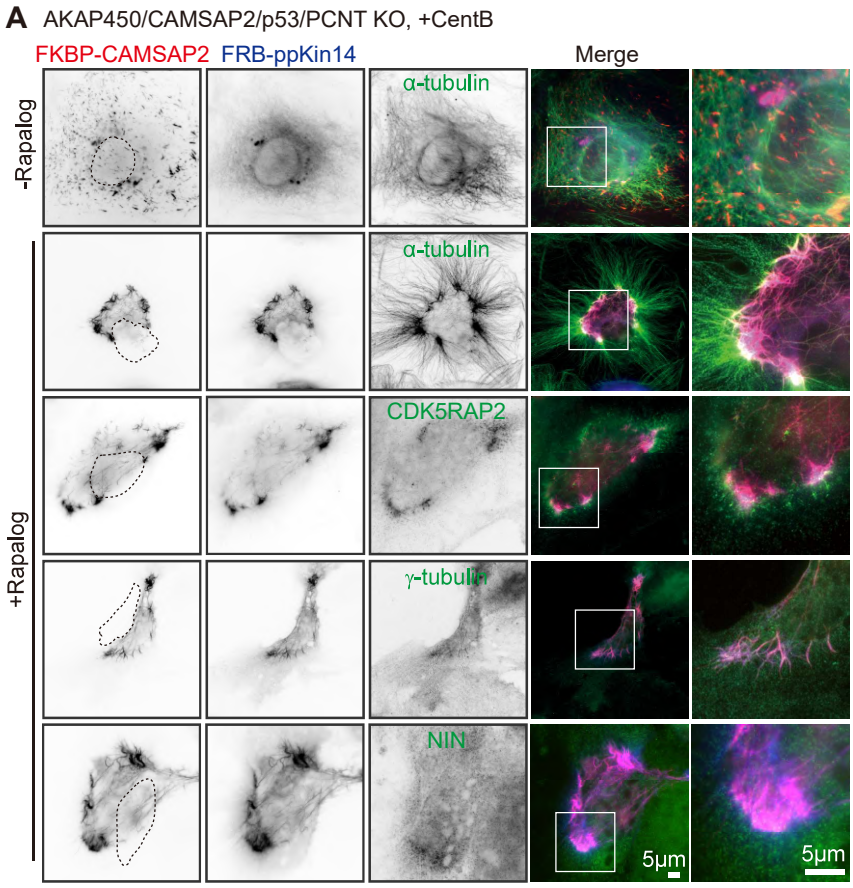
A
AKAP450/CAMSAP2/p53/PCNT KO, +CentB
FKBP-CAMSAP2
FRB-ppKin14
Merge
-Rapalog
+Rapalog
α-tubulin
α-tubulin
CDK5RAP2
γ-tubulin
NIN
5μm
5μm

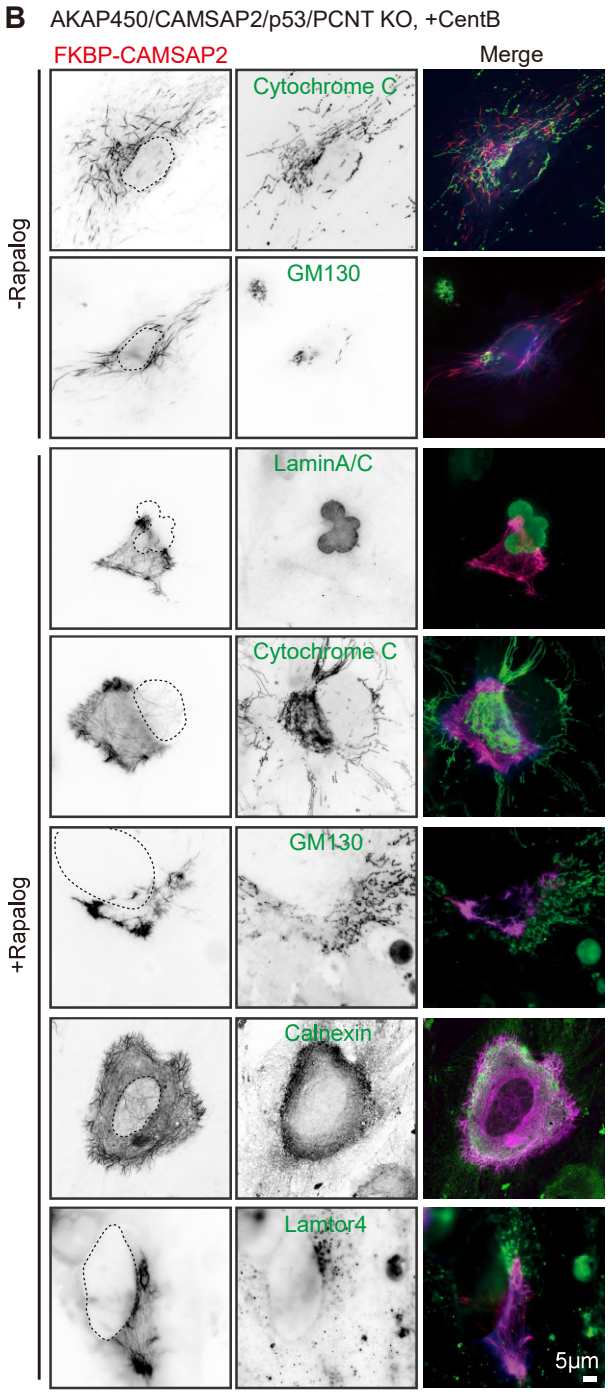
B
AKAP450/CAMSAP2/p53/PCNT KO, +CentB
FKBP-CAMSAP2
Merge
-Rapalog
+Rapalog
Cytochrome C
GM130
LaminA/C
Cytochrome C
GM130
Calnexin
Lamtor4
5μm

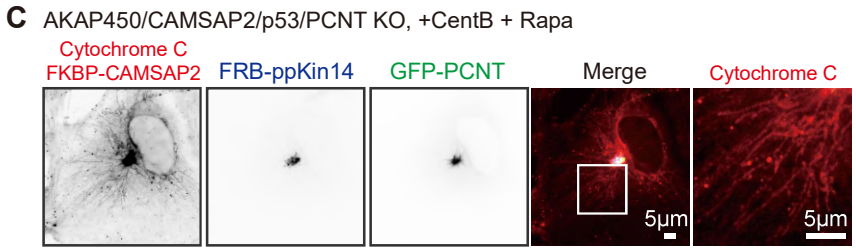
C
AKAP450/CAMSAP2/p53/PCNT KO, +CentB + Rapa
Cytochrome C
FKBP-CAMSAP2
FRB-ppKin14
GFP-PCNT
Merge
Cytochrome C
5μm
5μm

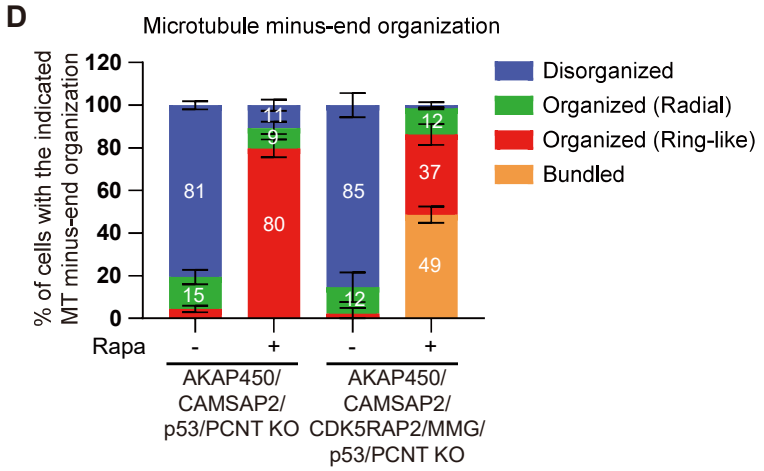
D
Microtubule minus-end organization
% of cells with the indicated MT minus-end organization
120
100
80
60
40
20
0
81
15
11
9
80
85
12
12
37
49
Rapa
-
+
-
+
AKAP450/ CAMSAP2/ p53/PCNT KO
AKAP450/ CAMSAP2/ CDK5RAP2/MMG/ p53/PCNT KO
Disorganized
Organized (Radial)
Organized (Ring-like)
Bundled

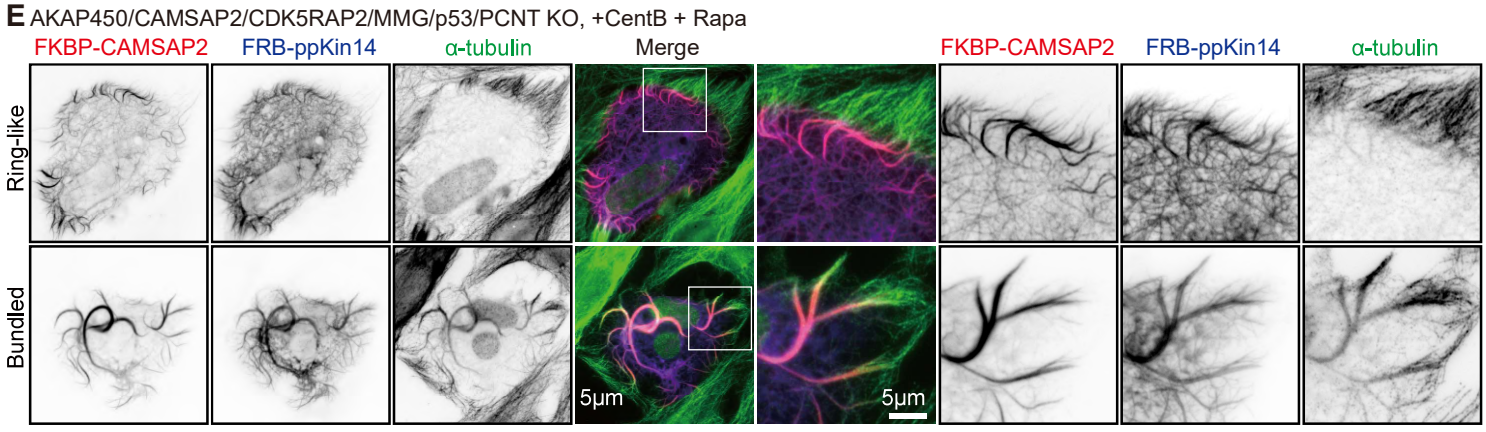
E
AKAP450/CAMSAP2/CDK5RAP2/MMG/p53/PCNT KO, +CentB + Rapa
FKBP-CAMSAP2
FRB-ppKin14
α-tubulin
Merge
FKBP-CAMSAP2
FRB-ppKin14
α-tubulin
Ring-like
Bundled
5μm
5μm

Figure 1 - figure supplement 1

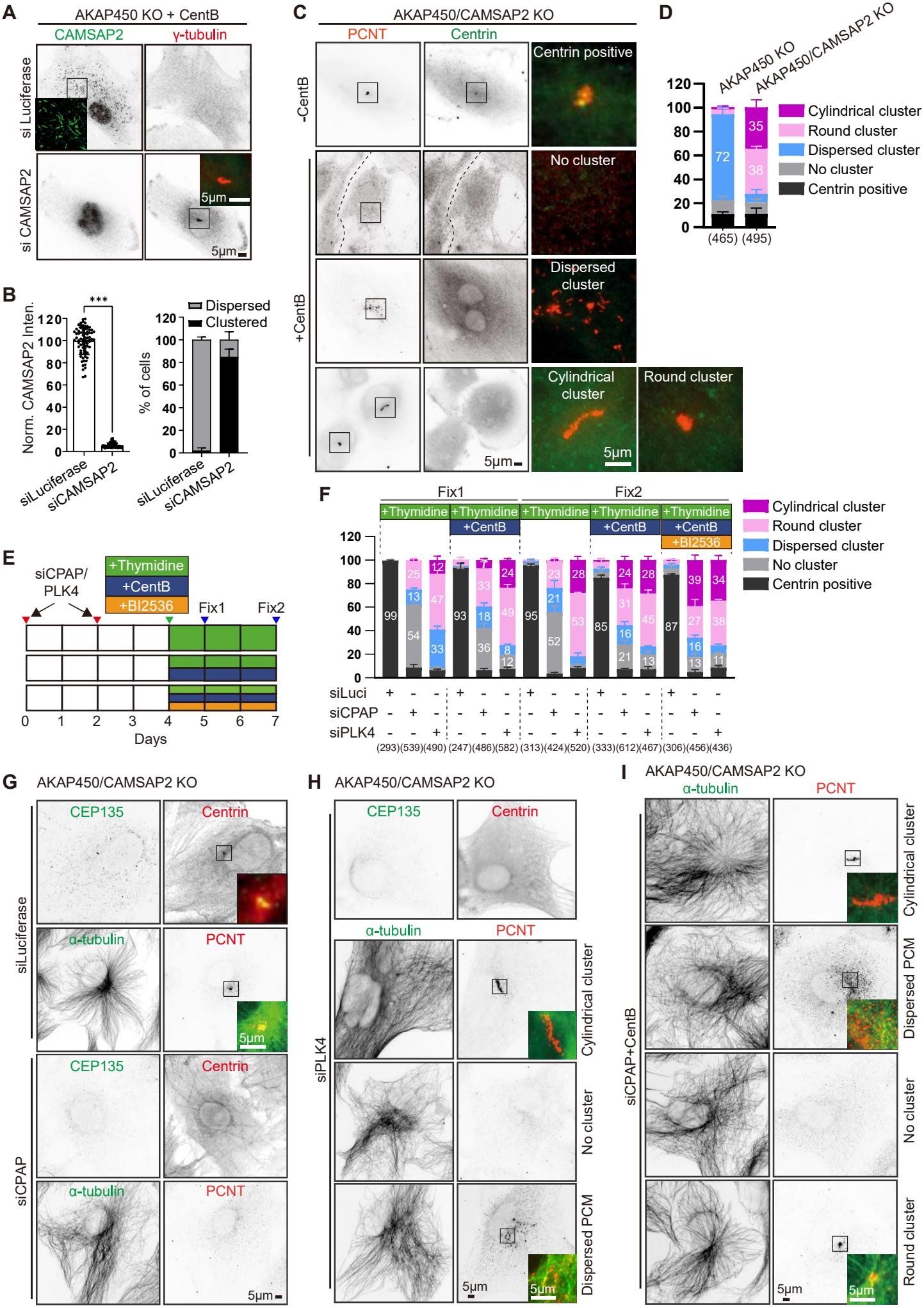

Figure 1 - figure supplement 2

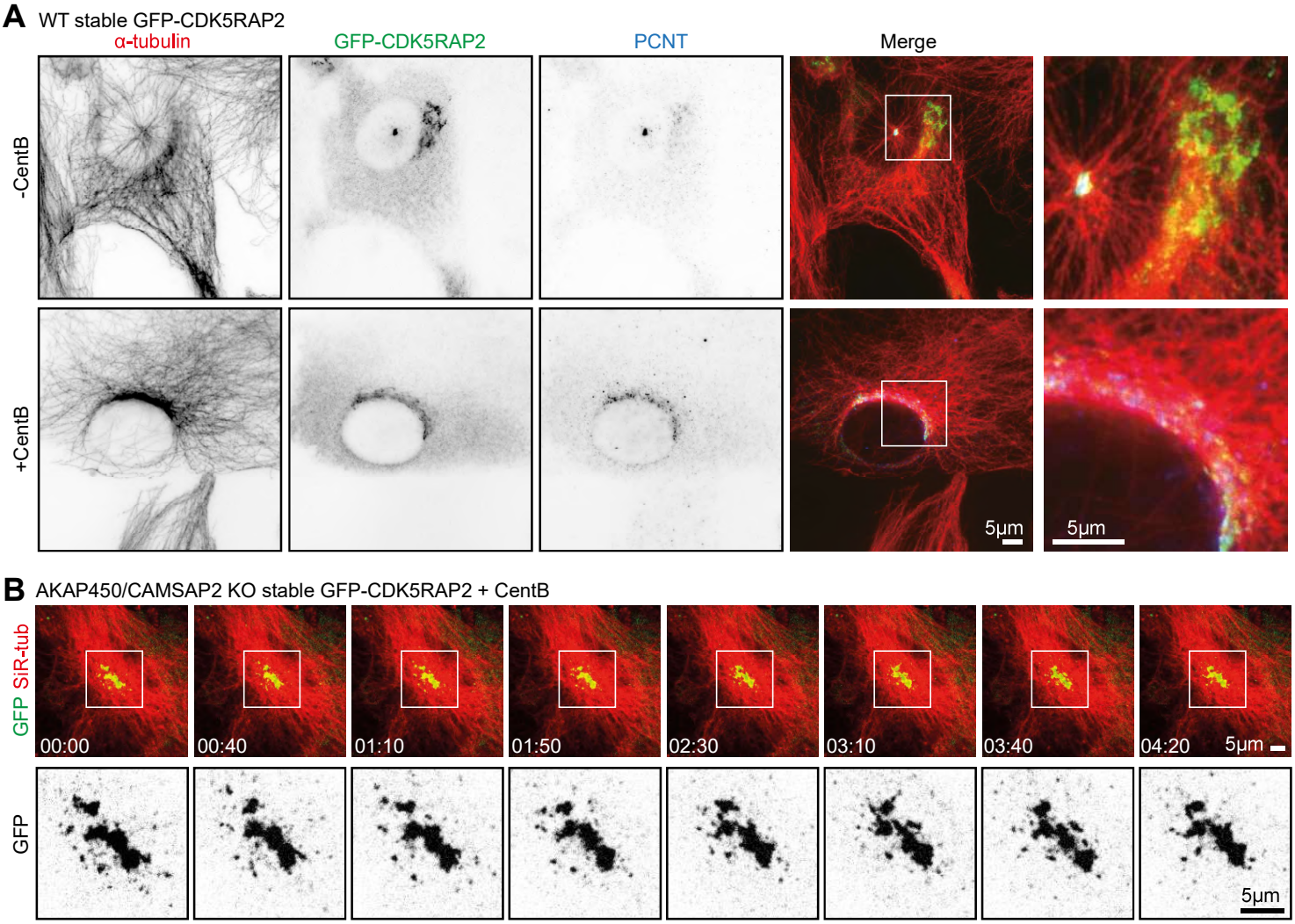

Figure 2- figure supplement 1

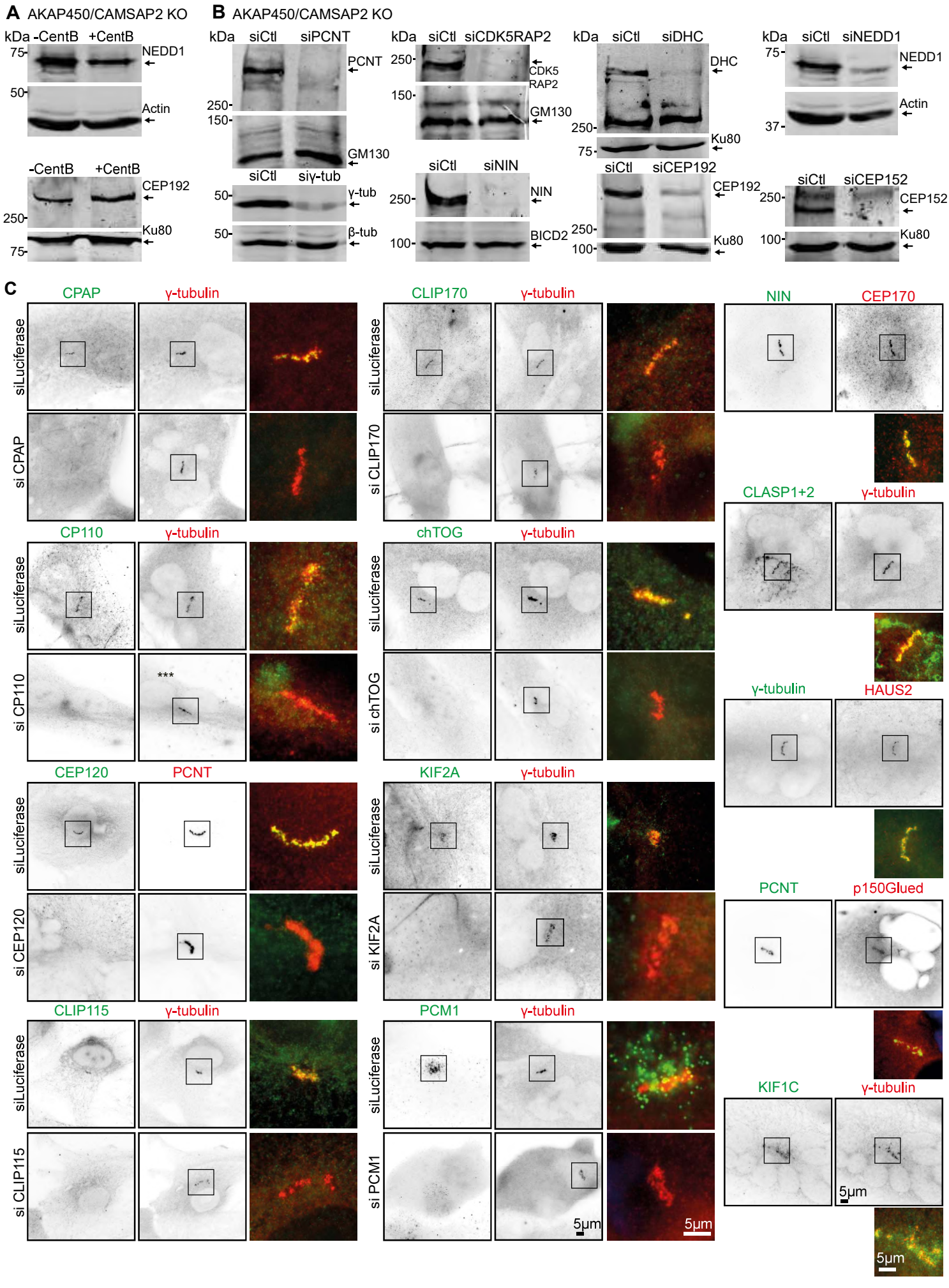

Figure 2 - figure supplement 2

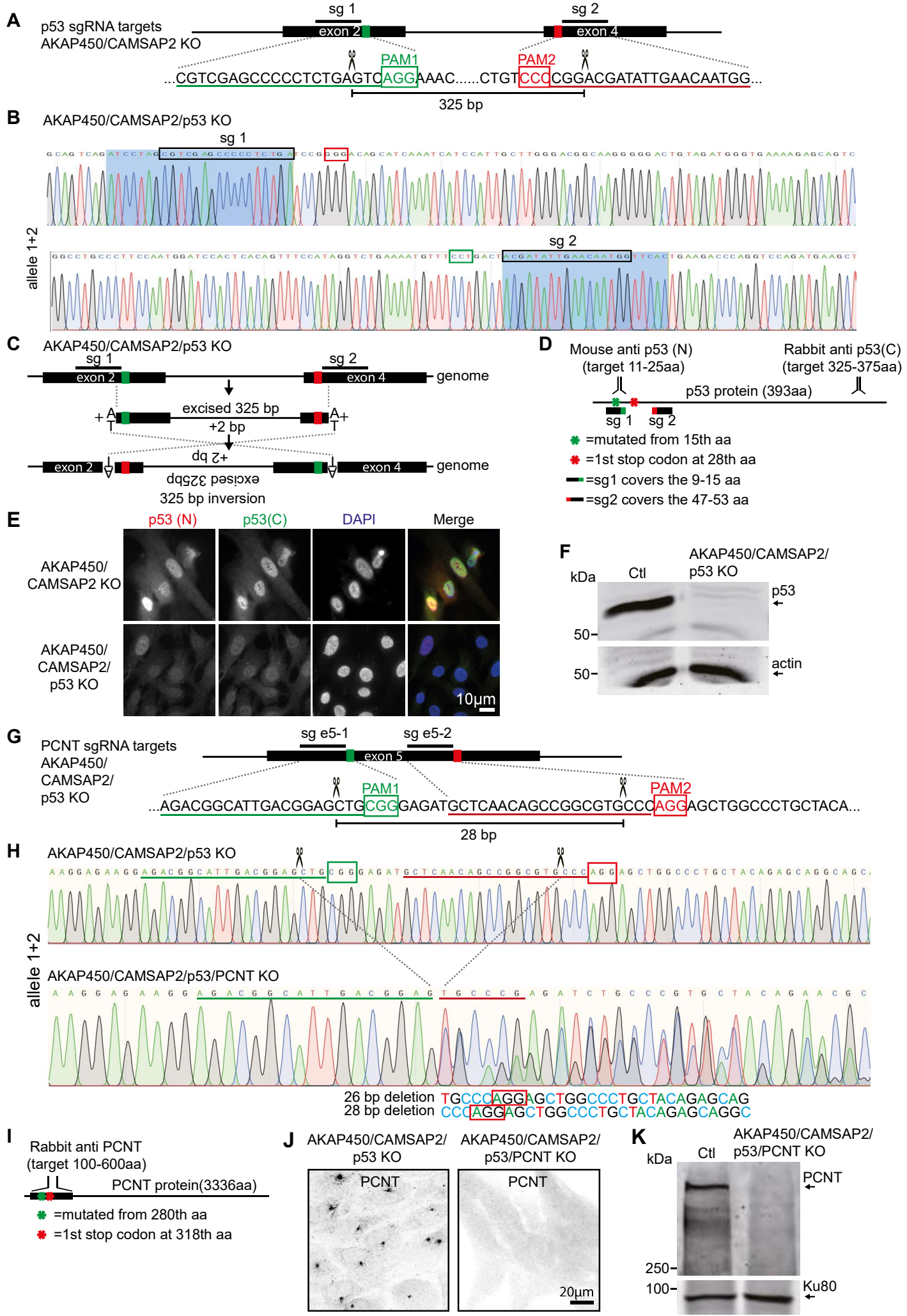

Figure 2 - figure supplement 3

Ctl=AKAP450/CAMSAP2/p53 KO + CentB

PCNT KO=AKAP450/CAMSAP2/p53/PCNT KO + CentB

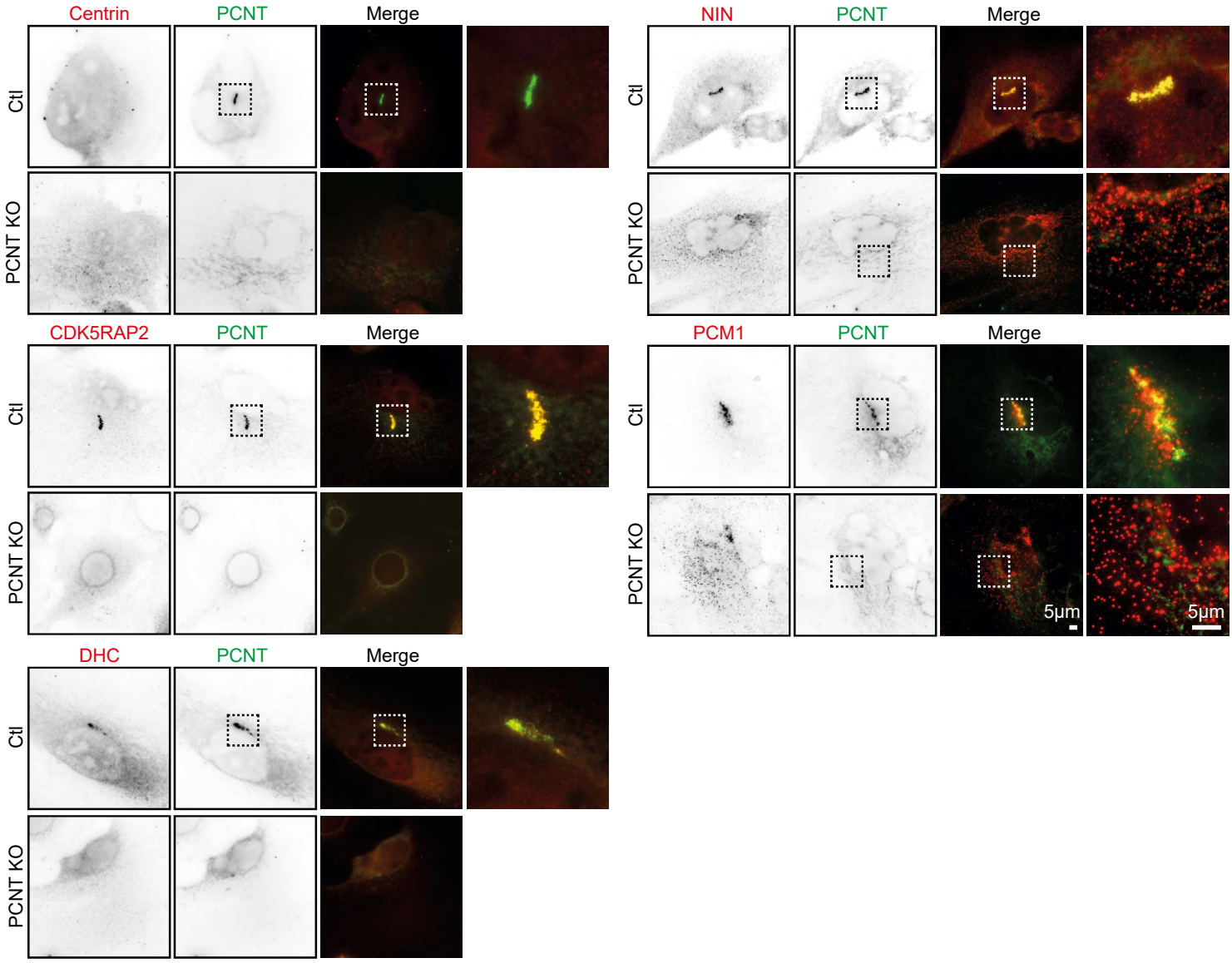

Figure 2 - figure supplement 4

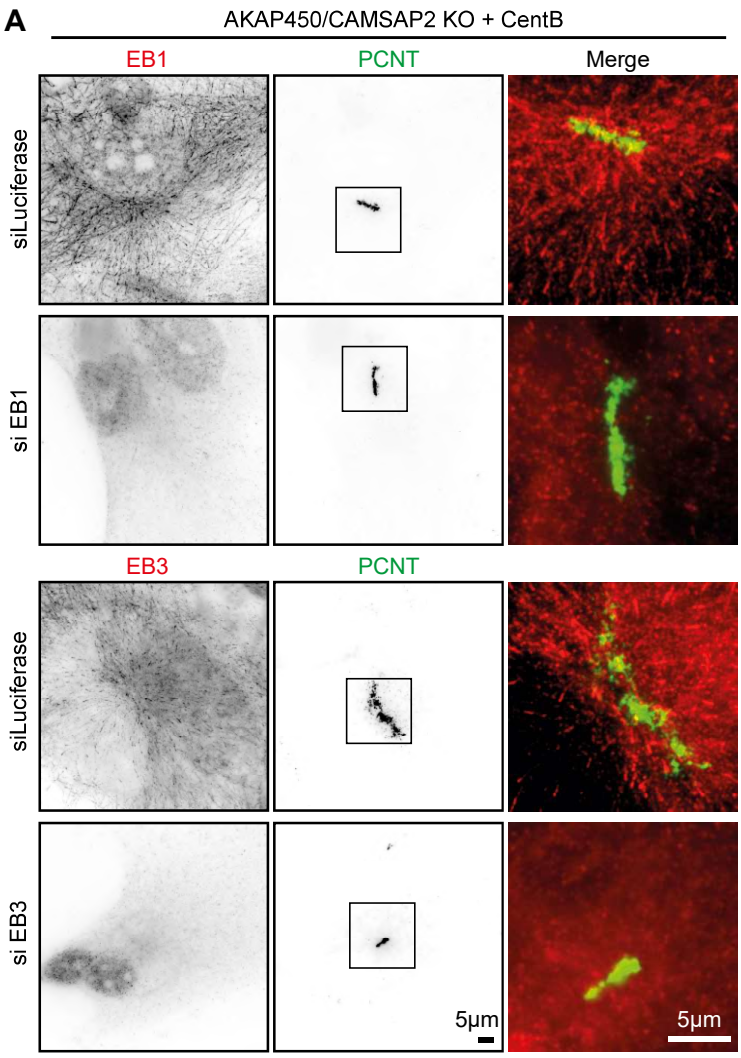

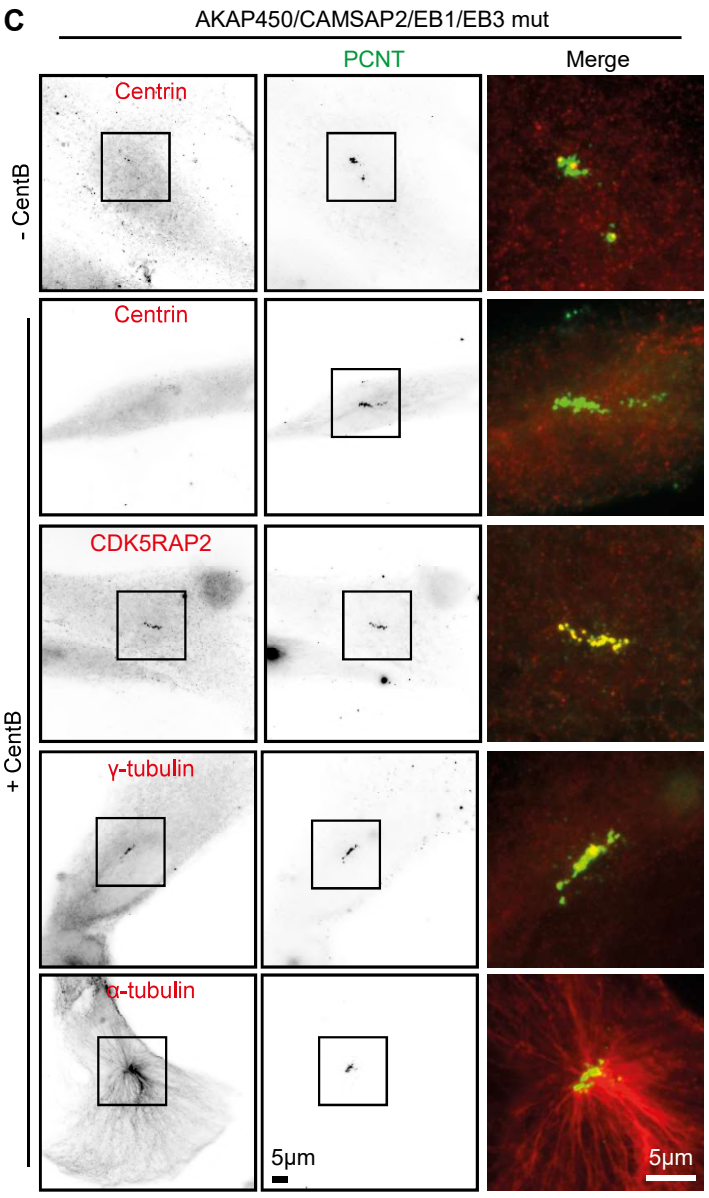

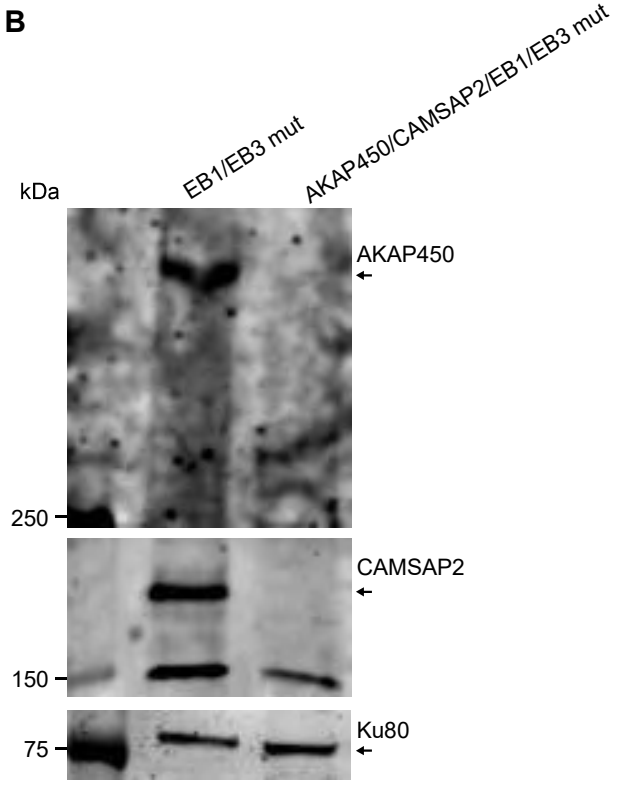

Figure 4 - figure supplement 1

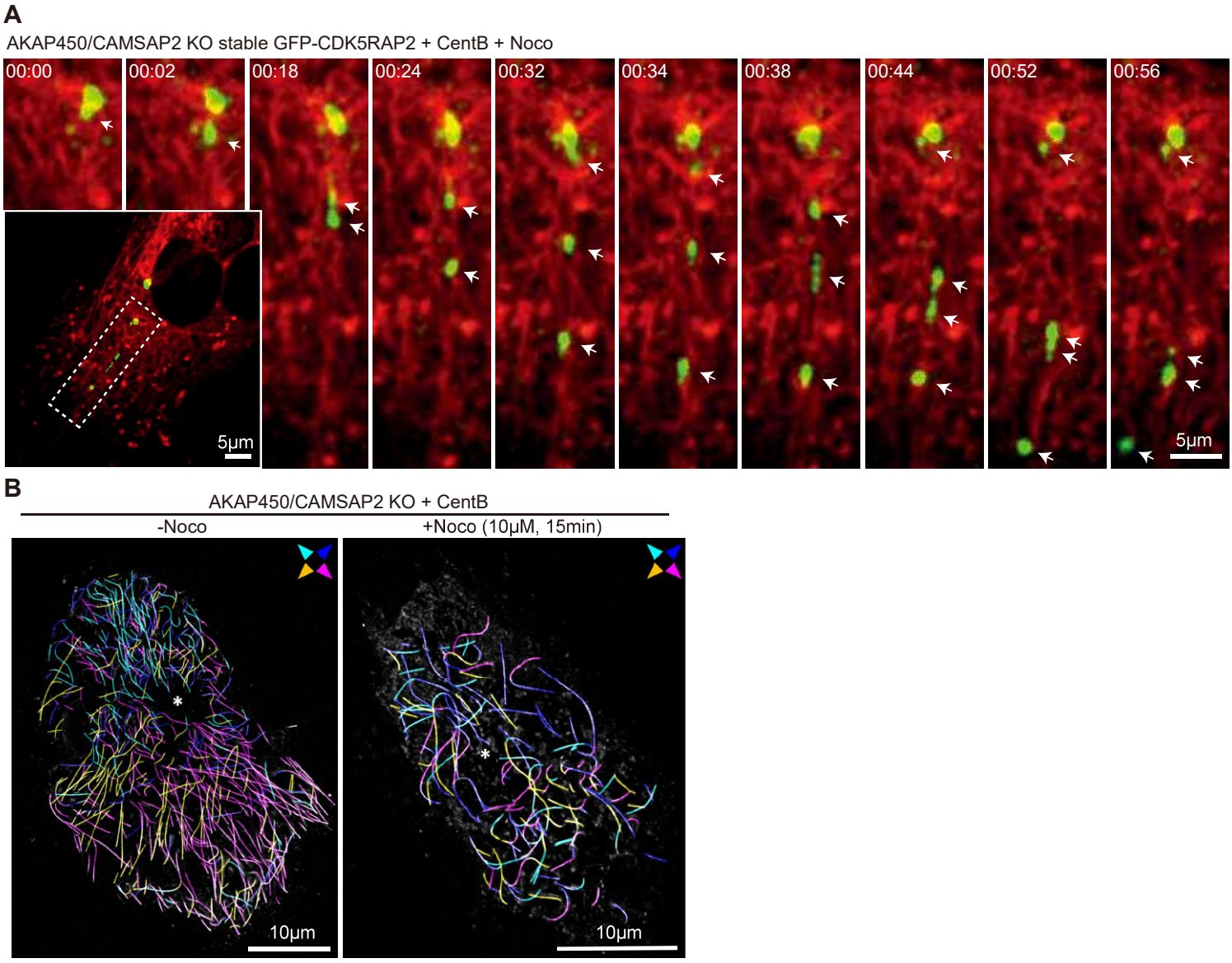

Figure 5 - figure supplement 1

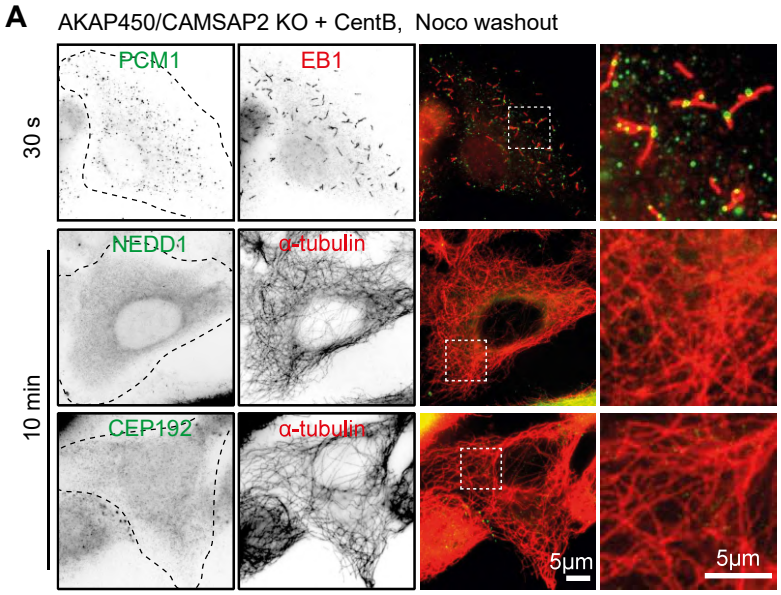

B

Presence of PCM proteins in clusters before/after Noco washout

CentB	-	+	+	+	+	+
Nocodazole	-	-	+	+	+	+
Washout			30 s	2 min	5 min	10 min
PCNT	+	+	+	+	+	+
CDK5RAP2	+	+	+	+	+	+
γ-tubulin	+	+	+	+	+	+
NEDD1	+	-	-	-	-	-
Ninein	+	+	-	+	+	+
CEP192	+	-	-	-	-	-
PCM1	+	+	+	+	+	+

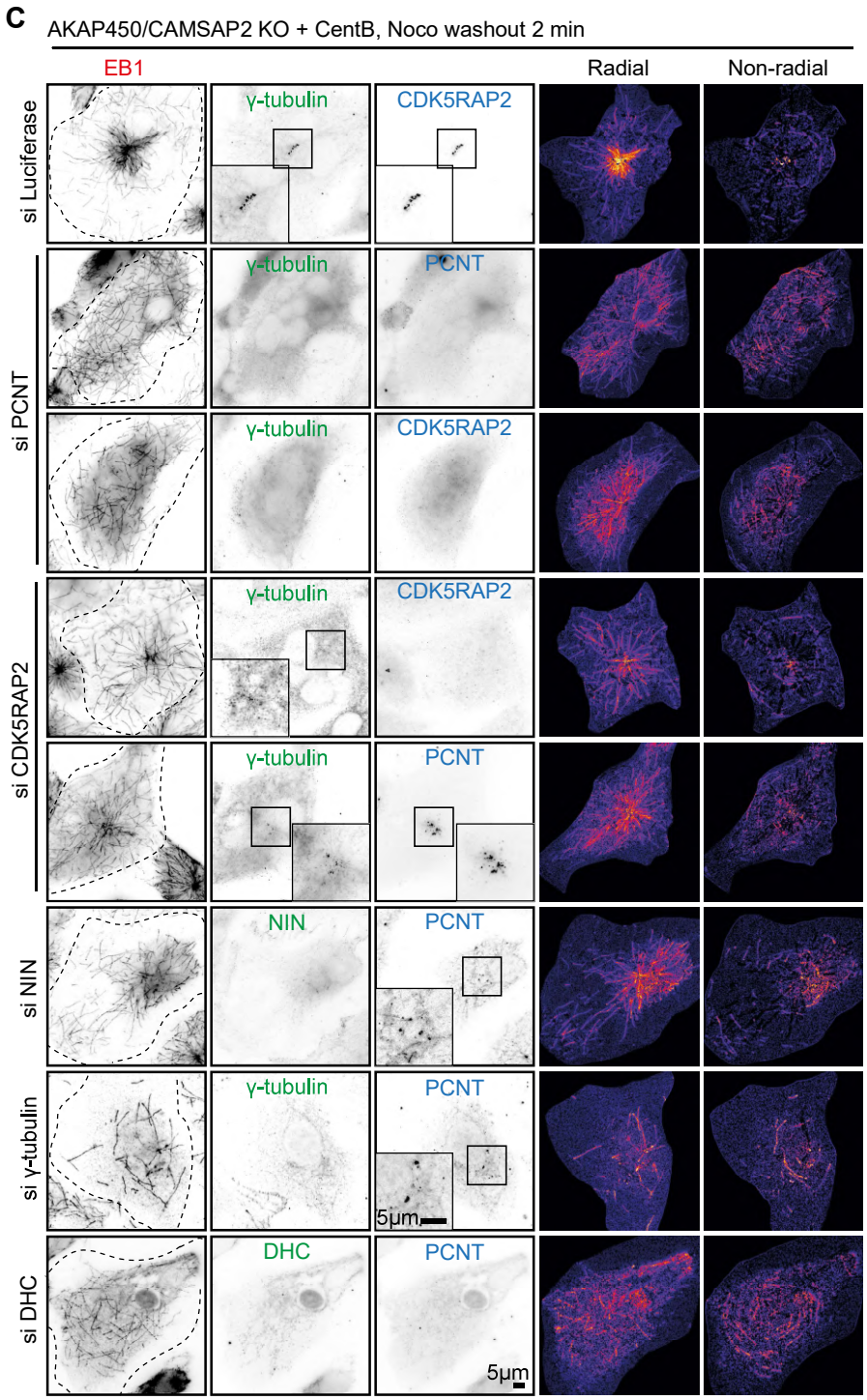

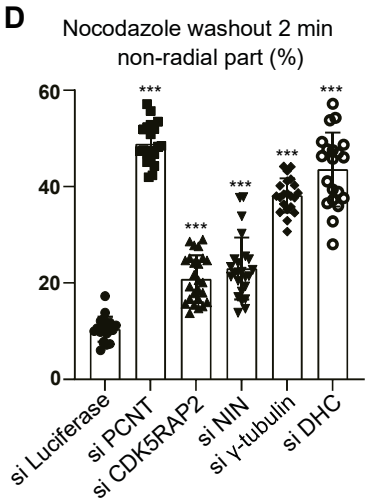

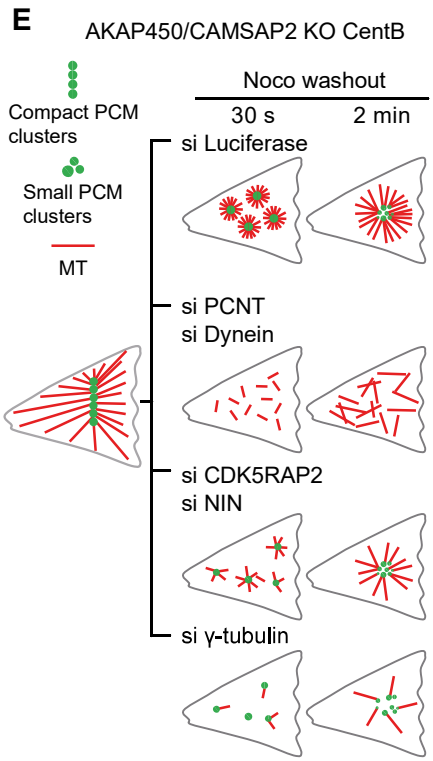

Figure 5 - figure supplement 2

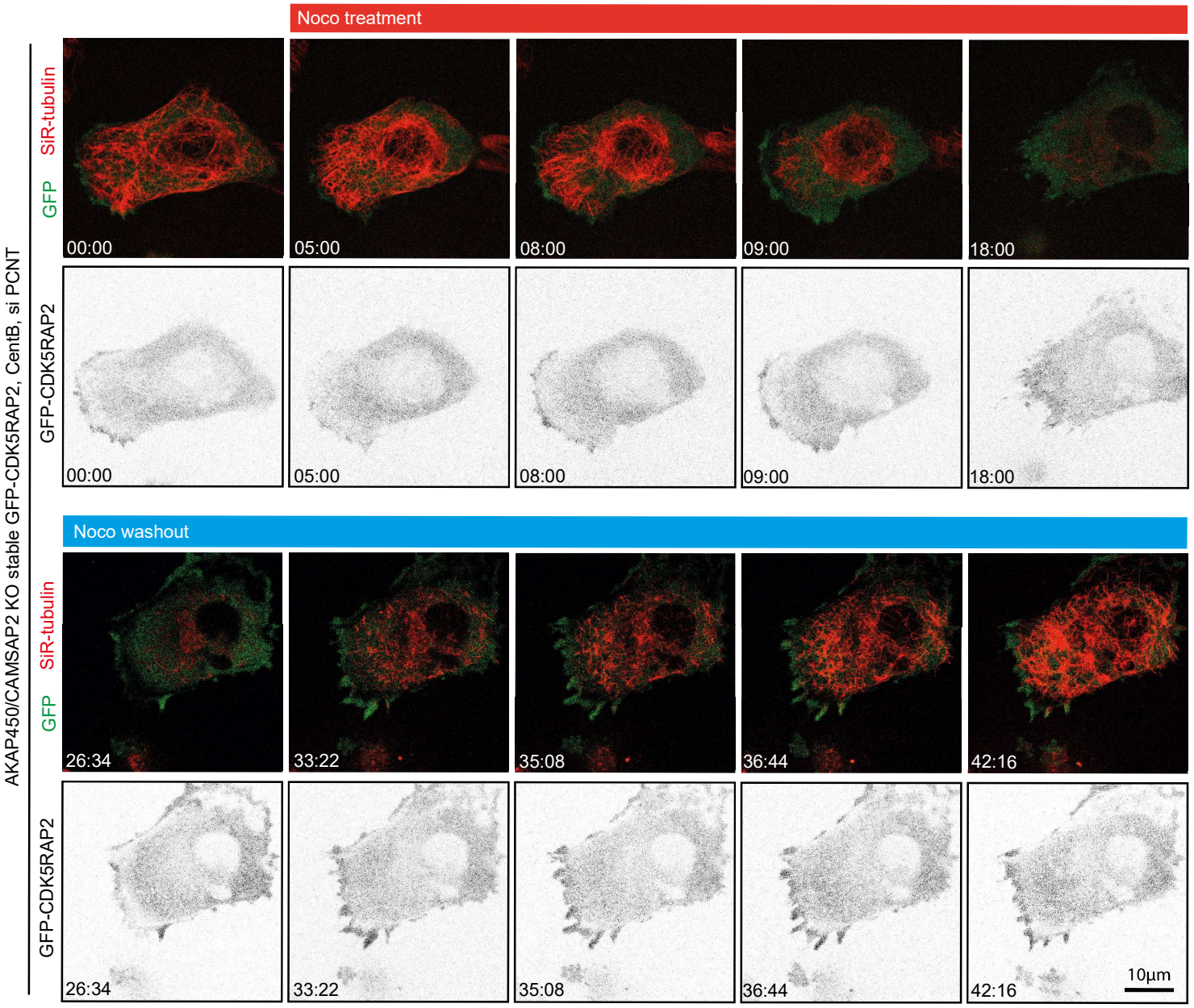

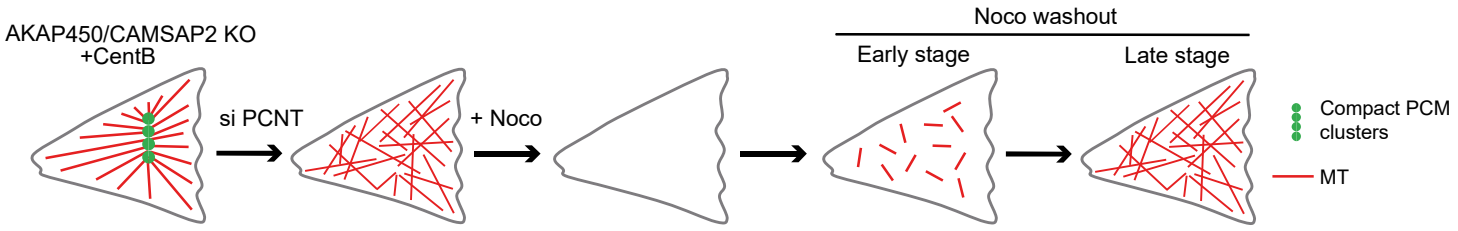

Figure 6 - figure supplement 1

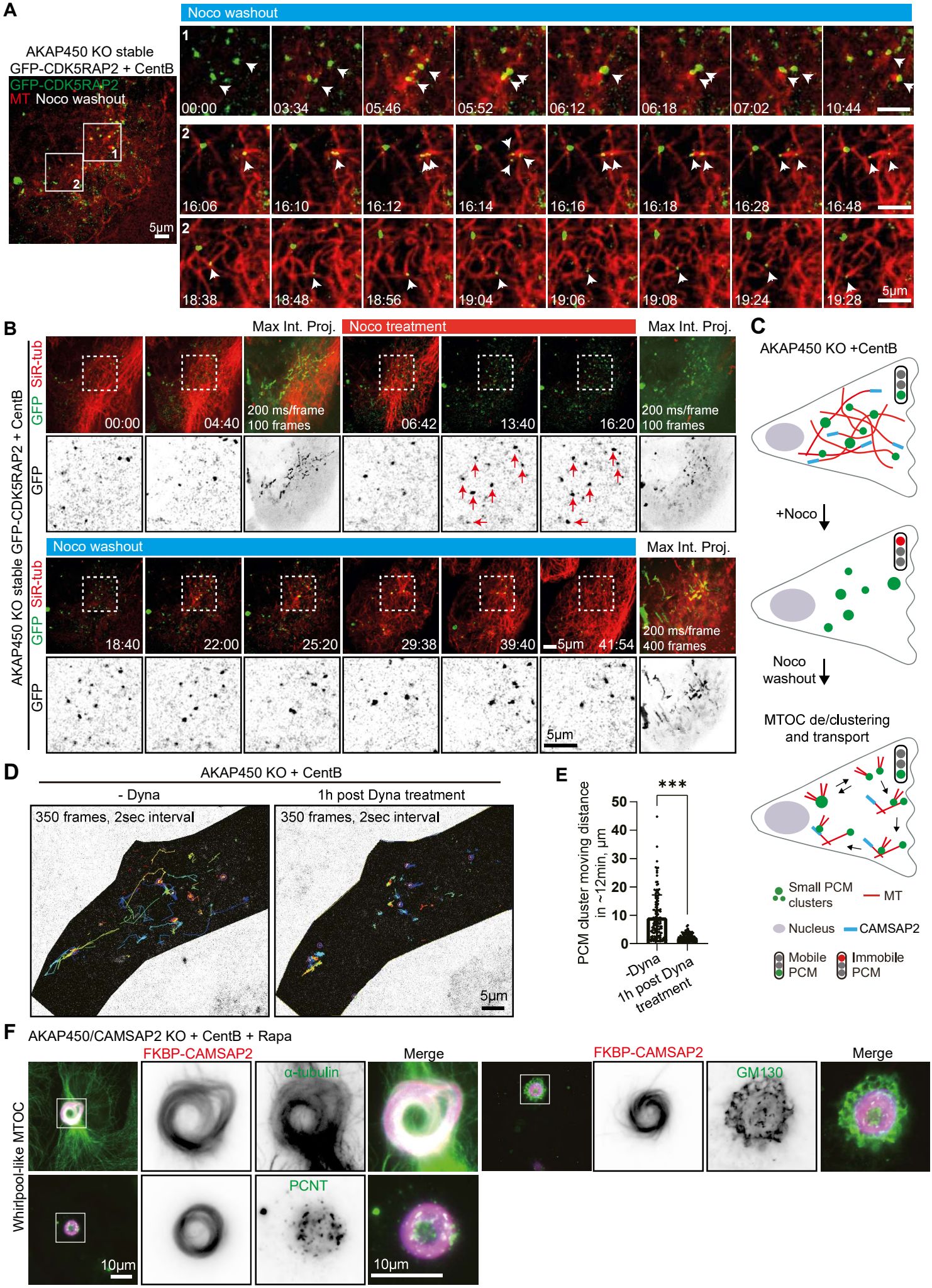

Figure 6 - figure supplement 2

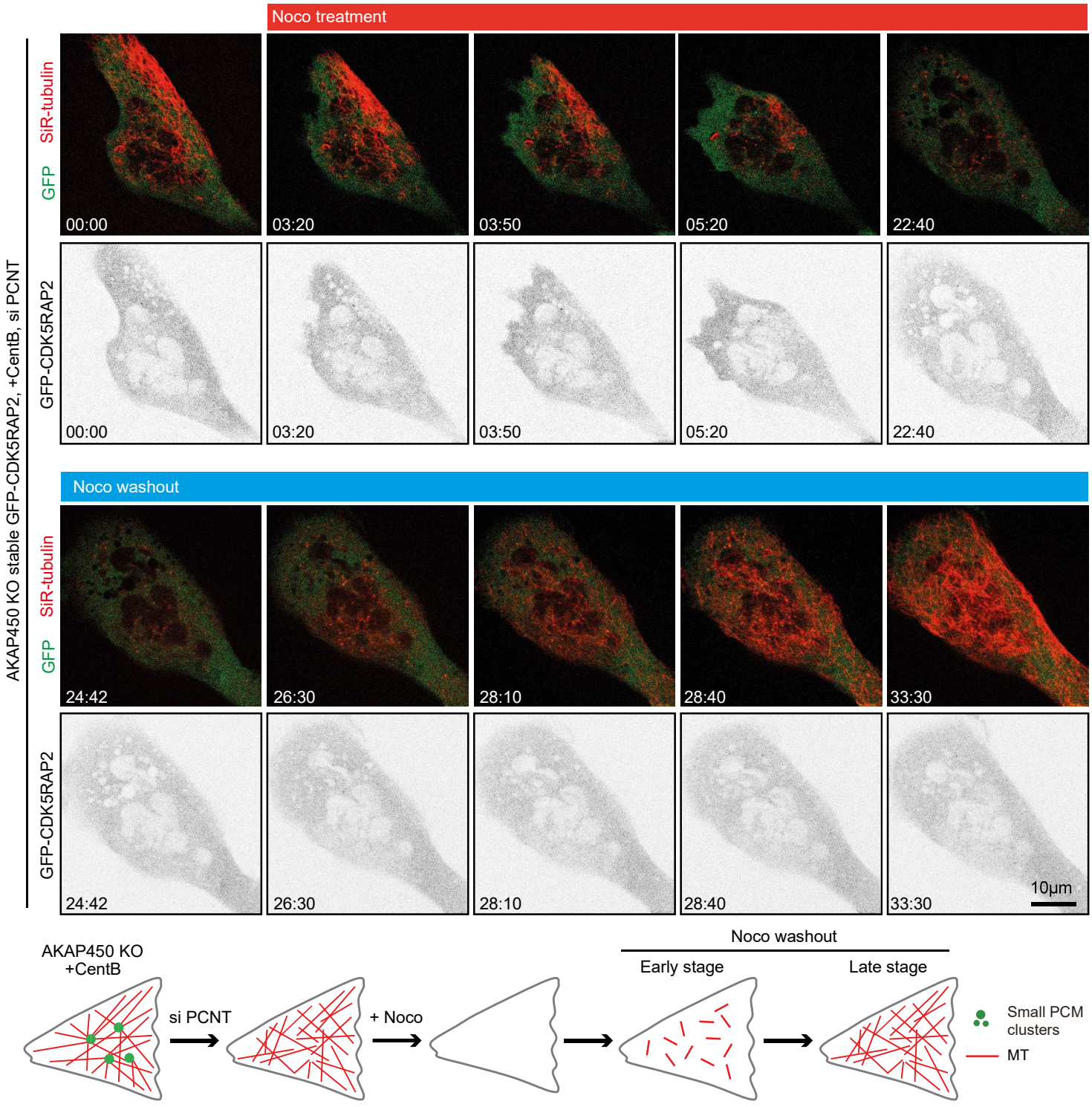

Figure 7 - figure supplement 1

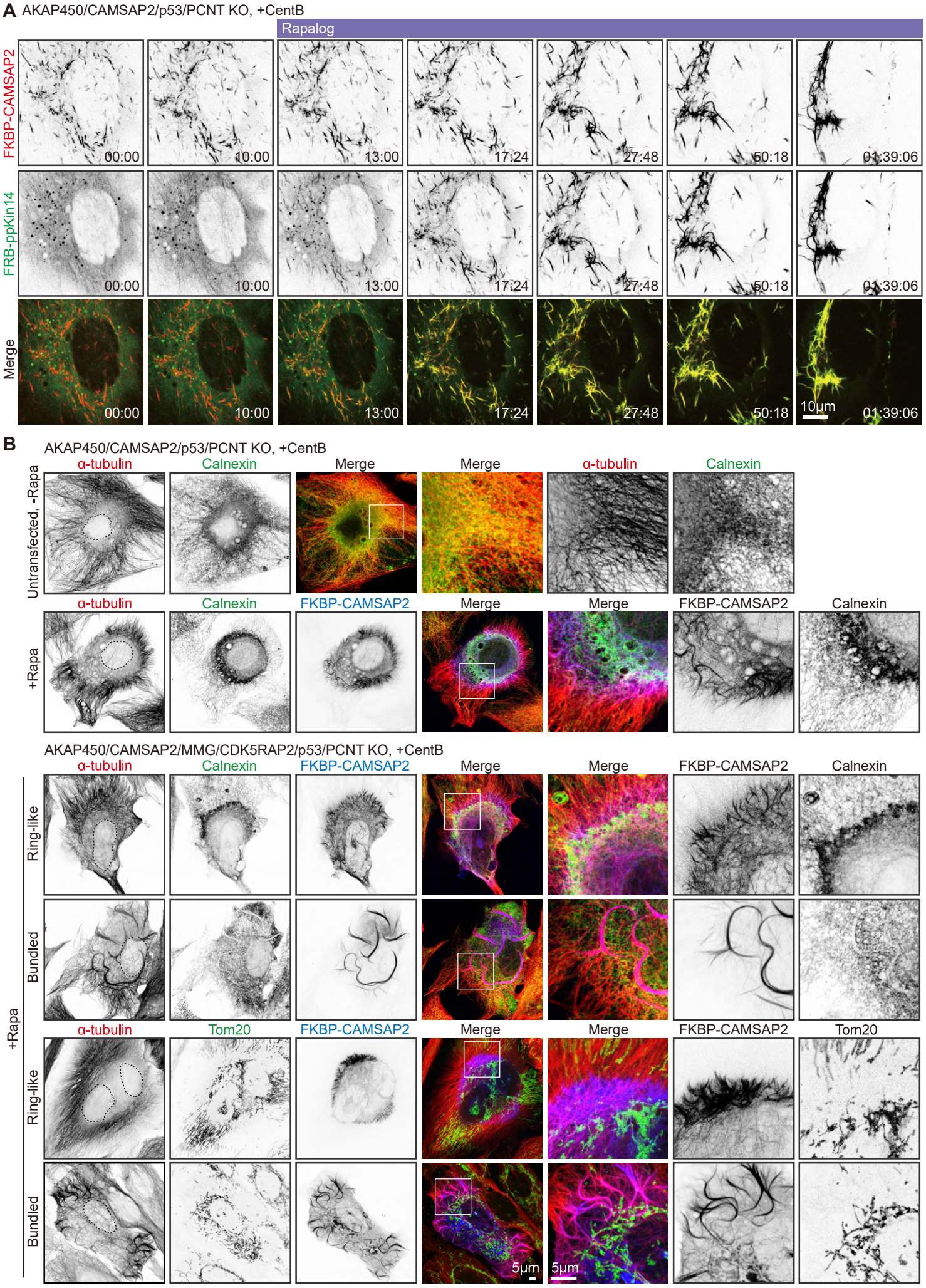

Figure 7- figure supplement 2

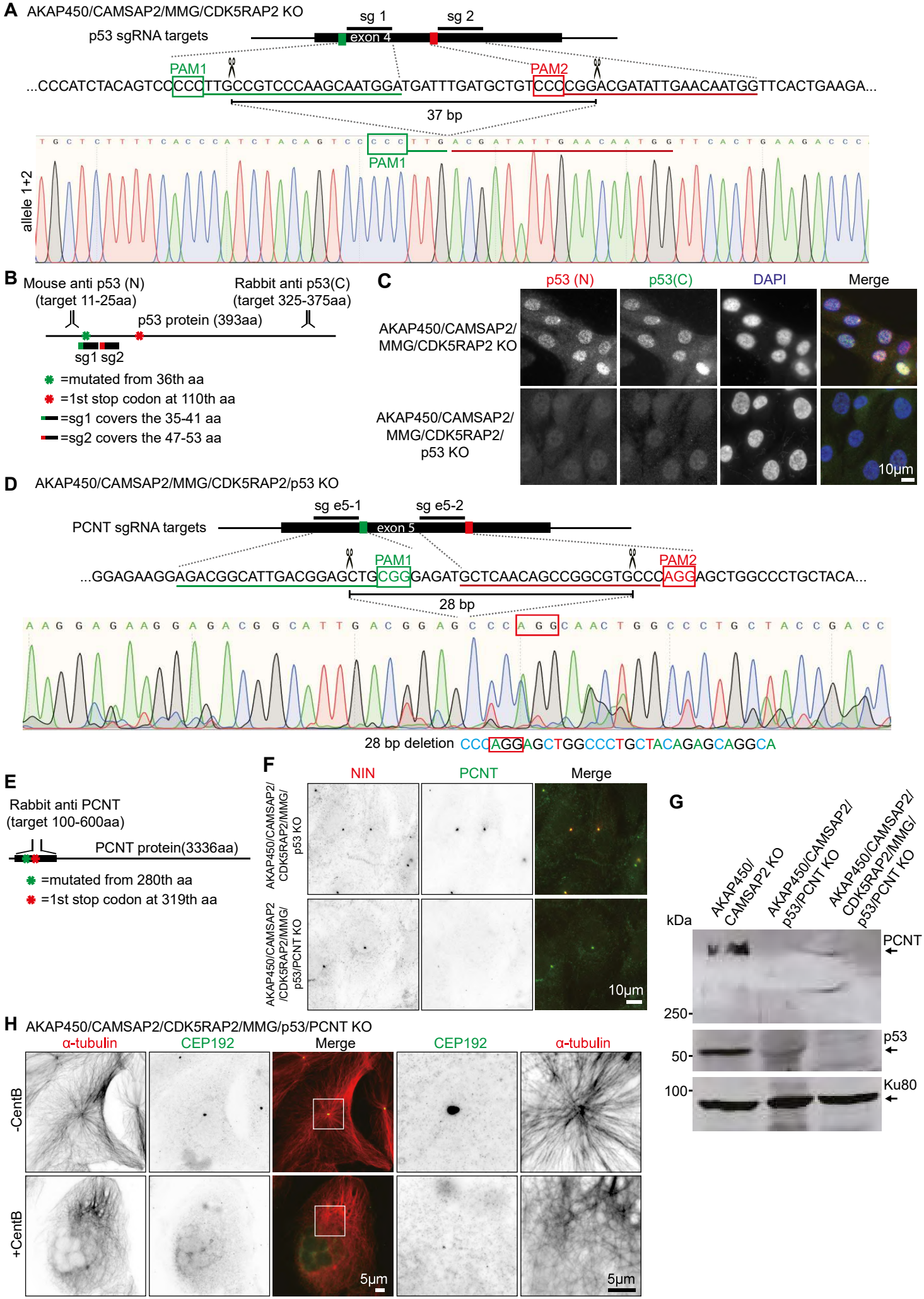

Source data 1
Uncropped Western blots shown in this manuscript

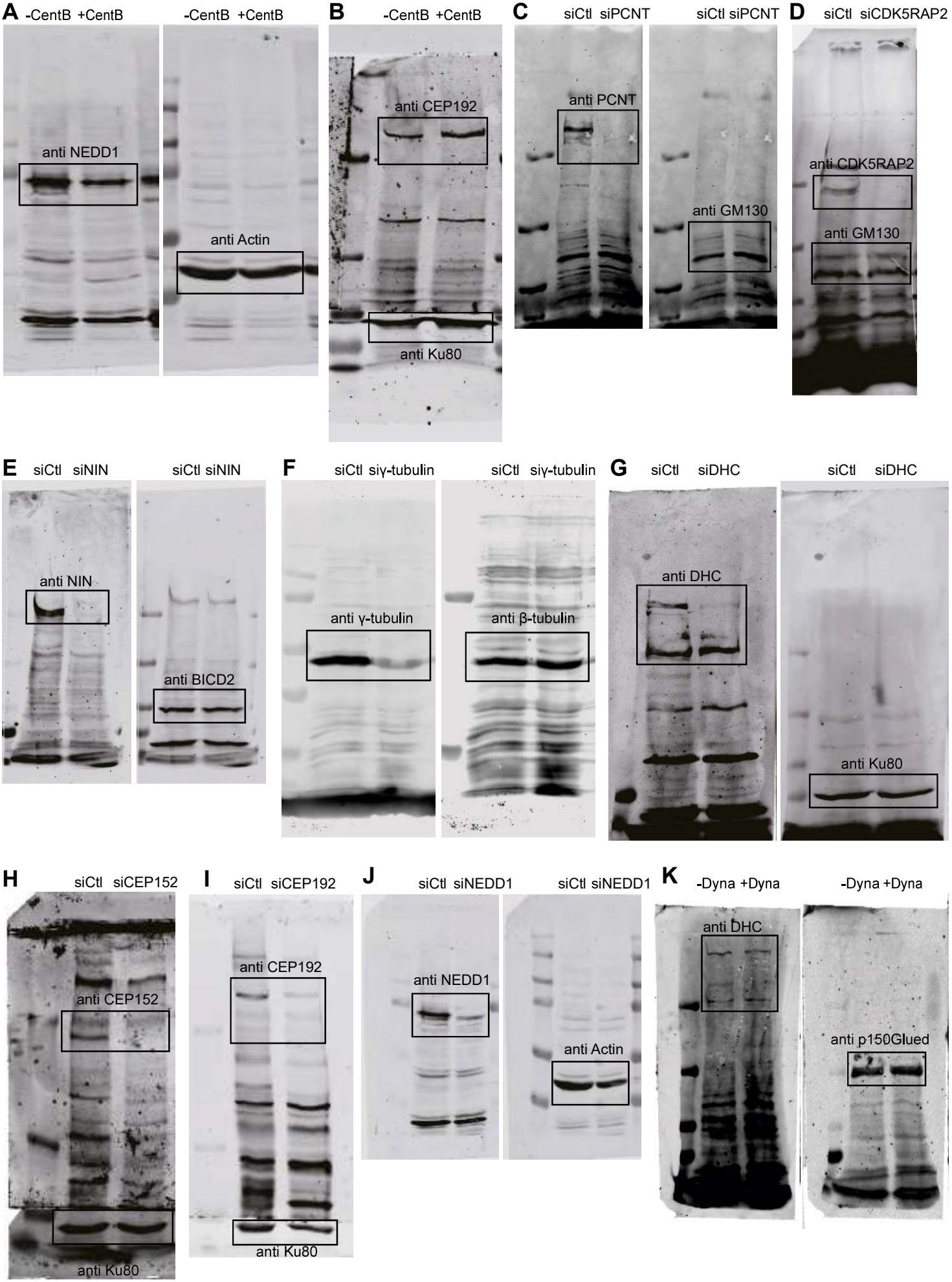

Source data 2
Uncropped Western blots shown in this manuscript